



# Snaking states and flux-periodic oscillations in cylindrical core-shell nanowires

Tómas Örn Rosdahl



Faculty of Physical Sciences  
University of Iceland  
2014



# SNAKING STATES AND FLUX-PERIODIC OSCILLATIONS IN CYLINDRICAL CORE-SHELL NANOWIRES

Tómas Örn Rosdahl

60 ECTS thesis submitted in partial fulfillment of a  
*Magister Scientiarum* degree in Physics

Advisor

Viðar Guðmundsson

M.Sc. committee

Andrei Manolescu

Viðar Guðmundsson

Faculty of Physical Sciences

School of Engineering and Natural Sciences

University of Iceland

Reykjavik, May 2014

Snaking states and flux-periodic oscillations in cylindrical core-shell nanowires  
Snaking states and FP oscillations in CS nanowires  
60 ECTS thesis submitted in partial fulfillment of a M.Sc. degree in Physics

Copyright © 2014 Tómas Örn Rosdahl  
All rights reserved

Faculty of Physical Sciences  
School of Engineering and Natural Sciences  
University of Iceland  
Hjarðarhagi 2-6  
107, Reykjavík  
Iceland

Telephone: 525 4700

Bibliographic information:

Tómas Örn Rosdahl, 2014, Snaking states and flux-periodic oscillations in cylindrical core-shell nanowires, M.Sc. thesis, Faculty of Physical Sciences, University of Iceland.

Printing: Háskólaprent, Fálkagata 2, 107 Reykjavík  
Reykjavík, Iceland, May 2014



# Abstract

We study the quantum mechanical states of electrons situated on a cylindrical surface of finite axial length to model a semiconductor core-shell nanowire. In a transverse magnetic field, the orbital characteristics of the electrons are determined by the radial component, which is nonuniform around the circumference. This leads to the formation of cyclotron states where the radial projection is maximum and snaking orbits where it vanishes. In a longitudinal magnetic field, emphasis is on manifestations of flux-periodic (FP) oscillations, and we calculate the conductance of the cylinder by weakly coupling it to semi-infinite leads. Oscillations survive and remain periodic in the presence of impurities, noncircular contacts and Rashba spin-orbit interaction (SOI). Furthermore, a transverse electric field flattens the oscillations but leaves them periodic, while Zeeman splitting results in aperiodicity, beating patterns and additional background fluctuations. Our results are in qualitative agreement with recent magnetotransport experiments performed on GaAs/InAs core-shell nanowires. Lastly, we propose methods of data analysis for detecting the presence of Rashba SOI in core-shell systems and for estimating the electron  $g$ -factor in the shell.

# Útdráttur

Skammtafræðileg rafeindaástand á endanlega löngu sívalningsyfirborði eru rannsökuð til að líkja eftir kjarna-skeljar hálfleiðarananóvír. Í þverstæðu segulsviði ákvarðast brautarhreyfing rafeindanna af ofanvarpi sviðsins í stefnu geislahnits. Þetta leiðir til myndunar hringhraðalsástanda þar sem geislahnitsofanvarp sviðsins er stærst og snákabrauta þar sem það er hverfandi. Þegar segulsviðinu er beint eftir ás sívalningsins greinast sveiflur sem eru lotubundnar í segulflæðinu og við reiknum leiðni sívalningsins með því að tengja hann veiklega við hálfóendanlegar leiðslur. Lotubundnar sveiflur eru greinanlegar þrátt fyrir að reiknað sé með íbótaratómum, Rashba spuna-brautar víxlverkun og að hringsamhverfa tenginganna við leiðslurnar sé brotin. Í þverstæðu rafsviði fletjast sveiflurnar út en eru þó enn lotubundnar, en þegar tekið er tillit til Zeeman klofnunar eru sveiflurnar enn greinanlegar en ekki lengur lotubundnar og aðrar lágtíðnisveiflur sjást í bakgrunni. Reikningum okkar ber vel saman við niðurstöður tilrauna á GaAs/InAs kjarna-skeljar nanóvírum. Að lokum gerum við grein fyrir hvernig nota megni niðurstöður leiðnimælinga til að greina tilvist Rashba spuna-brautar víxlverkunar og til að meta segulspunahlutfallsstuðul rafeindanna í skelinni.



# Contents

<b>List of Figures</b>	<b>ix</b>
<b>Acknowledgments</b>	<b>xiii</b>
<b>1. Introduction</b>	<b>1</b>
<b>2. A quantum mechanical model for closed core-shell nanowires</b>	<b>5</b>
2.1. The envelope function . . . . .	5
2.2. The single-electron Hamiltonian . . . . .	7
2.3. Densities and the chemical potential . . . . .	13
2.4. Symmetries . . . . .	15
<b>3. Results for the closed system</b>	<b>21</b>
3.1. Transverse magnetic field . . . . .	22
3.2. Longitudinal magnetic field . . . . .	27
<b>4. Modelling transport through the finite system</b>	<b>35</b>
4.1. Green's functions . . . . .	36
4.2. Obtaining conductance with Green's functions . . . . .	38
4.3. Evaluating the conductance - Leads and coupling kernels . . . . .	45
<b>5. Results of transport calculations</b>	<b>49</b>
5.1. Flux-periodic conductance oscillations and spin effects . . . . .	49
5.2. Transverse electric field . . . . .	56
5.3. Broken circular symmetry of the contacts . . . . .	59
<b>6. Inclusion of core impurities</b>	<b>61</b>
6.1. Formalism . . . . .	61
6.2. Results with core impurities included . . . . .	63
<b>7. Conclusions and summary</b>	<b>69</b>
<b>A. Evaluation of self-energy matrix elements</b>	<b>71</b>
<b>B. Evaluation of impurity-potential matrix elements</b>	<b>75</b>
<b>Bibliography</b>	<b>77</b>



# List of Figures

- 2.1. Effective magnetic potential  $V_{Bx}(\phi)$  evaluated for different values of  $k(l_B^x)^2/r_0$ . At small  $k(l_B^x)^2/r_0$ , minima at  $\phi = 0$  and  $\phi = \pi$  may produce localized cyclotron states. As  $k(l_B^x)^2/r_0$  increases, extrema form at points where the projection  $B_x \cos(\phi)$  vanishes, producing stable equilibrium points at the potential minimum, e. g. at  $\phi = 3\pi/2$  for  $k > 0$ . . . . . 9
- 3.1. Electron (left) and current (right) densities of  $N_e = 10$  electrons in transverse magnetic fields of strength: (a), (b)  $B_x = 1$  T. (c), (d)  $B_x = 2$  T. (e), (f)  $B_x = 4$  T. As  $B_x$  increases, the densities increase around the angles  $\phi = \pi/2$  and  $\phi = 3\pi/2$  but decrease around  $\phi = 0$  and  $\phi = \pi$ . The electron density is given in units of  $10^{-4} \text{ nm}^{-2}$ . . . . 23
- 3.2. Charge and spin densities of  $N_e = 90$  electrons in a magnetic field  $B_x = 2$  T. Each curve corresponds to a combination of SOI parameters  $(\alpha_R, \beta_D)$  indicated in the key in units of meVnm. (a)-(d) Densities evaluated at  $z = 160 \text{ nm}$  as functions of  $\phi$ . (e),(f)  $\rho$  evaluated at  $\phi = 2\pi/5$  and  $\phi = 7\pi/5$ , respectively, plotted over a subinterval of the cylinder length, centered at  $z = L_0/2$ . (a)  $\rho$  is slightly asymmetric under reflections over  $\phi = 0$  and  $\phi = \pi$  when  $\beta_D \neq 0$ , but becomes symmetric if  $\beta_D = 0$ . The asymmetry becomes clear for the large value  $\beta_D = 30 \text{ meVnm}$ . (b),(c),(d) Analogous results for  $S_x$ ,  $S_y$  and  $S_z$ . Note that  $S_y$  and  $S_z$  may change sign under reflection over  $\phi = 0$  and  $\phi = \pi$ . In (e) and (f),  $\rho$  shows a longitudinal symmetry under reflections over  $z = L_0/2$  if  $\beta_D = 0$ . . . . . 25
- 3.3. Spin density  $S_x(\mathbf{r})$  of  $N_e = 90$  electrons plotted over a part of the cylinder surface centered at  $z = L_0/2$  in a transverse magnetic field  $B_x = 2 \text{ T}$  with (a)  $(\alpha_R, \beta_D) = (20, 0) \text{ meVnm}$  and (b)  $(\alpha_R, \beta_D) = (0, 30) \text{ meVnm}$ , demonstrating the symmetry properties given in Eq. (3.11). A nonzero  $\beta_D$  creates a torsion of the spin density with opposite twist angles above and below the cylinder center. Bright and dark colors correspond to regions of high and low density, respectively. 27

## LIST OF FIGURES

- 3.4. Flux-dependence of the spectrum of a cylinder with spin suppressed,  $r_0 = 16.8$  nm and aspect ratio: (a)  $\eta = 0.25$ . (b)  $\eta = 3$ . (c)  $\eta = 10$ . In all cases, the spectrum is periodic in  $\Phi$ . . . . . 28
- 3.5. Flux-dependence of the spectrum of a cylinder with  $r_0 = 16.8$  nm and aspect ratio  $\eta = 3$  with: (a)  $g_e = -14.9$ ,  $\alpha_R = 0$ . (b)  $g_e = 0$ ,  $\alpha_R = 20$  meVnm. (c)  $g_e = -14.9$ ,  $\alpha_R = 20$  meVnm. The Zeeman term breaks the flux-periodicity whereas the Rashba term does not. . . . . 30
- 3.6. Current and spin densities of  $N_e = 8$  electrons on a cylinder with  $r_0 = 16.8$  nm and  $L_0 = 50.4$  nm ( $\eta = 3$ ) in a magnetic field  $B_z = 2$  T ( $\Phi/\Phi_0 \approx 0.4$ ) with Rashba SOI and Zeeman interaction. Both  $\mathbf{j}(\mathbf{r})$  and  $S_z(\mathbf{r})$  are circularly symmetric since  $\mathbf{v}$  and  $\sigma_z$  are rotationally invariant. However,  $S_x(\mathbf{r})$  and  $S_y(\mathbf{r})$  lack this property because  $\sigma_x$  and  $\sigma_y$  do not commute with the rotation operator  $D_z$ . . . . . 32
- 5.1. Conductance of a cylinder with aspect ratio  $\eta = 3$  for varying values of the chemical potential and magnetic flux, with: (a)  $\alpha_R = g_e = 0$ . (b)  $\alpha_R = 0$ ,  $g_e = -14.9$ . (c)  $\alpha_R = 20$  meVnm,  $g_e = 0$ . (d)  $\alpha_R = 20$  meVnm,  $g_e = -14.9$ . Conductance peaks correspond to broadened chemical potential intersections with the closed-system spectrum, resulting in periodic conductance oscillations provided  $g_e = 0$  (compare with Fig. 5.2). The shape and phase of the oscillations are dependent on the value of  $\mu$  considered, due to the varied structure of the spectrum. . . . . 50
- 5.2. Spectrum of a cylinder with aspect ratio  $\eta = 3$  as a function of magnetic flux with: (a)  $\alpha_R = g_e = 0$ . (b)  $\alpha_R = 0$ ,  $g_e = -14.9$ . (c)  $\alpha_R = 20$  meVnm,  $g_e = 0$ . (d)  $\alpha_R = 20$  meVnm,  $g_e = -14.9$ . Provided  $g_e = 0$ , the spectrum is periodic in the longitudinal magnetic flux even in the presence of Rashba SOI. . . . . 51
- 5.3. Spectrum of a cylinder with  $r_0 = 55$  nm and  $L_0 = 100$  nm with: (a)  $g_e = -14.9$ ,  $\alpha_R = 0$ . (b)  $g_e = -29.8$ ,  $\alpha_R = 0$ . (c)  $g_e = -29.8$ ,  $\alpha_R = 20$  meVnm. Due to Zeeman splitting, axial-sublevel minima produce sloped linear “traces” of parabola minima marked with dots. The traces can cross, resulting in large-scale DOS oscillations at a fixed energy. Doubling  $g_e$  moves the crossings to smaller values of  $\Phi$ . With Rashba SOI included the crossings become avoided. The values of  $\mu$  used to calculate  $G(\Phi)$  in Fig. 5.5 are marked with dashed lines. . . . . 53

- 5.4. Density of states of a cylinder coupled to leads, using the parameters  $r_0 = 55$  nm,  $L_0 = 100$  nm,  $g_e = -14.9$  and  $\alpha_R = 0$  meVnm, evaluated at the energies 15 (left) and 21 (right) meV, marked with dashed lines in Fig. 5.3 (a). The sloped “traces” result in a slowly varying DOS with  $\Phi$ . . . . . 54
- 5.5. A cylinder with  $r_0 = 55$  nm and  $L_0 = 100$  nm. (a), (b) and (c):  $G(\Phi)$  evaluated at  $\mu = 15$  meV (solid) and  $\mu = 21$  meV (dashed) with (a)  $g_e = -14.9$ ,  $\alpha_R = 0$ , (b)  $g_e = -29.8$ ,  $\alpha_R = 0$  and (c)  $g_e = -29.8$ ,  $\alpha_R = 20$  meVnm. Due to Zeeman splitting, conductance oscillations are superimposed on background fluctuations, the form of which depends on  $\mu$  as is reflected in the spectrum [compare with Figs. 5.3 (a), (b) and (c)]. (d) Flux-averaged conductance  $\langle G(N) \rangle$  relative to  $\langle G(N = 1) \rangle$  at  $\mu = 21$  meV, plotted against flux number  $N$  with  $g_e = -29.8$  for different values of  $\alpha_R$ , given in units of meVnm in the key. As  $\alpha_R$  increases, the amplitude of the peak around  $\Phi/\Phi_0 = N = 15$  is reduced, reflected in the Rashba-induced avoided crossings of “traces” in Fig. 5.3 (c). . . . . 55
- 5.6. Energy spectrum as a function of magnetic flux with a transverse electric field  $E_x = 1$  meV/nm for a finite cylinder of: (a) aspect ratio  $\eta = 3$ , (b) aspect ratio  $\eta = 0.25$  (ring limit). The spectrum remains periodic in  $\Phi$ , although oscillations are reduced in amplitude for states with low angular momentum  $L_z$ . Note that the figures are not to scale. 57
- 5.7. Magnetoconductance of a finite cylinder with aspect ratio  $\eta = 3$  in transverse electric fields of varying strength. The chemical potential is fixed at  $\mu = 29$  meV. Conductance oscillations remain flux-periodic, but as  $E_x$  increases their amplitude decreases and they are gradually washed out, such that  $G$  at fixed  $\mu$  is effectively constant as a function of  $\Phi$  in large transverse fields. The curves are to scale, but have been shifted along the  $y$ -axis for clarity. . . . . 58
- 5.8. Magnetoconductance evaluated at  $\mu = 29$  meV of the cylinder with spin neglected and unrestricted coupling (solid lines), compared to the case with coupling restricted to (dashed lines): (a)  $(\varphi_{min}^L, \varphi_{max}^L) = (0, \pi)$  and  $(\varphi_{min}^R, \varphi_{max}^R) = (\pi, 2\pi)$ . (b)  $(\varphi_{min}^L, \varphi_{max}^L) = (\pi/2, 3\pi/2)$  and  $(\varphi_{min}^R, \varphi_{max}^R) = (\pi/2, 2\pi)$ . Restricting the coupling alters the shape of the conductance oscillations, but they remain flux-periodic. . . . . 60

## LIST OF FIGURES

- 6.1. Electron (top) and current (bottom) densities of  $N_e = 8$  electrons on a cylinder with aspect ratio  $\eta = 3$  pierced by a longitudinal flux  $\Phi/\Phi_0 \approx 0.4$  with two distinct impurity configurations, 1 (left) and 2 (right), marked with filled dots. Due to the impurities, the rotational and parity symmetries are broken [compare with Figs. 3.6 (a) and (d)]. Bright and dark regions correspond to regions of high and low charge density, respectively. . . . . 64
  
- 6.2. Spectra of the cylinders with the same impurity configurations as in Fig. 6.1: (a) Configuration 1. (b) Configuration 2. The impurities break the parity and rotational symmetries, resulting in avoided crossings, flattening and deformation of energy levels as functions of  $\Phi$ . 65
  
- 6.3. Magnetoconductance of a cylinder of aspect ratio  $\eta = 3$  with impurity configuration 1 [Figs. 6.1 (a) and (c)] and: (a)  $\alpha_R = g_e = 0$ . (b)  $\alpha_R = 0$ ,  $g_e = -14.9$ . (c)  $\alpha_R = 20$  meVnm,  $g_e = 0$ . (d)  $\alpha_R = 20$  meVnm,  $g_e = -14.9$ . The figures are qualitatively similar to the case without impurities given in Fig. 5.1, but with damped oscillations. Impurities alone are insufficient to break the periodicity of the oscillations. . . . 66
  
- 6.4. Magnetoconductance evaluated at  $\mu = 29$  meV of a cylinder coupled to leads averaged over  $N_c = 250$  (dashed) and  $N_c = 750$  (dotted) random impurity configurations containing (a)  $N = 4$  and (b)  $N = 8$  impurities each. The curves almost overlap and further averaging does not affect results significantly. The solid lines show  $G(\Phi)$  without impurities. Impurity averaging reduces conductance oscillations in amplitude, but even with a highly doped core ( $N = 8$ ) they are still clearly visible. . . . . 67



# Acknowledgments

The work presented in this thesis was carried out at the University of Iceland. I would like to thank my instructors, professors Andrei Manolescu and Viðar Guðmundsson, whose limitless patience and enthusiasm for physics have been a source of inspiration. Whenever problems arose and assumed the form of questions, their doors were always open. I would also like to thank my colleagues for our numerous, interesting discussions over lunch, especially my fellow group members. I thank my family for their endless love and support, especially my parents, my aunt Anita and her husband Lars, who made my stay in Lund so much more enjoyable, and my fantastic girlfriend. My friends also deserve an honourable mention, especially my flatmates at Sækambur. Lastly, I extend my gratitude to all the musicians I've listened to during my studies, from Aphex Twin to the Wu-Tang Clan.

This work was partially funded by the Research Fund of the University of Iceland, the Icelandic Research Fund, the Instruments Fund and the Erasmus Student Grant for exchange studies.



# 1. Introduction

Recent years have seen significant progress in the development and fabrication of semiconductor nanostructures, and nanowires of diameters of the order of 10 – 100 nm can now be grown [1–4]. A semiconductor core-shell nanowire is a heterostructure composed of a thin material layer (shell) wrapped around a core in a tubular geometry, such that the longitudinal degree of freedom is parallel to the junction between core and shell [2–4]. The manufacture of a variety of geometries has been reported, e. g. cross sections which are triangular [5] or hexagonal [6], reflecting the lattice structure of the materials. The core and shell semiconductors may be chosen such that the difference in their conduction band energies forms a potential barrier confining carriers to either the core [7, 8] or the shell [6, 9]. Recent examples include nanowires composed of an InAs shell grown on a GaAs core, resulting in the formation of a highly conductive electron gas wrapped around the core, where electron transport takes place [10, 11]. Such GaAs/InAs core-shell nanowires will be the focus of this work. They provide a fascinating means for studying a plethora of physical phenomena. Examples include flux-periodic oscillations in longitudinal magnetic fields [12] and spin, which may couple to orbital observables and thus affect transport nontrivially [13]. Other aspects include Landau levels and the existence of cyclotron and snaking states in transverse magnetic fields [14, 15].

Generally in semiconductors, the intrinsic carrier concentration is insufficient to yield the current densities necessary for practical applications. Larger carrier concentrations can be obtained by adding electrically active impurities to the sample, i. e. by doping it. Such impurities can be divided into two categories, namely donors and acceptors, which add electrons to the conduction band and holes to the valence band, respectively. Since conduction electrons are the focus of this work, we will focus on donor-like impurities. In principle, donors are introduced by replacing individual lattice units (atoms or molecules) with an atom of another material with one more valence electron. The extra electron is weakly bound to the donor and thus forms a bound state relative to the conduction band with a small ionization energy. Hence, the extra electron is easily excited into the conduction band, leaving behind an ionized donor, i. e. a positively-charged impurity [16, 17].

At low enough temperature for negligible phonon excitations, an important source of scattering in semiconductors is Coulomb scattering of electrons due to charged impurities [16]. In a core-shell geometry, one might increase the concentration of

## 1. Introduction

shell conduction electrons by introducing donors to the shell. However, this would also result in increased Coulomb scattering due to the presence of ionized donors in the shell, which spoil the propagation of conduction electrons. A clever method to separate conduction electrons from their ionized donors is modulation doping, in which the dopants are grown separately from the conducting part of the sample [17]. In a core-shell geometry, doping is grown in the core, such that donor electrons are excited into the core conduction band. Due to the difference in conduction band energy between core and shell, some donor electrons wander into the energetically-lower conduction band of the shell, increasing the concentration of shell conduction electrons [10, 11]. This leaves behind positively charged ionized impurities in the core, resulting in the formation of an electric field that tends to drive shell conduction electrons back to the core. However, they are prevented from migrating back to the core due to the difference in conduction band energy. As a result, electrons accumulate in the shell, separated from their donors, resulting in reduced impurity scattering.

In this thesis, we analyze the energy spectrum, charge, current and spin densities of electrons confined to a closed cylindrical surface of finite length in an external magnetic field and furthermore discuss the transformation properties of the system under space inversion (parity) and rotation. The magnetic field can be oriented transverse to the cylinder surface or along the cylinder axis, such that the cylinder is pierced by a longitudinal magnetic flux. Electron spin is included through Zeeman splitting and SOI. In a transverse magnetic field, we identify snaking and cyclotron states where the radial projection of the field vanishes and is maximum, respectively. The latter are actually Landau levels, whose energies decrease as the magnetic field strength increases, resulting in a depletion of electrons from the cyclotron regions at large magnetic fields. Additionally, we find that Dresselhaus SOI breaks the parity symmetry of the closed system, which we relate to the edge currents that link the snaking states propagating between the cylinder edges. When the cylinder is pierced by a longitudinal magnetic flux, the spectrum is flux-periodic and we calculate the magnetoconductance of the finite system by coupling it to leads. Emphasis is on flux-periodic oscillations in both conductance and spectrum and how various factors affect them. The experimentally-relevant case of nonuniform coupling to leads leaves the conductance oscillations flux-periodic, and a transverse electric field tends to flatten them out. While donor impurities dampen the conductance oscillations, they remain resolvable after extensive averaging over multiple random impurity configurations, assuming realistic donor densities. Using parameters comparable to those reported in Ref. [11], we attribute background conductance oscillations, which are superimposed on the flux-periodic oscillations, to an interplay between the finite system length and Zeeman splitting, propose means for detecting the presence of Rashba SOI and discuss a method for estimating the shell electron  $g$ -factor based on transport data.

In Chapter 2 we describe the closed-system model, including the single-electron

Hamiltonian in Sec. 2.2 and useful symmetries in Sec. 2.4, and discuss results for the closed system in Chapter 3. In Chapter 4 we discuss the transport formalism and give results of transport calculations in longitudinal magnetic fields in Chapter 5. The effects of donor-like impurities in the core are discussed in Chapter 6 and lastly, we offer concluding remarks in Chapter 7.



## 2. A quantum mechanical model for closed core-shell nanowires

Due to the small length scales involved, the physics of nanoscale devices is the domain of quantum mechanics. In this section, we introduce a quantum mechanical model for conduction electrons in a closed core-shell nanowire. We start by bridging the gap between conventional single-particle quantum mechanics and the familiar solid-state physical description of particles propagating in crystals. Then, we move on to formulating the single-electron Hamiltonian.

### 2.1. The envelope function

Semiconductors are composed of atoms or molecules that are chemically bound together to form a lattice. Ideally, the lattice is composed of a periodic arrangement of identical building blocks called unit cells. This follows from translational symmetry, as every lattice point should be in an identical environment in a perfect crystal. In real semiconductor samples this periodicity is usually broken, for example by lattice defects and impurities. Lattice periodicity is usually assumed however, as it simplifies modelling of semiconductors significantly, such that lattice effects on electrons propagating in the sample are described by a lattice-periodic crystal potential  $V(\mathbf{r})$ . Thus, the time-independent Schrödinger equation for the eigenstates  $\psi(\mathbf{r})$  and -energies  $E$  of an electron propagating in the crystal is given by

$$\left( \frac{\mathbf{p}_k^2}{2m_0} + V(\mathbf{r}) \right) \psi(\mathbf{r}) = E\psi(\mathbf{r}), \quad (2.1)$$

where  $m_0$  is the free electron mass and  $\mathbf{p}_k$  the kinetic momentum operator. By Bloch's theorem, wave functions in a periodic system are Bloch states,  $\psi_{n\mathbf{k}}(\mathbf{r}) = U_{n\mathbf{k}}(\mathbf{r}) \exp(i\mathbf{k} \cdot \mathbf{r})$ , where  $U_{n\mathbf{k}}(\mathbf{r})$  is lattice-periodic. Here,  $n$  is the band index,  $\mathbf{k}$  the crystal momentum and  $E_n(\mathbf{k})$  gives the band structure.

Generally, one is interested in including extra inhomogeneities, such as external magnetic fields  $\mathbf{B}$ . To include a static magnetic field in the Hamiltonian, one introduces a vector potential satisfying  $\mathbf{B} = \nabla \times \mathbf{A}$  into the kinetic momentum  $\mathbf{p}_k = \mathbf{p} + e\mathbf{A}$ ,

## 2. A quantum mechanical model for closed core-shell nanowires

where  $\mathbf{p} = -i\hbar\nabla$  is the canonical momentum operator. Accounting for other static factors with the potential  $W(\mathbf{r})$ , e. g. impurities or an electric field, the single-electron Hamiltonian becomes

$$\left[ \frac{(\mathbf{p} + e\mathbf{A})^2}{2m_0} + V(\mathbf{r}) + W(\mathbf{r}) \right] \psi(\mathbf{r}) = E\psi(\mathbf{r}). \quad (2.2)$$

This equation is difficult to solve, largely due to the lattice-periodic potential  $V(\mathbf{r})$ . Furthermore, the problem of a two-dimensional lattice-periodic structure in a perpendicular magnetic field is conceptually challenging, because the spectrum manifests a fractal structure known as Hofstadter's butterfly when plotted against the magnetic flux through a lattice cell [18]. However, utilizing the effective mass approximation [16, 17], one can from Eq. (2.2) obtain an approximate equation which has the same form, but with  $V(\mathbf{r})$  omitted and the free electron mass  $m_0$  replaced by an effective electron mass. To derive it, one expands the eigenstates  $\psi(\mathbf{r})$  of the full Hamiltonian Eq. (2.2) in terms of Bloch states. They are eigenstates of the Hamiltonian Eq. (2.1), which satisfy the crystal boundary conditions, and hence form a basis for state space. One then assumes that only states from a single band contribute significantly, the clear choice being the conduction band  $n = c$  when considering conduction electrons. Hence

$$\psi(\mathbf{r}) = \int_{1.\text{Bz}} C_c(\mathbf{k}) U_{c\mathbf{k}}(\mathbf{r}) e^{i\mathbf{k}\cdot\mathbf{r}} d^3k, \quad (2.3)$$

where the integral extends over the first Brillouin zone. An arbitrary crystal momentum can always be shifted to the first Brillouin zone and hence all unique values of  $\mathbf{k}$  occur there. The inverse Fourier transform of the expansion coefficient  $C_c(\mathbf{k})$  is

$$F_c(\mathbf{r}) = \int_{1.\text{Bz}} C_c(\mathbf{k}) e^{i\mathbf{k}\cdot\mathbf{r}} d^3k. \quad (2.4)$$

Provided  $\mathbf{A}(\mathbf{r})$  and  $W(\mathbf{r})$  are slowly varying over length scales comparable to the unit cell (typically  $\sim 0.5$  nm), it can be shown that close to a conduction band minimum  $E_c^0$ , the function  $F_c$  satisfies

$$\left[ \frac{(\mathbf{p} + e\mathbf{A})^2}{2m_e} + W(\mathbf{r}) \right] F_c(\mathbf{r}) = (E - E_c^0) F_c(\mathbf{r}), \quad (2.5)$$

where we assume a diagonal, constant effective mass tensor  $(m_e)_{ii} = m_e$  in the vicinity of the band minimum. In the following, we assume that only one band minimum contributes significantly, an adequate approximation in the vicinity of the  $\Gamma$ -point in InAs.

To see the relation between the function  $F_c(\mathbf{r})$  and the proper wave function  $\psi(\mathbf{r})$ ,



we consider the single-band expansion Eq. (2.3)

$$\psi(\mathbf{r}) = \int_{1.Bz} C_c(\mathbf{k}) U_{c\mathbf{k}}(\mathbf{r}) e^{i\mathbf{k}\cdot\mathbf{r}} d^3k \approx U_{c\mathbf{k}_0}(\mathbf{r}) \int_{1.Bz} C_c(\mathbf{k}) e^{i\mathbf{k}\cdot\mathbf{r}} d^3k = U_{c\mathbf{k}_0}(\mathbf{r}) F_c(\mathbf{r}), \quad (2.6)$$

where we assume that only  $\mathbf{k}$ -values close to the band minimum at  $\mathbf{k}_0$  (i. e.  $E_c(\mathbf{k}_0) = E_c^0$ ) are important and hence approximate  $U_{c\mathbf{k}}(\mathbf{r}) \approx U_{c\mathbf{k}_0}(\mathbf{r})$ . This shows that  $F_c(\mathbf{r})$  corresponds to the wave function  $\psi$  without the rapidly oscillating lattice-periodic part  $U_{c\mathbf{k}}(\mathbf{r})$ . Thus,  $F_c$  modulates the Bloch oscillations of  $\psi$  and determines the qualitative behaviour of the wave function on length scales larger than the unit cell. Accordingly,  $F_c$  is called the envelope function and it is the quantity of interest when modelling conduction electrons in semiconductors. As a result, Eq. (2.5) will be used as the starting point when we introduce the single-electron Hamiltonian in our model. It is the Schrödinger equation of an electron in a magnetic field and external potential  $W(\mathbf{r})$ , with  $m_0$  replaced by the effective electron mass  $m_e$ , and it yields electron energies relative to the shell conduction-band minimum, which will henceforth be denoted simply as  $E - E_c^0 \equiv E$ . Similarly, the envelope functions shall be referred to as wave functions.

## 2.2. The single-electron Hamiltonian

Let us now consider the single-electron Hamiltonian. In the following, we establish the geometry of the system and introduce various effects into the Hamiltonian in succession. We approximate the hexagonal geometry as cylindrical and consider a conduction electron confined to the shell of a cylindrical core-shell nanowire of radius  $r_0$  and length  $L_0$ . We assume negligible wave function leakage into the core and that the shell thickness is small compared to  $r_0$  and  $L_0$ , such that only the lowest radial mode is occupied, and approximate the shell as infinitely thin. In principle,  $r_0$  thus corresponds to the mean radius of the shell and we model the nanowire as a two-dimensional cylindrical surface. In the presence of magnetic field  $\mathbf{B}$  with vector potential  $\mathbf{A}$ , the kinetic energy term is

$$H_0 = \frac{(\mathbf{p} + e\mathbf{A})^2}{2m_e}. \quad (2.7)$$

Here,  $\mathbf{p} = p_\phi \hat{a}_\phi + p_z \hat{a}_z = -i\hbar(\hat{a}_\phi \partial_\phi / r_0 + \hat{a}_z \partial_z)$  in cylindrical coordinates. To model finite cylinder length, we impose hard-wall boundary conditions at the cylinder edges  $z = 0$  and  $z = L_0$ , such that wave functions must vanish there.

If  $\mathbf{B} = 0$ , the Hamiltonian Eq. (2.7) is separable in  $\phi$  and  $z$ . Along the longitudinal direction, it is given by the familiar one-dimensional infinite-square well system

## 2. A quantum mechanical model for closed core-shell nanowires

[19, 20]. Since  $[H_0, L_z] = 0$ , where  $L_z$  is the orbital angular momentum operator, the normalized eigenstates may be written as

$$\begin{aligned}\psi_{np}(\phi, z) &= \langle \mathbf{r} | np \rangle = \sqrt{\frac{1}{\pi r_0 L_0}} \sin\left(\frac{p\pi z}{L_0}\right) e^{in\phi}, \\ E_{np} &= \frac{\hbar^2}{2m_e} \left( \frac{n^2}{r_0^2} + \frac{p^2 \pi^2}{L_0^2} \right), \quad n \in \mathbb{Z}, \quad p \in \mathbb{Z}_+.\end{aligned}\tag{2.8}$$

Thus  $L_z$  is a constant of the motion, i. e. a conserved quantity. Each state, except  $n = 0$ , is doubly degenerate as states of opposite orbital angular momenta  $L_z = \pm \hbar n$  have the same energy. Now suppose we apply a uniform magnetic field in the  $xz$ -plane,  $\mathbf{B} = B_x \hat{a}_x + B_z \hat{a}_z$ . Generally, the solutions are no longer separable and the eigenstates of Eq. (2.7) must be obtained numerically. Let us consider two special cases: a purely transverse ( $\mathbf{B} = B_x \hat{a}_x$ ) and a purely longitudinal ( $\mathbf{B} = B_z \hat{a}_z$ ) magnetic field.

In a uniform, transverse magnetic field  $\mathbf{B} = B_x \hat{a}_x$ , we pick the vector potential  $\mathbf{A}_T = B_x y \hat{a}_z = B_x r_0 \sin(\phi) \hat{a}_z$ . Inserting into Eq. (2.7) and expanding the bracket yields

$$H_0 = \frac{p_\phi^2 + p_z^2}{2m_e} + r_0 \omega_c^x \sin(\phi) p_z + \frac{\hbar \omega_c^x}{2} \frac{r_0^2}{(l_B^x)^2} \sin^2(\phi),\tag{2.9}$$

where  $\omega_c^x = eB_x/m_e$  and  $l_B^x = \sqrt{\hbar/(eB_x)}$  are the cyclotron frequency and magnetic length due to  $B_x$ , respectively. Because of the coupling between  $\sin(\phi)$  and  $p_z$ , the Hamiltonian is indeed not separable and the eigenstates must be obtained numerically. Furthermore,  $L_z$  and  $H_0$  no longer commute so orbital angular momentum is no longer conserved.

For a physical picture of the effects of a transverse magnetic field on a conduction electron, it is instructive to consider an infinitely-long cylinder. One can then construct eigenstates common to  $H_0$  and  $p_z$ , which simplifies matters significantly. Such a procedure does not work on the finite cylinder, as one is quick to see from the axial part in Eq. (2.8). On the infinite cylinder,  $[H_0, p_z] = 0$  and we may pick eigenstates with definite longitudinal momenta,  $p_z = \hbar k$  where  $k \in \mathbb{R}$ . As a result, the single-electron Hamiltonian Eq. (2.9) becomes

$$\begin{aligned}H_0 &= \frac{p_\phi^2 + \hbar^2 k^2}{2m_e} + k r_0 \hbar \omega_c^x \sin(\phi) + \frac{\hbar \omega_c^x}{2} \frac{r_0^2}{(l_B^x)^2} \sin^2(\phi) \\ &= \frac{p_\phi^2}{2m_e} + \frac{1}{2m_e} (\hbar k + e B_x r_0 \sin(\phi))^2 \\ &= \frac{p_\phi^2}{2m_e} + \frac{\hbar^2 r_0^2}{2m_e (l_B^x)^4} \left( \frac{k (l_B^x)^2}{r_0} + \sin(\phi) \right)^2,\end{aligned}\tag{2.10}$$

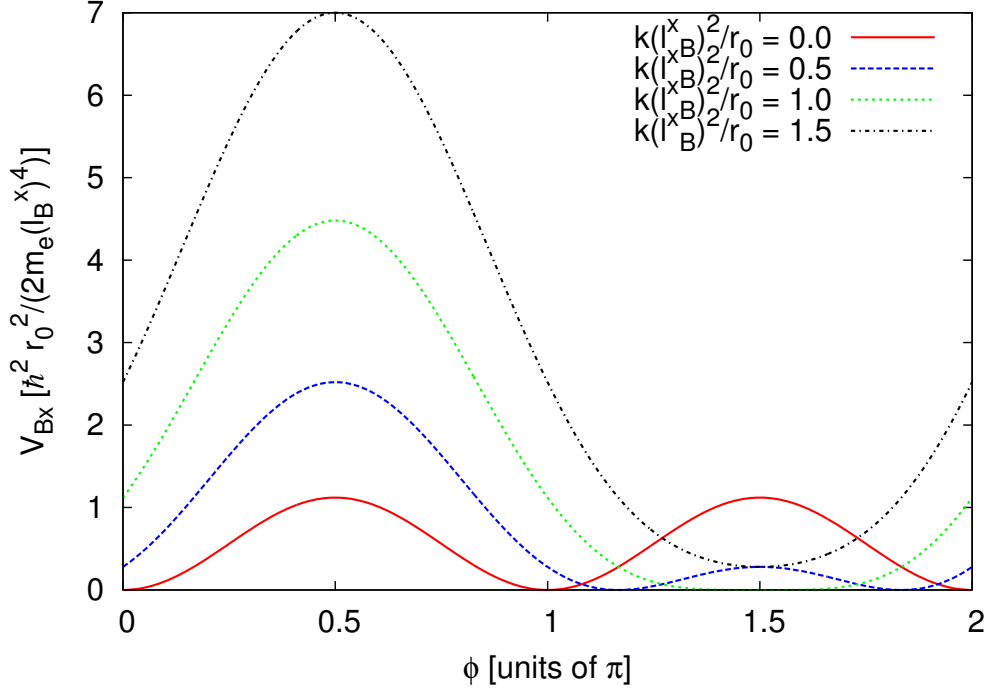


Figure 2.1: Effective magnetic potential  $V_{Bx}(\phi)$  evaluated for different values of  $k(l_B^x)^2/r_0$ . At small  $k(l_B^x)^2/r_0$ , minima at  $\phi = 0$  and  $\phi = \pi$  may produce localized cyclotron states. As  $k(l_B^x)^2/r_0$  increases, extrema form at points where the projection  $B_x \cos(\phi)$  vanishes, producing stable equilibrium points at the potential minimum, e. g. at  $\phi = 3\pi/2$  for  $k > 0$ .

where we identify the effective magnetic potential

$$V_{Bx}(\phi) = \frac{\hbar^2 r_0^2}{2m_e (l_B^x)^4} \left( \frac{k(l_B^x)^2}{r_0} + \sin(\phi) \right)^2. \quad (2.11)$$

Figure 2.1 shows  $V_{Bx}(\phi)$  evaluated for different values of the dimensionless quantity  $k(l_B^x)^2/r_0$ . Assuming a fixed, positive value of  $B_x$ ,  $k(l_B^x)^2/r_0$  increases linearly with the momentum quantum number  $k$ , and so large values of  $k(l_B^x)^2/r_0$  correspond to large values of  $p_z$ . For small  $k(l_B^x)^2/r_0$ , we see minima in  $V_{Bx}$  around the angles  $\phi = 0$  and  $\phi = \pi$ . These points correspond to the maxima in the perpendicular projection  $B_x \cos(\phi)$  onto the curved cylinder surface. Classically, electrons thus experience a strong Lorentz force there, given by  $\mathbf{F} = -e(\mathbf{v} \times \mathbf{B})$ , where  $\mathbf{v}$  is the electron velocity. The interplay between angular and longitudinal motion may lead to the formation of localized cyclotron states there. As  $k(l_B^x)^2/r_0$  increases, a minimum forms at  $\phi = 3\pi/2$  and a maximum at  $\phi = \pi/2$ . At these points, the perpendicular projection  $B_x \cos(\phi)$  onto the cylinder surface vanishes, and so electrons experience no Lorentz force there classically. Slight deviations from these two angular points however produce a non-vanishing projection  $B_x \cos(\phi)$  and the

## 2. A quantum mechanical model for closed core-shell nanowires

Lorentz force reappears. Since the Lorentz force involves a cross product of the electron velocity, the force orientation depends on their direction of propagation. By considering  $k(l_B^x)^2/r_0 \geq 0$  and presupposing  $B_x > 0$ , we have inherently assumed that  $k \geq 0$ , i. e. electrons are propagating in the direction of  $+z$ . As a result, a slight angular deviation from  $\phi = \pi/2$  will produce a Lorentz force pulling the electron away from that angle, and therefore it is an unstable equilibrium point. On the other hand, an electron that deviates slightly from the angle  $\phi = 3\pi/2$  will experience a Lorentz force pushing it back into  $\phi = 3\pi/2$  making it a stable equilibrium point. This produces a snaking-like motion along  $z$  and such quantum mechanical states are called snake orbits. Similarly, electrons with  $k < 0$  will have a potential minimum at  $\phi = \pi/2$ , and so it is around  $\phi = \pi/2$  and  $\phi = 3\pi/2$  that we expect to find snaking orbits. On the surface of a cylinder of finite length, this physical picture is complicated by edge effects, because edge currents link to the snaking orbits. Nevertheless, we expect to see qualitative snake and cyclotron orbits on the finite cylinder as well [14, 15, 21].

Now suppose we instead apply a uniform, longitudinal field  $\mathbf{B} = B_z \hat{a}_z$ . We pick the vector potential  $\mathbf{A}_L = \hat{a}_\phi r_0 B_z / 2$  and obtain from Eq. (2.7) the single-electron Hamiltonian

$$H_0 = \frac{1}{2m_e} \left[ \left( \frac{\hbar}{ir_0} \partial_\phi + \frac{eB_z r_0}{2} \right)^2 + \left( \frac{\hbar}{i} \partial_z \right)^2 \right] = \frac{\hbar^2}{2m_e} \left[ \frac{1}{r_0^2} \left( \frac{\partial_\phi}{i} + \frac{\Phi}{\Phi_0} \right)^2 + \left( \frac{\partial_z}{i} \right)^2 \right], \quad (2.12)$$

where  $\Phi = \pi B_z r_0^2$  is the longitudinal magnetic flux piercing the cylinder and  $\Phi_0 = h/e$  the magnetic flux quantum. The magnetic field only couples to the angular part of the Hamiltonian, so the axial part is once again the infinite square well. Furthermore, the Hamiltonian still commutes with  $L_z$  and we can construct simultaneous eigenstates of  $H_0$  and  $L_z$ . It follows that the eigenstates are given by

$$\begin{aligned} \psi_{np}(\phi, z) &= \langle \mathbf{r} | np \rangle = \sqrt{\frac{1}{\pi r_0 L}} \sin\left(\frac{p\pi z}{L}\right) e^{in\phi}, \\ E_{np} &= \frac{\hbar^2}{2m_e r_0^2} \left[ \left( n + \frac{\Phi}{\Phi_0} \right)^2 + p^2 \frac{r_0^2}{L^2} \right], \end{aligned} \quad (2.13)$$

where  $n \in \mathbb{Z}$  and  $p \in \mathbb{Z}_+$  as before. The spectrum is periodic in  $\Phi$  with the period  $\Phi = \Phi_0$ . Increasing  $\Phi$  by  $\Phi_0$  amounts to reducing the angular momentum of a given eigenstate by  $\hbar$ :  $L_z = \hbar n \rightarrow \hbar(n - 1)$ . Since the ground state has  $L_z = 0$  when  $\Phi = 0$ , it follows that the ground state has nonzero  $L_z$  for  $\Phi > \Phi_0/2$  [22, 23].

The flux-periodic oscillations in the spectrum arise because the wave functions enclose a magnetic flux [12]. They are reminiscent of the Aharonov-Bohm oscillations, a quantum-mechanical interference phenomenon which arises because wave functions that enclose a magnetic flux acquire a flux-dependent phase shift [24]. Flux-periodic oscillations in rings have indeed been observed experimentally, for example in the

resistance [25] and magnetization [26]. A couple of theoretical papers have addressed flux-periodic oscillations in core-shell systems [27, 28] and later, magnetoresistance measurements on core-shell nanowires revealed the existence of flux-periodic oscillations [9]. Recently, they were shown to manifest because transport is mediated by closed-loop states encircling the core, tying the oscillations to those observed in the spectrum [11].

To account for both transverse and longitudinal magnetic fields simultaneously, we simply add the corresponding vector potentials

$$\mathbf{A} = \mathbf{A}_T + \mathbf{A}_L = \frac{r_0 B_z}{2} \hat{a}_\phi + r_0 B_x \sin(\phi) \hat{a}_z. \quad (2.14)$$

The corresponding Hamiltonian is a combination of Eqs. (2.9) and (2.12), namely

$$H_0 = \frac{\hbar^2}{2m_e} \left[ \frac{1}{r_0^2} \left( \frac{\partial_\phi}{i} + \frac{\Phi}{\Phi_0} \right)^2 + \left( \frac{\partial_z}{i} \right)^2 \right] + r_0 \omega_c^x \sin(\phi) p_z + \frac{\hbar \omega_c^x}{2} \frac{r_0^2}{(l_B^x)^2} \sin^2(\phi). \quad (2.15)$$

Electrons are fermions and so, in addition to orbital angular momentum, they possess an intrinsic angular momentum called spin. Electron spin is described by the observable  $\mathbf{S} = \frac{\hbar}{2} \boldsymbol{\sigma}$ , which is formally an angular momentum with quantum number  $s = 1/2$  [19, 20]. Along a given quantization axis, two projections ( $\pm \hbar/2$ ) are allowed. Typically, states with definite spin projections along the  $z$ -axis, i. e. the eigenspinors of  $S_z$ , are used as a basis for spin space. Electron spin constitutes an intrinsic magnetic moment, which interacts with external magnetic fields. This interaction is described by the Zeeman Hamiltonian  $H_Z = g_e e \hbar \boldsymbol{\sigma} \cdot \mathbf{B} / (4m_0)$  which in our case reads

$$H_Z = \frac{\hbar g_e m^*}{4} (\omega_c^x \sigma_x + \omega_c^z \sigma_z). \quad (2.16)$$

Here,  $g_e$  is the effective conduction electron  $g$ -factor of the semiconductor in question. In the special case of a purely longitudinal (transverse) field,  $\sigma_z$  ( $\sigma_x$ ) is a constant of the motion of the Hamiltonian  $H_0 + H_Z$ .

Electron spin can also couple to orbital observables resulting in spin-orbit interaction (SOI), which plays an important role in many semiconductors. By considering a low-energy limit of the Dirac equation for relativistic fermions, one can show that an SOI term called Pauli SOI arises in the presence of a potential gradient  $\nabla V$  [13]

$$H_{\text{Pauli}} = \frac{e \hbar}{4m_0^2 c^2} (\nabla V \times \mathbf{p}_k) \cdot \boldsymbol{\sigma}. \quad (2.17)$$

This form can also be argued for using special relativity by considering an electron moving in an electric potential due to the electric field  $\mathbf{E}_0 = -\nabla V$ . An electron moving in an electric field with velocity  $\mathbf{v}$  will feel a magnetic field  $\mathbf{B} = -\mathbf{v} \times \mathbf{E}_0 / c$  [29], which in turn couples to the intrinsic spin magnetic moment of the electron,

## 2. A quantum mechanical model for closed core-shell nanowires

resulting in a term coupling the orbital observables  $\mathbf{v}$  and  $\mathbf{E}_0$  with spin [20]. Here, we will consider two types of SOI that manifest in semiconductors: Rashba and Dresselhaus SOI. Let us discuss the Rashba term first, as it can be qualitatively derived from Pauli SOI [Eq. (2.17)]. In Chapter 1, we discussed the appearance of a confining electric field in core-shell nanowires, due to modulation doping of the core. In a cylindrical geometry it is oriented approximately radially and hence we set  $\mathbf{E}_0 = -E_0 \hat{a}_r = -\nabla V$ . Inserting into the Pauli SOI term Eq. (2.17) yields

$$\begin{aligned} H_{\text{Pauli}} &= \frac{e\hbar}{4m_0^2 c^2} (E_0 \hat{a}_r \times \mathbf{p}_k) \cdot \boldsymbol{\sigma} = \frac{eE_0 \hbar}{4m_0^2 c^2} (\hat{a}_r \times \mathbf{p}_k) \cdot \boldsymbol{\sigma} \\ &= \frac{eE_0 \hbar}{4m_0^2 c^2} (\mathbf{p}_k \times \boldsymbol{\sigma}) \cdot \hat{a}_r \end{aligned} \quad (2.18)$$

by cyclic permutation of the scalar triple product. Setting  $m_0 \rightarrow m_e$  and renaming the coefficient in the front  $\alpha_R$ , we obtain the qualitative Rashba SOI Hamiltonian in core-shell geometry [30, 31]

$$H_R = \alpha_R (\mathbf{p}_k \times \boldsymbol{\sigma}) \cdot \hat{a}_r = \frac{\alpha_R}{\hbar} [\sigma_\phi (p_z + eA_z) - \sigma_z (p_\phi + eA_\phi)], \quad (2.19)$$

where  $\sigma_\phi = \cos(\phi)\sigma_y - \sin(\phi)\sigma_x$  describes the spin projection along the angular direction. While the preceding derivation captures the essence of Rashba SOI, such as the coupling to external electric fields, it provides a poor estimation of  $\alpha_R$ , which requires a more detailed analysis based on group theory [13]. The Hamiltonian  $H_R$  in Eq. (2.19) is nonetheless qualitatively correct. Dresselhaus SOI arises in semiconductors if the unit cell lacks a spatial inversion center [13]. In a cylindrical core-shell geometry, the Dresselhaus SOI Hamiltonian is given by [15]

$$H_D = \frac{\beta_D}{\hbar} \left[ \frac{1}{2} \{ \sigma_\phi (p_\phi + eA_\phi) + (p_\phi + eA_\phi) \sigma_\phi \} - \sigma_z (p_z + eA_z) \right], \quad (2.20)$$

where  $\beta_D$  is a material- and geometry-dependent parameter which determines the SOI strength. In bulk, InAs is known to lack an inversion center due to its zincblende crystal structure. Growing InAs into nanowires furthermore results in structural changes in the lattice such that the crystal structure becomes wurtzite, the unit cell of which indeed lacks a spatial inversion center [32]. While Rashba SOI can generally be tuned, for example by varying doping or gate voltages [33–36], Dresselhaus SOI is essentially a fixed property of a given sample [13]. Since  $[p_\phi, \sigma_\phi] \neq 0$  the first term has been symmetrized to ensure the hermicity of  $H_D$ .

Suppose we apply a static electric field transverse to the cylinder  $\mathbf{E}_T = E_x \hat{a}_x$ . Since  $\mathbf{E}_T = -\nabla V_T$  is static, we pick the electric potential  $V_T = -E_x x$  in which electrons have the electrostatic potential energy  $U = eE_x x$ . The Hamiltonian describing the coupling of  $\mathbf{E}_T$  to conduction electrons is thus

$$H_{E_x} = eE_x x = eE_x r_0 \cos(\phi). \quad (2.21)$$

Evidently,  $H_{E_x}$  does not commute with  $L_z$  and, since it only couples to the angular part of the Hamiltonian, the longitudinal part of electron wave functions remains unaffected.

The most general form of the single-electron Hamiltonian  $H_S$  for shell conduction electrons under consideration in this work is given by a sum of all of the terms discussed in this section, namely

$$H_S = H_O + H_Z + H_R + H_D + H_{E_x}, \quad (2.22)$$

where the various terms are given in Eqs. (2.15), (2.16), (2.19), (2.20) and (2.21), and  $\mathbf{A}$  is given in Eq. (2.14). The spectrum and eigenstates of  $H_S$  are obtained by solving the time-independent Schrödinger equation

$$H_S|\alpha\rangle = \epsilon_\alpha^S|\alpha\rangle. \quad (2.23)$$

When an analytical solution is not possible, this is done numerically by constructing the matrix of  $H_S$  in the basis of eigenstates of  $H_0$  with  $\mathbf{B} = 0$  [Eq. (2.8)]. For spin space, we use the basis composed of eigenspinors of  $\sigma_z$ . Hence, we denote the basis elements by  $\{|nps\rangle\}$  where  $n$  and  $p$  are as in Eq. (2.8) and  $s = \pm 1$  describes the spin projection along  $z$ . Actually, in Chapter 6 the Hamiltonian will also include contributions from static impurities in the core. We neglect electron-electron interaction in this work. In the following, we will analyze the effects of the various terms on closed-system properties such as the spectrum and densities, which will be discussed in the next section. Usually, we will only consider a few of the terms in Eq. (2.22) simultaneously.

## 2.3. Densities and the chemical potential

Densities give insight into how the various properties of conduction electrons vary over the cylinder surface. We are interested in how the terms discussed in Sec. 2.2 affect electron and current densities, as well as spin orientations, locally. The electron charge density and charge current density operators  $\hat{\rho}(\mathbf{r}')$  and  $\hat{\mathbf{j}}(\mathbf{r}')$  are defined as [37]

$$\begin{aligned} \hat{\rho}(\mathbf{r}') &= -e\delta(\mathbf{r}' - \mathbf{r}), \\ \hat{\mathbf{j}}(\mathbf{r}') &= -\frac{e}{2} [\mathbf{v}\delta(\mathbf{r}' - \mathbf{r}) + \delta(\mathbf{r}' - \mathbf{r})\mathbf{v}], \end{aligned} \quad (2.24)$$

where  $\mathbf{v}$  is the velocity operator. It is derived from  $H_S$  [Eq. (2.22)] using the Heisenberg equation of motion, namely

$$\mathbf{v} = \frac{d\mathbf{r}}{dt} = \frac{i}{\hbar} [H_S, \mathbf{r}], \quad (2.25)$$

## 2. A quantum mechanical model for closed core-shell nanowires

where operators are in the Heisenberg picture. We note that since  $H_S$  is time-independent, it commutes with the time-evolution operator

$$U(t, t_0) = e^{-i\frac{H_S}{\hbar}(t-t_0)}. \quad (2.26)$$

Hence,  $U^\dagger H_S U = H_S$  and  $H_S$  is thus equivalent in both Schrödinger and Heisenberg pictures. In Eq. (2.24),  $\mathbf{r}'$  is the coordinate at which the density is evaluated and  $\mathbf{r}$  the electron coordinate. Note that generally  $\mathbf{v}$  does not commute with the coordinate  $\delta$ -functions, which is why  $\hat{\mathbf{j}}(\mathbf{r}')$  has been symmetrized to ensure hermicity. Similarly, the spin density operator is

$$\hat{\mathbf{S}}(\mathbf{r}') = \mathbf{S}\delta(\mathbf{r}' - \mathbf{r}), \quad (2.27)$$

where  $\mathbf{S} = \frac{\hbar}{2}\boldsymbol{\sigma} = \frac{\hbar}{2}(\sigma_x\hat{a}_x + \sigma_y\hat{a}_y + \sigma_z\hat{a}_z)$ . For a given eigenstate of  $H_S$ ,  $\langle\mathbf{r}|\alpha\rangle = \Psi_\alpha^S(\mathbf{r})$ , the charge, charge current and spin densities are obtained by taking the expectation values of the corresponding operators [Eqs. (2.24) and (2.27)], namely

$$\begin{aligned} \rho_\alpha(\mathbf{r}) &= \langle\alpha|\hat{\rho}|\alpha\rangle = -e\Psi_\alpha^{S\dagger}(\mathbf{r})\Psi_\alpha^S(\mathbf{r}), \\ \mathbf{j}_\alpha(\mathbf{r}) &= \langle\alpha|\hat{\mathbf{j}}|\alpha\rangle = \int \Psi_\alpha^{S\dagger}(\mathbf{r}')\hat{\mathbf{j}}(\mathbf{r}')\Psi_\alpha^S(\mathbf{r}')d\mathbf{r}', \\ \mathbf{S}_\alpha(\mathbf{r}) &= \langle\alpha|\hat{\mathbf{S}}|\alpha\rangle = \frac{\hbar}{2}\Psi_\alpha^{S\dagger}(\mathbf{r})\boldsymbol{\sigma}\Psi_\alpha^S(\mathbf{r}), \end{aligned} \quad (2.28)$$

where the integral extends over the cylinder surface. We note that on a cylindrical surface of radius  $r_0$ , the  $\delta$ -function should be taken as

$$\delta(\mathbf{r}) = \frac{1}{r_0}\delta(\phi)\delta(z), \quad (2.29)$$

which clearly satisfies  $\int \delta(\mathbf{r})d\mathbf{r} = 1$ .

In a non-interacting system at zero temperature, placing  $N_e$  electrons in the closed system will fill up the  $N_e$  energetically-lowest states. The densities  $\rho(\mathbf{r})$ ,  $\mathbf{j}(\mathbf{r})$  and  $\mathbf{S}(\mathbf{r})$  are then obtained by summing up the contributions of occupied states [Eq. (2.28)]. At finite temperatures  $T$ , nonzero electron thermal energy results in finite occupation probabilities of higher-energy states. In thermal equilibrium, the occupation probability is given by the temperature- and energy-dependent Fermi-Dirac distribution function [38]

$$f(E, \mu, T) = \frac{1}{\exp\left(\frac{E-\mu}{k_B T}\right) + 1}, \quad (2.30)$$

where  $E$  is the energy at which the probability is evaluated,  $\mu$  the system chemical potential and  $k_B$  Boltzmann's constant. The chemical potential  $\mu$  relates to the flow of charge in the system, i. e. spatial variations in  $\mu$  means that the system is out of equilibrium. Currents then flow in order to restore equilibrium in the form



of a constant  $\mu$  throughout the system [16, 17, 38]. We will assume that the closed system is in thermal equilibrium. In the limit  $T \rightarrow 0$  K,  $\mu$  is simply the energy of the energetically-highest occupied state. At arbitrary  $T$ , the equilibrium densities of noninteracting electrons are obtained by summing up the contributions of individual eigenstates [Eq. (2.28)] multiplied by their occupation probabilities [Eq. (2.30)]

$$\begin{aligned}\rho(\mathbf{r}) &= \sum_{\alpha} \rho_{\alpha}(\mathbf{r}) f(\epsilon_{\alpha}^S, \mu, T), \\ \mathbf{j}(\mathbf{r}) &= \sum_{\alpha} \mathbf{j}_{\alpha}(\mathbf{r}) f(\epsilon_{\alpha}^S, \mu, T), \\ \mathbf{S}(\mathbf{r}) &= \sum_{\alpha} \mathbf{S}_{\alpha}(\mathbf{r}) f(\epsilon_{\alpha}^S, \mu, T).\end{aligned}\tag{2.31}$$

The chemical potential of  $N_e$  electrons follows from integrating  $-\rho(\mathbf{r})/e$  in Eq. (2.31) over the closed system, which yields the electron number  $N_e$

$$N_e = \sum_{\alpha} f(\epsilon_{\alpha}^S, \mu, T),\tag{2.32}$$

and can be solved for  $\mu$  numerically for a given  $N_e$ .

## 2.4. Symmetries

Let us discuss rotational and space inversion (parity) symmetries, which are powerful tools for analyzing the effects of the various terms introduced in Sec. 2.2. In quantum mechanics, the total angular momentum operator  $\mathbf{J} = \mathbf{L} + \mathbf{S}$  is the generator of infinitesimal rotations. Finite rotations of state kets are obtained by applying the rotation operator [20]

$$D(\mathbf{n}, \theta) = e^{-i \frac{\mathbf{J} \cdot \mathbf{n}}{\hbar} \theta},\tag{2.33}$$

which rotates by the finite angle  $\theta$  around the axis defined by the unit vector  $\mathbf{n}$ . Due to the cylindrical geometry, we are primarily interested in the special case  $\mathbf{n} = \hat{a}_z$ , i. e. the operator

$$D_z(\theta) = e^{-i \frac{J_z}{\hbar} \theta},\tag{2.34}$$

which will be called the rotation operator henceforth in this work. Since  $J_z = L_z + S_z$ , the rotation operator can be decomposed into a product of two operators

$$D_z(\theta) = e^{-i \frac{J_z}{\hbar} \theta} = e^{-i \frac{L_z}{\hbar} \theta} e^{-i \frac{S_z}{2} \theta} \equiv D_{zO} D_{zS},\tag{2.35}$$

which correspond to rotations in orbital (O) and spin (S) space, respectively. Evidently,  $[D_{zO}, D_{zS}] = 0$  since the operators act on different subspaces. Under rotation, the expectation value of an observable  $A$  transforms as

$$\langle \psi | A | \psi \rangle \xrightarrow{\text{Rotation}} \langle \psi | D_z^{\dagger} A D_z | \psi \rangle,\tag{2.36}$$

## 2. A quantum mechanical model for closed core-shell nanowires

where  $|\psi\rangle$  is an arbitrary ket. Rotation is thus equivalent to transforming  $A$  as

$$A \xrightarrow{\text{Rotation}} D_z^\dagger A D_z. \quad (2.37)$$

If  $[D_z, A] = 0$ , it follows that  $D_z^\dagger A D_z = D_z^\dagger D_z A = A$  since  $D_z$  is unitary [19, 20], and  $A$  is thus rotationally invariant.

Suppose  $H_S$  is rotationally invariant and let us discuss the implications for the eigenstates  $|\alpha\rangle$ . Since  $[H_S, D_z] = 0$  one has

$$H_S(D_z|\alpha\rangle) = D_z H_S|\alpha\rangle = \epsilon_\alpha^S(D_z|\alpha\rangle), \quad (2.38)$$

which shows that a rotated eigenket remains an eigenket of  $H_S$  with the same eigenvalue [Eq. (2.22)]. More can be asserted if we focus on two special cases. First of all, let us assume that the spectrum of  $H_S$  is nondegenerate, such that a single linearly-independent eigenket corresponds to each eigenvalue  $\epsilon_\alpha^S$ . Since Eq. (2.38) shows that  $D_z|\alpha\rangle$  and  $|\alpha\rangle$  are eigenstates of  $H_S$  with the same eigenvalue, they are the same state, differing at most by a complex coefficient,  $D_z|\alpha\rangle = C|\alpha\rangle$ . But rotation conserves normalization,  $\langle\alpha|D_z^\dagger D_z|\alpha\rangle = \langle\alpha|\alpha\rangle$ , so the complex coefficient is simply a phase factor  $C = e^{i\gamma}$ , where  $\gamma \in \mathbb{R}$ . Secondly, we assume that  $|\alpha\rangle$  is an eigenket common to  $J_z$  and  $H_S$  and the energy level  $\epsilon_\alpha^S$  thus possibly degenerate. Assuming that  $J_z|\alpha\rangle = j_\alpha|\alpha\rangle$ , rotating  $|\alpha\rangle$  yields

$$D_z|\alpha\rangle = \sum_{n=0}^{\infty} \frac{1}{n!} \left(-i \frac{J_z}{\hbar} \theta\right)^n |\alpha\rangle = \sum_{n=0}^{\infty} \frac{1}{n!} \left(-i \frac{j_\alpha}{\hbar} \theta\right)^n |\alpha\rangle = e^{-i \frac{j_\alpha}{\hbar} \theta} |\alpha\rangle \equiv e^{i\gamma} |\alpha\rangle, \quad (2.39)$$

where we Taylor expanded the exponential [Eq. (2.34)]. Again, we see that rotation leaves the state  $|\alpha\rangle$  invariant up to a phase factor. In summary, we have shown that for a rotationally invariant  $H_S$  with a nondegenerate spectrum or eigenstates chosen common to  $H_S$  and  $J_z$ , rotation leaves the eigenstates invariant up to a phase factor

$$|\alpha\rangle \xrightarrow{\text{Rotation}} D_z|\alpha\rangle = e^{i\gamma} |\alpha\rangle. \quad (2.40)$$

We can apply this to analyze the densities in Eq. (2.31). The densities are all sums over terms of the form  $A_\alpha(\mathbf{r}) = \langle\alpha|A\delta(\mathbf{r}' - \mathbf{r})|\alpha\rangle$ , where  $A$  is an observable or the identity operator, which is hermitian anyway. We start by checking how rotations affect the  $\delta$ -function. Using Eq. (2.35), for an arbitrary ket  $|\psi\rangle$  one finds

$$\langle\psi|D_z^\dagger \delta(\mathbf{r}' - \mathbf{r}) D_z|\psi\rangle = \langle\psi|D_{zO}^\dagger D_{zS}^\dagger \delta(\mathbf{r}' - \mathbf{r}) D_{zO} D_{zS}|\psi\rangle. \quad (2.41)$$

The  $\delta$ -function depends only on orbital quantities and hence commutes with  $D_{zS}$ , which only acts in spin space. Therefore

$$D_{zO}^\dagger D_{zS}^\dagger \delta(\mathbf{r}' - \mathbf{r}) D_{zO} D_{zS} = D_{zO}^\dagger \delta(\mathbf{r}' - \mathbf{r}) D_{zO}, \quad (2.42)$$

and one obtains

$$\begin{aligned}
\langle \psi | D_z^\dagger \delta(\mathbf{r}' - \mathbf{r}) D_z | \psi \rangle &= \langle \psi | D_{zO}^\dagger \delta(\mathbf{r}' - \mathbf{r}) D_{zO} | \psi \rangle \\
&= \int \psi^\dagger(\phi', z') D_{zO}^\dagger \delta(\mathbf{r}' - \mathbf{r}) D_{zO} \psi(\phi', z') r_0 d\phi' dz' \\
&= \int \psi^\dagger(\phi' + \theta, z') \delta(\mathbf{r}' - \mathbf{r}) \psi(\phi' + \theta, z') r_0 d\phi' dz' \\
&= \psi^\dagger(\phi + \theta, z) \psi(\phi + \theta, z),
\end{aligned} \tag{2.43}$$

where we have used the  $\delta$ -function [Eq. (2.29)] and the fact that  $D_{zO}$  rotates wave functions in coordinate space [19, 20]. Comparing the first and fourth lines shows that

$$D_z^\dagger \delta(\mathbf{r}' - \mathbf{r}) D_z = \frac{1}{r_0} \delta(\phi' - [\phi + \theta]) \delta(z' - z) \equiv \delta(\mathbf{r}' - \mathbf{r}_{\text{rot}}), \tag{2.44}$$

i. e. the coordinate vector  $\mathbf{r} = (z, \phi)$  has been rotated into  $\mathbf{r}_{\text{rot}} = (z, \phi + \theta)$ . Let us now analyze an arbitrary density  $A_\alpha(\mathbf{r})$  under rotation. We assume that rotation leaves the eigenkets  $|\alpha\rangle$  invariant up to a phase factor, as discussed before. Since  $D_z^\dagger D_z = 1$  one obtains

$$\begin{aligned}
A_\alpha(\mathbf{r}) &= \langle \alpha | A \delta(\mathbf{r}' - \mathbf{r}) | \alpha \rangle = \langle \alpha | D_z D_z^\dagger A D_z D_z^\dagger \delta(\mathbf{r}' - \mathbf{r}) D_z D_z^\dagger | \alpha \rangle \\
&= \langle \alpha | e^{i\gamma} D_z^\dagger A D_z D_z^\dagger \delta(\mathbf{r}' - \mathbf{r}) D_z e^{-i\gamma} | \alpha \rangle = \langle \alpha | D_z^\dagger A D_z \delta(\mathbf{r}' - \mathbf{r}_{\text{rot}}) | \alpha \rangle,
\end{aligned} \tag{2.45}$$

where we have used Eq. (2.40) and the analogue for  $D_z^\dagger$ . If  $A$  is rotationally invariant, then  $D_z^\dagger A D_z = D_z^\dagger D_z A = A$  and we find

$$A_\alpha(\mathbf{r}) = \langle \alpha | D_z^\dagger A D_z \delta(\mathbf{r}' - \mathbf{r}_{\text{rot}}) | \alpha \rangle = \langle \alpha | A \delta(\mathbf{r}' - \mathbf{r}_{\text{rot}}) | \alpha \rangle = A_\alpha(\mathbf{r}_{\text{rot}}), \tag{2.46}$$

which shows that the density  $A_\alpha(\mathbf{r})$  is invariant under rotations, because the angle  $\theta$  is arbitrary. It then immediately follows that  $A(\mathbf{r}) = \sum_\alpha A_\alpha(\mathbf{r}) f(\epsilon_\alpha^S, \mu, T)$  is rotationally invariant, i. e.  $A(\mathbf{r})$  manifests as concentric circles of constant density. This can be applied to the densities in Eq. (2.28). For example, in  $S_z(\mathbf{r})$  and  $\rho(\mathbf{r})$  the operator  $A$  corresponds to  $S_z$  and 1 respectively, both of which are rotationally invariant. On the other hand, in  $S_x(\mathbf{r})$  and  $S_y(\mathbf{r})$  the corresponding operators are not rotationally invariant. As the velocity operator  $\mathbf{v}$  is derived from  $H_S$  [Eq. (2.25)], the transformation properties of  $\mathbf{j}(\mathbf{r})$  depend on which terms are included, as discussed in Sec. 2.2.

Space-inversion of states is obtained by applying the unitary parity operator  $P$ , which fundamentally is taken to invert the expectation value of the coordinate operator  $\mathbf{r}$ . The parity transformations of the operators  $\mathbf{r}$ ,  $\mathbf{p}$  and  $\mathbf{J}$  in a cartesian coordinate system follow from this and are given by [20]

$$\begin{aligned}
P^\dagger \mathbf{r} P &= -\mathbf{r} \Leftrightarrow \{P, \mathbf{r}\} = 0, \\
P^\dagger \mathbf{p} P &= \mathbf{p} \Leftrightarrow \{P, \mathbf{p}\} = 0, \\
P^\dagger \mathbf{J} P &= \mathbf{J} \Leftrightarrow [P, \mathbf{J}] = 0.
\end{aligned} \tag{2.47}$$

## 2. A quantum mechanical model for closed core-shell nanowires

Physically, a parity transformation thus mirrors coordinates over the origin and reverses momentum, but leaves angular momentum unchanged. An observable  $A$  is even (odd) under parity if  $P^\dagger A P = +(-)A$ . Inverting a state twice yields the original state up to a phase factor and hence  $P^2 = 1$ . Since  $P$  is unitary, it follows that  $P^2 = 1 = P^\dagger P$  and so

$$P^\dagger = P^{-1} = P. \quad (2.48)$$

Eigenkets of  $P$  satisfy  $P^2|\psi\rangle = \lambda^2|\psi\rangle \Leftrightarrow \lambda^2 = 1$  and so  $\lambda = \pm 1$ . Parity eigenkets with  $\lambda = 1$  are said to have even parity and eigenkets with  $\lambda = -1$  odd parity. In coordinate representation, parity eigenstates with even (odd) parity manifest as even (odd) functions relative to the inversion center. A very useful theorem exists regarding the parity of energy eigenkets. It states that provided  $[H_S, P] = 0$ , a nondegenerate eigenket  $|\alpha\rangle$  of  $H_S$  is also a parity eigenket [19, 20].

Let us discuss how the parity operator applies in a cylindrical geometry. The transformation properties listed in Eq. (2.47) assume a system with an inversion center at the origin. However, we have restricted the finite cylinder length to  $0 \leq z \leq L_0$ , which intuitively means that the inversion center should be located in the plane  $z = L_0/2$ , such that an inversion of the  $z$ -coordinate should mirror it over the plane  $z = L_0/2$ . More formally, we wish to show that

$$P_z z P_z = L_0 - z, \quad (2.49)$$

for a finite cylinder  $0 \leq z \leq L_0$ , where  $P_z$  is the longitudinal part of the parity operator, inverting only the  $z$ -coordinate. To show this, consider a finite cylinder on the interval  $-L_0/2 \leq z \leq L_0/2$ , which has an inversion center at the origin. Hence Eq. (2.47) applies directly, i. e.

$$P_z z P_z = -z. \quad (2.50)$$

We make a change of variables  $z' = z + L_0/2$ , such that  $0 \leq z' \leq L_0$ , and find

$$P_z \left( z' - \frac{L_0}{2} \right) P_z = - \left( z' - \frac{L_0}{2} \right) \Leftrightarrow P_z z P_z = L_0 - z, \quad (2.51)$$

which shows that the inversion plane has been shifted to  $z = L_0/2$ , proving Eq. (2.49). Inversion on the cylinder surface in a plane perpendicular to the  $z$ -axis clearly leaves the radius  $r_0$  unchanged and yields

$$\begin{aligned} P_x x P_x = -x &\Leftrightarrow P_x r_0 \cos(\phi) P_x = -r_0 \cos(\phi), \\ P_y y P_y = -y &\Leftrightarrow P_y r_0 \sin(\phi) P_y = -r_0 \sin(\phi), \end{aligned} \quad (2.52)$$

which is accomplished by the transformation  $\phi \rightarrow \phi + \pi$ . One might also have guessed this transformation from a geometrical point of view, as it corresponds to an inversion over the origin in the plane. To summarize, parity transformations of coordinates in our cylindrical geometry are given by

$$\begin{aligned} \phi &\xrightarrow{\text{Parity}} \phi + \pi, \\ z &\rightarrow L_0 - z. \end{aligned} \quad (2.53)$$

Suppose  $[H_S, P] = 0$  and that the spectrum of  $H_S$  is nondegenerate. The eigenstates  $|\alpha\rangle$  then have definite parity relative to the cylinder inversion center, which we can use to analyze the densities in Eq. (2.31). As before, we consider the density  $A_\alpha(\mathbf{r}) = \langle\alpha|A\delta(\mathbf{r}' - \mathbf{r})|\alpha\rangle$  and start by checking the parity transformation properties of the  $\delta$ -function. For an arbitrary ket  $|\psi\rangle$ , we have

$$\begin{aligned}\langle\psi|P^\dagger\delta(\mathbf{r}' - \mathbf{r})P|\psi\rangle &= \int \psi^\dagger(\phi', z')P^\dagger\delta(\mathbf{r}' - \mathbf{r})P\psi(\phi', z')r_0d\phi'dz' \\ &= \int \psi^\dagger(\phi' + \pi, L_0 - z')\delta(\mathbf{r}' - \mathbf{r})\psi(\phi' + \pi, L_0 - z')r_0d\phi'dz' \\ &= \psi^\dagger(\phi + \pi, L_0 - z)\psi(\phi + \pi, L_0 - z).\end{aligned}\tag{2.54}$$

Comparing the first and third lines shows that

$$P^\dagger\delta(\mathbf{r}' - \mathbf{r})P = \frac{1}{r_0}\delta(\phi' - [\phi + \pi])\delta(z' - [L_0 - z]) \equiv \delta(\mathbf{r}' - \mathbf{r}_P),\tag{2.55}$$

i. e.  $\mathbf{r} = (\phi, z)$  is mapped to the parity transformation  $\mathbf{r}_P \equiv (\phi + \pi, L_0 - z)$ . To analyze  $A_\alpha(\mathbf{r})$ , we use  $P|\alpha\rangle = \pm|\alpha\rangle$  and write

$$\begin{aligned}A_\alpha(\mathbf{r}) &= \langle\alpha|A\delta(\mathbf{r}' - \mathbf{r})|\alpha\rangle = \langle\alpha|P^\dagger A\delta(\mathbf{r}' - \mathbf{r})P|\alpha\rangle \\ &= \langle\alpha|P^\dagger APP^\dagger\delta(\mathbf{r}' - \mathbf{r})P|\alpha\rangle = \langle\alpha|P^\dagger AP\delta(\mathbf{r}' - \mathbf{r}_P)|\alpha\rangle.\end{aligned}\tag{2.56}$$

If  $A$  has definite parity  $P^\dagger AP = \pm A$ , it follows that

$$A_\alpha(\mathbf{r}) = \pm\langle\alpha|A\delta(\mathbf{r}' - \mathbf{r}_P)|\alpha\rangle = \pm A_\alpha(\mathbf{r}_P),\tag{2.57}$$

which relates the density at the coordinate  $\mathbf{r}$  to the density at the parity-transformed coordinate  $\mathbf{r}_P$ . This has immediate applications in considering the densities  $\rho(\mathbf{r})$  and  $\mathbf{S}(\mathbf{r})$  [Eq. (2.28)], as the identity operator and Pauli spin matrices all have even parity [Eq. (2.47)]. As with rotation, the transformation properties of  $\mathbf{j}(\mathbf{r})$  depend on which terms are included in  $H_S$ .



### 3. Results for the closed system

We consider a cylindrical shell with material parameters for InAs [15, 31]. Unless otherwise specified, we use the effective electron  $g$ -factor  $g_e = -14.9$ , a Rashba SOI parameter  $\alpha_R = 20$  meVnm, which corresponds to a strong confining radial field, and a Dresselhaus SOI parameter  $\beta_D = 3$  meVnm. As the effective mass of conduction electrons at the  $\Gamma$ -point, we use  $m_e = 0.023m_0$ . The temperature is taken as  $T = 1$  K, low enough to have no real role, but only to avoid possible errors from inserting  $T = 0$  K into the Fermi distribution function [Eq. (2.30)]. The dielectric constant is taken as  $\epsilon_r = 14.6$ . In the following sections, we discuss results obtained for a closed cylinder based on  $H_S$ , as discussed in Sec. 2.2.

Before proceeding, let us consider  $H_S$  in the case when all external fields vanish, i. e.  $\mathbf{E}_T = \mathbf{B} = 0$ . From Eq. (2.22) one obtains

$$H_S = \frac{p_\phi^2 + p_z^2}{2m_e} + \frac{\alpha_R}{\hbar} (\sigma_\phi p_z - \sigma_z p_\phi) + \frac{\beta_D}{\hbar} \left( \frac{1}{2} [\sigma_\phi p_\phi + p_\phi \sigma_\phi] - \sigma_z p_z \right). \quad (3.1)$$

Let us evaluate  $[D_z, H_S]$  [see Eq. (2.34)]. Taylor expanding  $D_z$  yields

$$D_z = \sum_{n=0}^{\infty} \frac{1}{n!} \left( -i \frac{J_z}{\hbar} \theta \right)^n, \quad (3.2)$$

so, since the commutator is linear, we must evaluate  $[J_z^n, H_S]$ . It is immediately clear that  $[J_z^n, p_z] = [J_z^n, \sigma_z] = [J_z^n, p_\phi] = 0$ , where the last one follows from  $p_\phi = L_z/r_0$ , and hence these operators all commute with  $D_z$ . All that remains is to check  $[J_z^n, \sigma_\phi]$ . Starting with  $n = 1$

$$[J_z, \sigma_\phi] = [L_z + \frac{\hbar}{2} \sigma_z, \sigma_\phi], \quad (3.3)$$

and since  $\sigma_\phi = \cos(\phi)\sigma_y - \sin(\phi)\sigma_x$ , one finds

$$[L_z, \cos(\phi)\sigma_y - \sin(\phi)\sigma_x] = -\frac{\hbar}{i} (\sin(\phi)\sigma_y + \cos(\phi)\sigma_x). \quad (3.4)$$

Using  $[\sigma_i, \sigma_j] = 2i\epsilon_{ijk}\sigma_k$  [20], one finds

$$\begin{aligned} \frac{\hbar}{2} [\sigma_z, \cos(\phi)\sigma_y - \sin(\phi)\sigma_x] &= \frac{\hbar}{i} (\sin(\phi)\sigma_y + \cos(\phi)\sigma_x) \\ &= -[L_z, \cos(\phi)\sigma_y - \sin(\phi)\sigma_x], \end{aligned} \quad (3.5)$$

### 3. Results for the closed system

and therefore

$$[J_z, \sigma_\phi] = 0. \quad (3.6)$$

Suppose  $[J_z^n, \sigma_\phi] = 0$  and let us show that  $[J_z^{n+1}, \sigma_\phi] = 0$ . One has

$$[J_z^{n+1}, \sigma_\phi] = J_z[J_z^n, \sigma_\phi] + [J_z, \sigma_\phi]J_z^n = 0, \quad (3.7)$$

and so  $[J_z^n, \sigma_\phi] = 0$  for all  $n$  by induction. Therefore,  $[D_z, \sigma_\phi] = 0$  and it follows that

$$[D_z, H_S] = 0, \quad (3.8)$$

i. e.  $H_S$  is rotationally invariant if  $\mathbf{E}_T = \mathbf{B} = 0$ .

## 3.1. Transverse magnetic field

Including a transverse magnetic field  $\mathbf{B} = B_x \hat{a}_x$ ,  $H_S$  becomes

$$\begin{aligned} H_S = & \frac{p_\phi^2 + p_z^2}{2m_e} + r_0 \omega_c^x \sin(\phi) p_z + \frac{\beta_D}{\hbar} \left[ \frac{1}{2} \{ \sigma_\phi p_\phi + p_\phi \sigma_\phi \} - \sigma_z \{ p_z + e r_0 B_x \sin(\phi) \} \right] \\ & + \frac{\hbar \omega_c^x}{2} \frac{r_0^2}{(l_B^x)^2} \sin^2(\phi) + \frac{\hbar g_e m^*}{4} \omega_c^x \sigma_x + \frac{\alpha_R}{\hbar} [ \sigma_\phi \{ p_z + e r_0 B_x \sin(\phi) \} - \sigma_z p_\phi ], \end{aligned} \quad (3.9)$$

and the rotational invariance is manifestly broken, for example since  $[J_z, \sigma_x] \neq 0$ . From Eq. (2.25),  $\mathbf{v}$  follows as

$$\mathbf{v} = \left( \frac{p_\phi}{m_e} - \frac{\alpha_R}{\hbar} \sigma_z + \frac{\beta_D}{\hbar} \sigma_\phi \right) \hat{a}_\phi + \left( \frac{p_z}{m_e} + r_0 \omega_c^x \sin(\phi) + \frac{\alpha_R}{\hbar} \sigma_\phi - \frac{\beta_D}{\hbar} \sigma_z \right) \hat{a}_z. \quad (3.10)$$

In Sec. 2.2 we analyzed the effects of a transverse magnetic field in part by considering an infinitely-long cylinder [Fig. 2.1]. To be consistent with this, we consider a cylinder of aspect ratio  $\eta = L_0/r_0 = 10$  with  $r_0 = 33.6$  nm in this section.

Figure 3.1 shows the equilibrium electron and current densities  $\rho(\mathbf{r})$  and  $\mathbf{j}(\mathbf{r})$  [Eq. (2.31)] of  $N_e = 10$  electrons on the cylinder in transverse magnetic fields of varying strength. The broken rotational symmetry manifests as an increase in  $\rho(\mathbf{r})$  around the angles  $\phi = \pi/2$  and  $\phi = 3\pi/2$ , where the radial projection  $B_x \cos(\phi)$  is minimum and snaking orbits are expected. Similarly,  $\rho(\mathbf{r})$  decreases around  $\phi = 0$  and  $\phi = \pi$ , where the radial magnetic field projection is maximum. This trend is amplified as  $B_x$  increases and for this particular configuration, the regions around  $\phi = 0$  and  $\phi = \pi$  are depleted of electrons if  $B_x = 4$  T, as Fig. 3.1 (e) shows. This behaviour is reflected in  $\mathbf{j}(\mathbf{r})$ , which shows how the snaking states carry currents between the cylinder edges and combine with edge currents there. For example, on the top



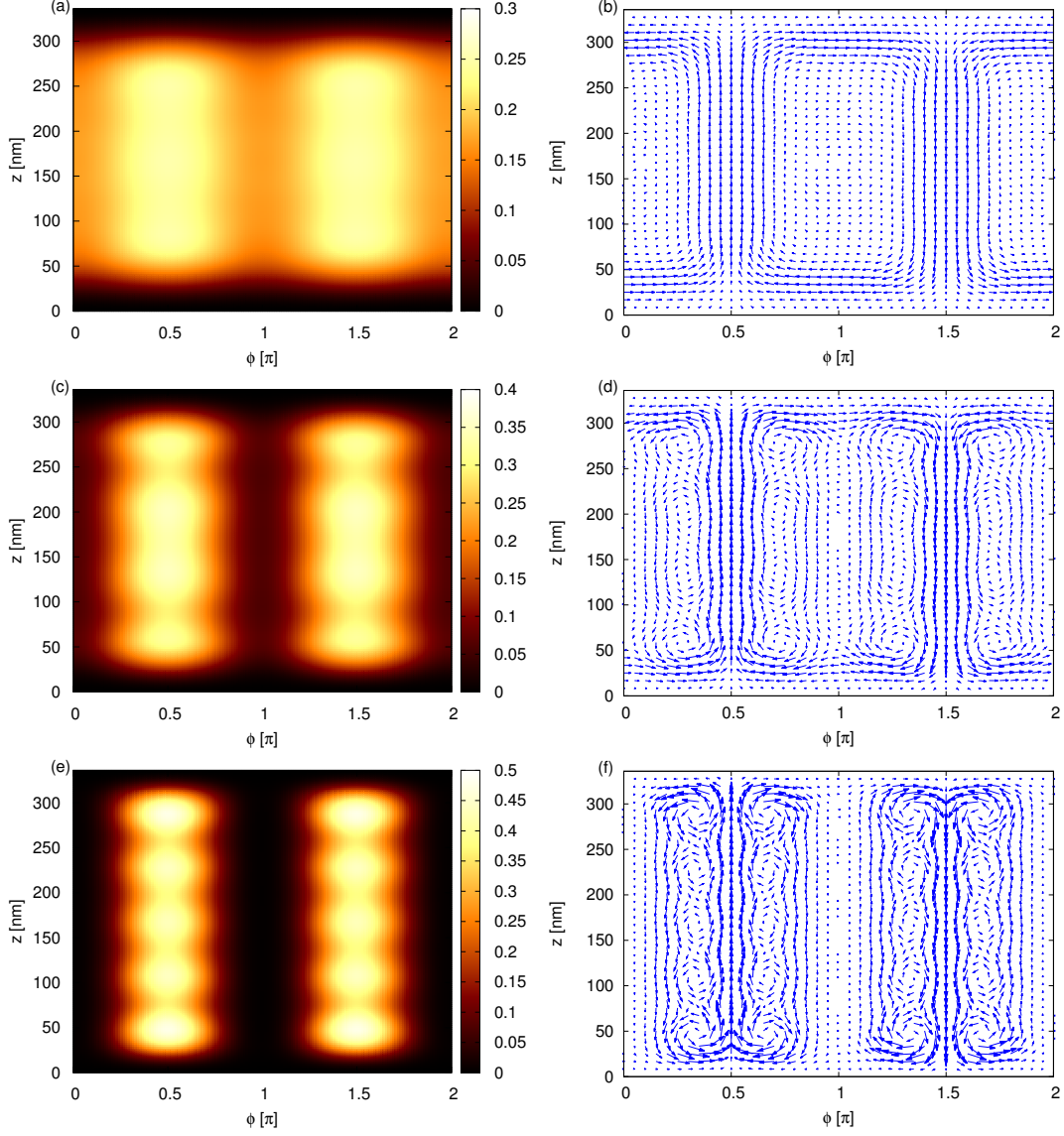


Figure 3.1: Electron (left) and current (right) densities of  $N_e = 10$  electrons in transverse magnetic fields of strength: (a), (b)  $B_x = 1$  T. (c), (d)  $B_x = 2$  T. (e), (f)  $B_x = 4$  T. As  $B_x$  increases, the densities increase around the angles  $\phi = \pi/2$  and  $\phi = 3\pi/2$  but decrease around  $\phi = 0$  and  $\phi = \pi$ . The electron density is given in units of  $10^{-4} \text{ nm}^{-2}$ .

### 3. Results for the closed system

edge of the cylinder in Figs. 3.1 (b) and (d), one observes how the snaking states split at  $\phi = \pi/2$  to form edge currents, which again recombine at  $\phi = 3\pi/2$  to form snaking states, resulting in closed current loops propagating on the cylinder surface. However, in the strong field  $B_x = 4$  T, where the regions around  $\phi = 0$  and  $\phi = \pi$  are depleted, the edge currents connecting the snaking states on opposite sides tend to vanish, and the two cylinder halves  $0 < \phi < \pi$  and  $\pi < \phi < 2\pi$  form disconnected current loops [Fig. 3.1 (f)]. Comparing Figs. 3.1 (b), (d) and (f) also shows the formation of vortices as  $B_x$  is increased, which we identify as cyclotron states. To explain the observed depletion at large values of  $B_x$ , recall that the depleted regions correspond to maxima in the radial projection  $B_x \cos(\phi)$ , and are thus the domain of cyclotron states. The localization of cyclotron states is governed by the magnetic length  $l_B^x = \sqrt{\hbar/(eB_x)}$ , such that when  $B_x$  increases, they become more localized around  $\phi = 0$  or  $\phi = \pi$ . This leads to the formation of Landau levels in these regions [14, 21], analogous to a two-dimensional planar electron gas in a perpendicular magnetic field [17]. The energies of Landau level states increase with  $B_x$ , whereas the energies of snaking states remain relatively stable [15]. For a fixed number of electrons  $N_e$ , it follows that at some value of  $B_x$ , the highest occupied state will have less energy than the lowest Landau level, resulting in a depletion of carriers around the angles  $\phi = 0$  and  $\phi = \pi$ . We have already seen that with  $N_e = 10$ ,  $B_x = 4$  T is already enough to deplete these regions. For more electrons however, a larger field would be necessary.

Let us now increase the number of electrons to  $N_e = 90$ , which is more realistic given the surface electron density reported in Ref. [31]. Figure 3.2 shows  $\rho(\mathbf{r})$  and  $\mathbf{S}(\mathbf{r})$  [Eq. (2.31)] in a transverse magnetic field  $B_x = 2$  T, for varying values of the SOI parameters  $(\alpha_R, \beta_D)$ . In (a),  $\rho(\mathbf{r})$  is shown as a function of  $\phi$  evaluated at  $z = 160$  nm, which is close to the cylinder center. As in Fig. 3.1, we observe dips and peaks in the cyclotron and snaking regions, respectively, although the structure is more complicated now due to the increased number of electrons. Interestingly, for the “most general” values  $(\alpha_R, \beta_D) = (20, 3)$  meVnm, we observe a faint asymmetry in  $\rho(\mathbf{r})$  under reflections over the  $x$ -axis, i. e. reflections over  $\phi = 0$  and  $\phi = \pi$ . Setting  $(\alpha_R, \beta_D) = (20, 0)$  meVnm restores the  $x$ -axis reflection symmetry, while setting  $(\alpha_R, \beta_D) = (0, 30)$  meVnm make the asymmetry more pronounced. Therefore, the asymmetry is due to the Dresselhaus term. If  $\beta_D = 0$ ,  $\rho(\mathbf{r})$  is invariant under reflections over the  $x$ -axis ( $\phi \rightarrow -\phi$ ), the  $y$ -axis ( $\phi \rightarrow \pi - \phi$ ) and hence also under inversion in the  $xy$ -plane ( $\phi \rightarrow \phi + \pi$ ). On the other hand, if  $\beta_D \neq 0$  only the  $xy$ -plane inversion survives. Unsurprisingly, this trend is not particular to  $z = 160$  nm and holds for arbitrary, fixed  $z$ . Figures 3.2 (b)-(d) show analogous plots for the spin densities  $S_x(\mathbf{r})$ ,  $S_y(\mathbf{r})$  and  $S_z(\mathbf{r})$ . The same symmetries are observed as with  $\rho(\mathbf{r})$ , but with some sign changes involved for  $S_y$  and  $S_z$ . Even the small value  $\beta_D = 3$  meVnm results in pronounced asymmetry in  $S_y$  and  $S_z$ , but  $S_x$  is more robust. This is due to the Zeeman term, which couples only to  $\sigma_x$  and acts as a spin-polarizing element in the relatively strong magnetic field  $B_x = 2$  T. Lastly, we probe longitudinal symmetries by showing  $\rho(\mathbf{r})$  plotted over a range of  $z$ -values,

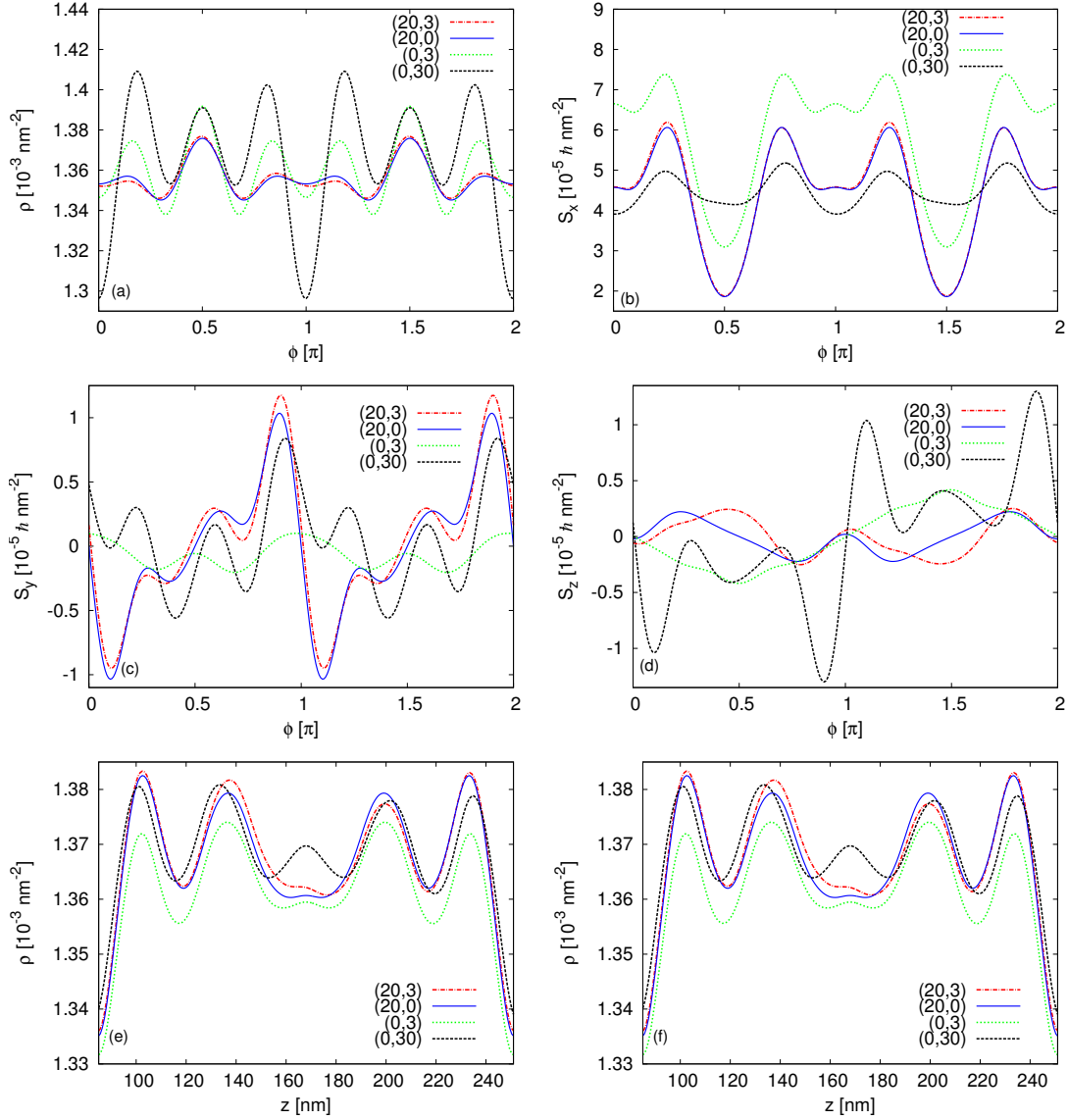


Figure 3.2: Charge and spin densities of  $N_e = 90$  electrons in a magnetic field  $B_x = 2$  T. Each curve corresponds to a combination of SOI parameters  $(\alpha_R, \beta_D)$  indicated in the key in units of  $\text{meVnm}$ . (a)-(d) Densities evaluated at  $z = 160$  nm as functions of  $\phi$ . (e), (f)  $\rho$  evaluated at  $\phi = 2\pi/5$  and  $\phi = 7\pi/5$ , respectively, plotted over a subinterval of the cylinder length, centered at  $z = L_0/2$ . (a)  $\rho$  is slightly asymmetric under reflections over  $\phi = 0$  and  $\phi = \pi$  when  $\beta_D \neq 0$ , but becomes symmetric if  $\beta_D = 0$ . The asymmetry becomes clear for the large value  $\beta_D = 30 \text{ meVnm}$ . (b), (c), (d) Analogous results for  $S_x$ ,  $S_y$  and  $S_z$ . Note that  $S_y$  and  $S_z$  may change sign under reflection over  $\phi = 0$  and  $\phi = \pi$ . In (e) and (f),  $\rho$  shows a longitudinal symmetry under reflections over  $z = L_0/2$  if  $\beta_D = 0$ .

### 3. Results for the closed system

centered at  $z = L_0/2$ , at the angles  $\phi = 2\pi/5$  and  $\phi = 7\pi/5$  in Figs. 3.2 (e) and (f), respectively. With  $\beta_D = 0$ ,  $\rho(\mathbf{r})$  is symmetric under longitudinal inversion relative to the cylinder center,  $z \rightarrow L_0 - z$  at any given angle, but when  $\beta_D \neq 0$  this symmetry is broken. If  $\beta_D \neq 0$ , we furthermore find that  $\rho(\mathbf{r})$  is symmetric under the transformations  $(z, \phi) \rightarrow (L_0 - z, -\phi)$  and  $(z, \phi) \rightarrow (L_0 - z, \pi - \phi)$ , although this is not explicitly shown in the figures. All of the aforementioned symmetries and their breaking also manifest in  $\mathbf{j}(\mathbf{r})$  and  $\mathbf{S}(\mathbf{r})$ , but possibly with a sign change as in Figs. 3.2 (b)-(d), although the symmetry breaking is not clearly visible in Fig. 3.1 due to the small value  $\beta_D = 3$  meVnm considered.

A summary of transformations under which densities are symmetric, depending on whether Dresselhaus SOI is included or not, is given in the following:

$$\begin{aligned} \beta_D = 0 : & \quad (z, \phi) \rightarrow (z, -\phi), \quad (z, \pi - \phi), \quad (z, \pi + \phi), \quad (L_0 - z, \phi), \\ \beta_D \neq 0 : & \quad (z, \phi) \rightarrow (z, \pi + \phi), \quad (L_0 - z, -\phi), \quad (L_0 - z, \pi - \phi). \end{aligned} \quad (3.11)$$

To illustrate these two cases, Fig. 3.3 shows how  $S_x(\mathbf{r})$  varies over a part of the cylinder surface, centered at  $z = L_0/2$ . We see that Dresselhaus SOI creates a “torsion” of the densities with opposite twist angles above and below the cylinder center. Interestingly enough, this torsion effect has no analogue in infinitely-long cylinders and is thus related to the finite system length [15]. More specifically, we have traced it to the terms  $\sigma_\phi p_\phi + p_\phi \sigma_\phi$  in Dresselhaus SOI, i. e. setting them to zero removes the torsion. From Fig. 3.1, it is clear that edge currents give the primary contribution to this SOI term due to the large angular currents at the edges, and so the torsion arises due to an interplay between edge currents and Dresselhaus SOI. Since edge currents only manifest in cylinders of finite length, the torsion does not appear in infinitely-long cylinders.

We can shed light on a part of the observed symmetries [Eq. (3.11)] by considering the parity transformation properties of  $H_S$  [Eq. (3.9)]. Using Eqs. (2.47), (2.48) and (2.53) yields

$$\begin{aligned} P \sin(\phi) P &= -\sin(\phi), \quad P \cos(\phi) P = -\cos(\phi), \quad P p_\phi P = P \frac{L_z}{r_0} P = \frac{L_z}{r_0} = p_\phi, \\ P \sigma_\phi P &= P(\cos(\phi)\sigma_y - \sin(\phi)\sigma_x)P = P \cos(\phi) P P \sigma_y P - P \sin(\phi) P P \sigma_x P \\ &= -\cos(\phi)\sigma_y + \sin(\phi)\sigma_x = -\sigma_\phi. \end{aligned} \quad (3.12)$$

It follows that every term in  $H_S$  has even parity except for the Dresselhaus term, which has odd parity. Provided  $\beta_D = 0$ , one therefore has  $[H_S, P] = 0$  and since the spectrum is generally nondegenerate, eigenstates have definite parity relative to the cylinder center as discussed in Sec. 2.4. As a result,  $\rho(\mathbf{r})$  and  $\mathbf{S}(\mathbf{r})$ , both of which depend on the expectation value of operators with even parity [Eq. (2.28)], are even under the parity transformation  $(z, \phi) \rightarrow (L_0 - z, \pi + \phi)$ . With  $\beta_D \neq 0$  however,  $H_S$  and  $P$  no longer commute and the parity symmetry is lost, as Eq. (3.11) indeed expresses. Similarly,  $\mathbf{j}(\mathbf{r})$  depends on the expectation value of  $\mathbf{v}$  [Eq. (3.10)], the

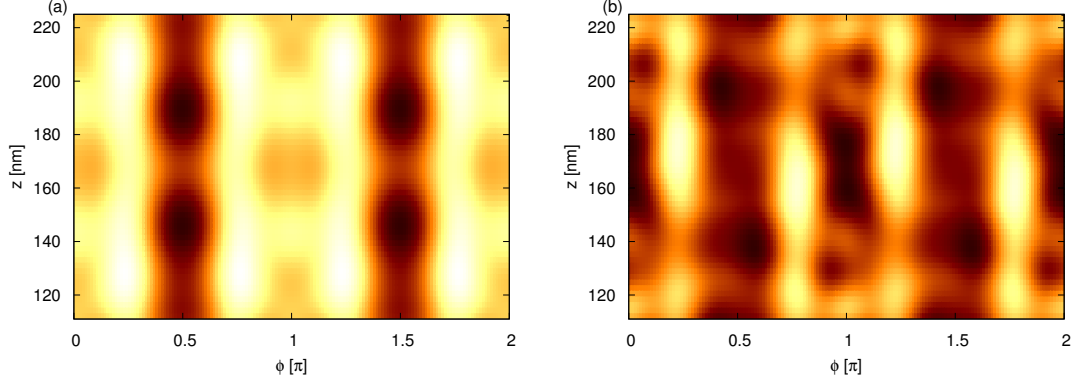


Figure 3.3: Spin density  $S_x(\mathbf{r})$  of  $N_e = 90$  electrons plotted over a part of the cylinder surface centered at  $z = L_0/2$  in a transverse magnetic field  $B_x = 2$  T with (a)  $(\alpha_R, \beta_D) = (20, 0)$  meVnm and (b)  $(\alpha_R, \beta_D) = (0, 30)$  meVnm, demonstrating the symmetry properties given in Eq. (3.11). A nonzero  $\beta_D$  creates a torsion of the spin density with opposite twist angles above and below the cylinder center. Bright and dark colors correspond to regions of high and low density, respectively.

components of which have definite parity if  $\beta_D = 0$ , such that  $j_z$  and  $j_\phi$  are odd and even under parity, respectively [15].

## 3.2. Longitudinal magnetic field

In a purely longitudinal magnetic field with  $\alpha_R = \beta_D = g_e = 0$ , the Hamiltonian and spectrum are given in Eqs. (2.12) and (2.13), respectively. As discussed in Sec. 2.2, the spectrum is periodic in the magnetic flux  $\Phi$  with period  $\Phi_0$ . Figure 3.4 shows how the spectra of cylinders with radius  $r_0 = 16.8$  nm and different aspect ratios  $\eta = L_0/r_0$  vary with  $\Phi$ . When  $\eta \ll 1$  as in (a), the energy gap between axial levels of quantization ( $\propto 1/L_0^2$ ) is much larger than between angular levels ( $\propto 1/r_0^2$ ). Therefore, the energetically-lowest states correspond to different angular levels occupying the lowest axial level, forming a ring-like spectrum. The reason for the large energy scale in (a) is that the energy of the lowest axial level is  $\propto 1/L_0^2$  and thus becomes large for small  $L_0$ . For  $\eta \approx 1$ , the energies of axial and angular levels become comparable, such that higher axial levels become occupied at lower energies, as shown in (b) for the case  $\eta = 3$ . There, the second and third axial levels set in around the energies 25 and 60 meV, respectively, complicating the spectrum somewhat. Regardless, a comparison with (a) shows that the spectrum in (b) can be thought of as a superposition of several ring-like spectra, each corresponding to a single axial level. In (c), we have  $\eta = 10$  and the spacing between angular levels is now greater than between axial levels. As a result, the energetically lowest states correspond to successively higher axial levels occupying the lowest angular level.

### 3. Results for the closed system

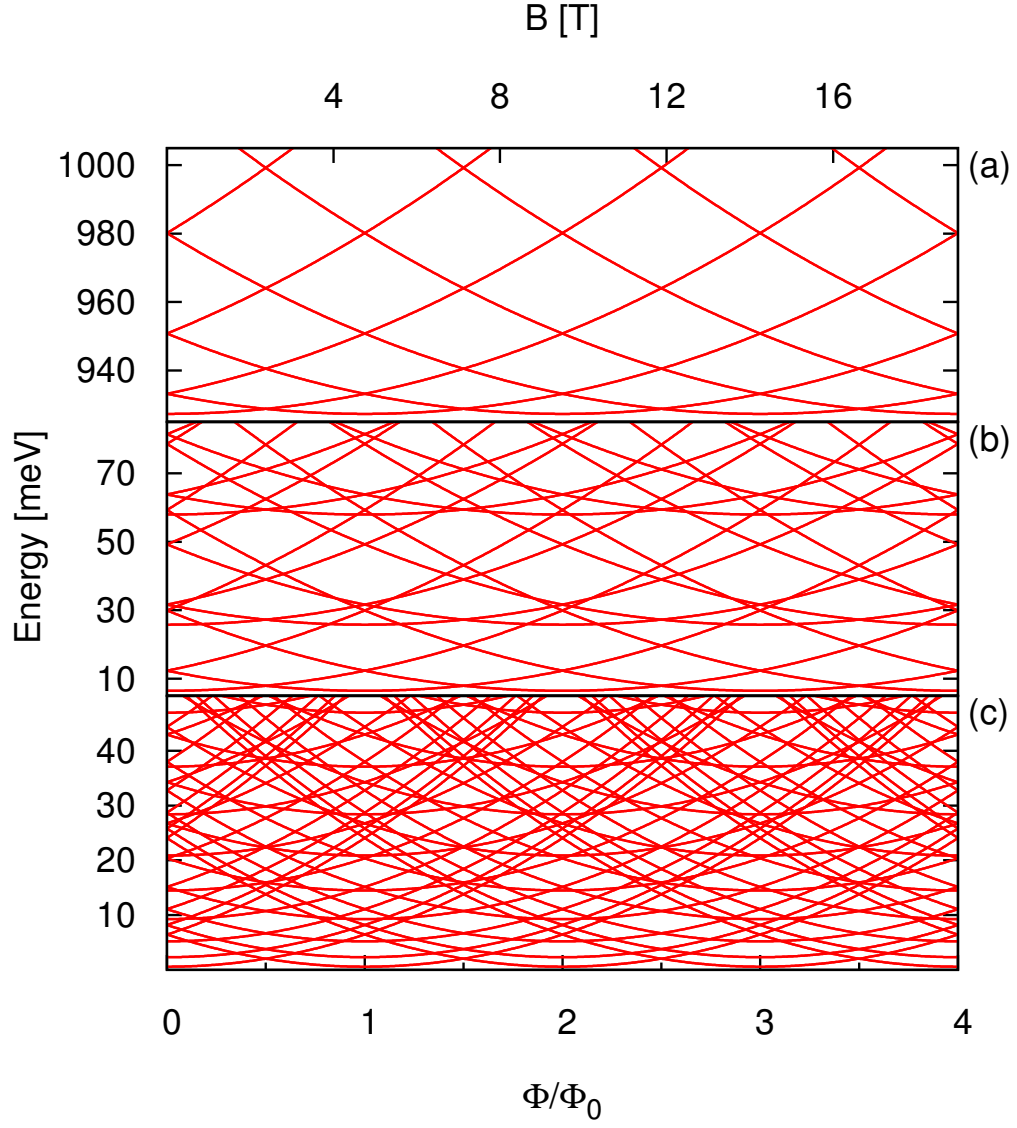


Figure 3.4: Flux-dependence of the spectrum of a cylinder with spin suppressed,  $r_0 = 16.8$  nm and aspect ratio: (a)  $\eta = 0.25$ . (b)  $\eta = 3$ . (c)  $\eta = 10$ . In all cases, the spectrum is periodic in  $\Phi$ .

To probe spin effects on the spectrum, we maintain  $r_0 = 16.8$  nm and fix  $\eta = 3$  such that angular and axial levels enter into the spectrum on equal footing [Fig. 3.4 (b)]. Section 3.1 showed that for the chosen parameters, the Rashba term is the dominant SOI, such that including both Rashba and Dresselhaus SOI only results in minor variations when compared with the case of only Rashba SOI. While the Dresselhaus term is most certainly interesting as a symmetry-breaking element, as discussed in Sec. 3.1, we will mostly focus on Rashba SOI in the following. In Fig. 3.5, we show the effects of the Rashba and Zeeman terms on the closed cylinder spectrum. With both terms included, the Hamiltonian is given by [Eqs. (2.12), (2.16) and (2.19)]

$$H_S = \frac{\hbar^2}{2m_e} \left[ \frac{1}{r_0^2} \left( \frac{\partial_\phi}{i} + \frac{\Phi}{\Phi_0} \right)^2 + \left( \frac{\partial_z}{i} \right)^2 \right] + \frac{\hbar g_e m^*}{4} \omega_c^z \sigma_z + \frac{\alpha_R}{\hbar} \left[ \sigma_\phi p_z - \sigma_z \left( p_\phi + \frac{e B_z r_0}{2} \right) \right]. \quad (3.13)$$

In (a), the spectrum is shown with the Zeeman term included. In this case, the spectrum can be written analytically as

$$\begin{aligned} \epsilon_{nps}^S &= \frac{\hbar^2}{2m_e r_0^2} \left[ \left( n + \frac{\Phi}{\Phi_0} \right)^2 + p^2 \frac{r_0^2}{L^2} \right] + \frac{\hbar g_e m^*}{4} \omega_c^z s \\ &= \frac{\hbar^2}{2m_e r_0^2} \left[ \left( n + \frac{\Phi}{\Phi_0} \right)^2 + p^2 \frac{r_0^2}{L^2} + g_e m^* \frac{\Phi}{\Phi_0} s \right]. \end{aligned} \quad (3.14)$$

The Zeeman term thus introduces a flux-linear term which splits the energies of spin up and down states and breaks the periodicity of the spectrum [27, 28]. This effect is pronounced in InAs due to the large electron  $g$ -factor. In (b), the spectrum is shown with only Rashba SOI included, i. e.  $g_e = 0$ . Compared with Fig. 3.4 (b), Rashba SOI generally lifts the spin degeneracy at  $\Phi \neq 0$ , but crossings still appear at regular intervals. Interestingly, the spectrum remains periodic in  $\Phi$  despite Rashba SOI introducing a flux-linear term into the Hamiltonian [27]. Unfortunately, the spectrum can not be written analytically, but this result can nonetheless be understood by noting that  $\Phi$  couples only to the angular part of the Hamiltonian [Eq. (3.13)]. As a result, the flux-dependence does not change in the quantum ring-limit  $L_0 \rightarrow 0$ , in which longitudinal electron motion is suppressed, and we set  $p_z = 0$ . In this ring limit, the spectrum is given by

$$\epsilon_{ns}^{Sr} = \frac{\hbar^2}{2m_e r_0^2} \left( n + \frac{\Phi}{\Phi_0} \right)^2 - \frac{\alpha_R}{r_0} \left( n + \frac{\Phi}{\Phi_0} \right) s, \quad (3.15)$$

which is indeed periodic in  $\Phi$ . Since the ring-limit and the finite-cylinder spectra couple identically to  $\Phi$ , it follows that the spectrum of a finite cylinder with Rashba SOI alone is also periodic in  $\Phi$ , which is in agreement with the numerically obtained spectrum (b). We emphasize that the ring-limit spectrum with Rashba SOI [Eq.

### 3. Results for the closed system

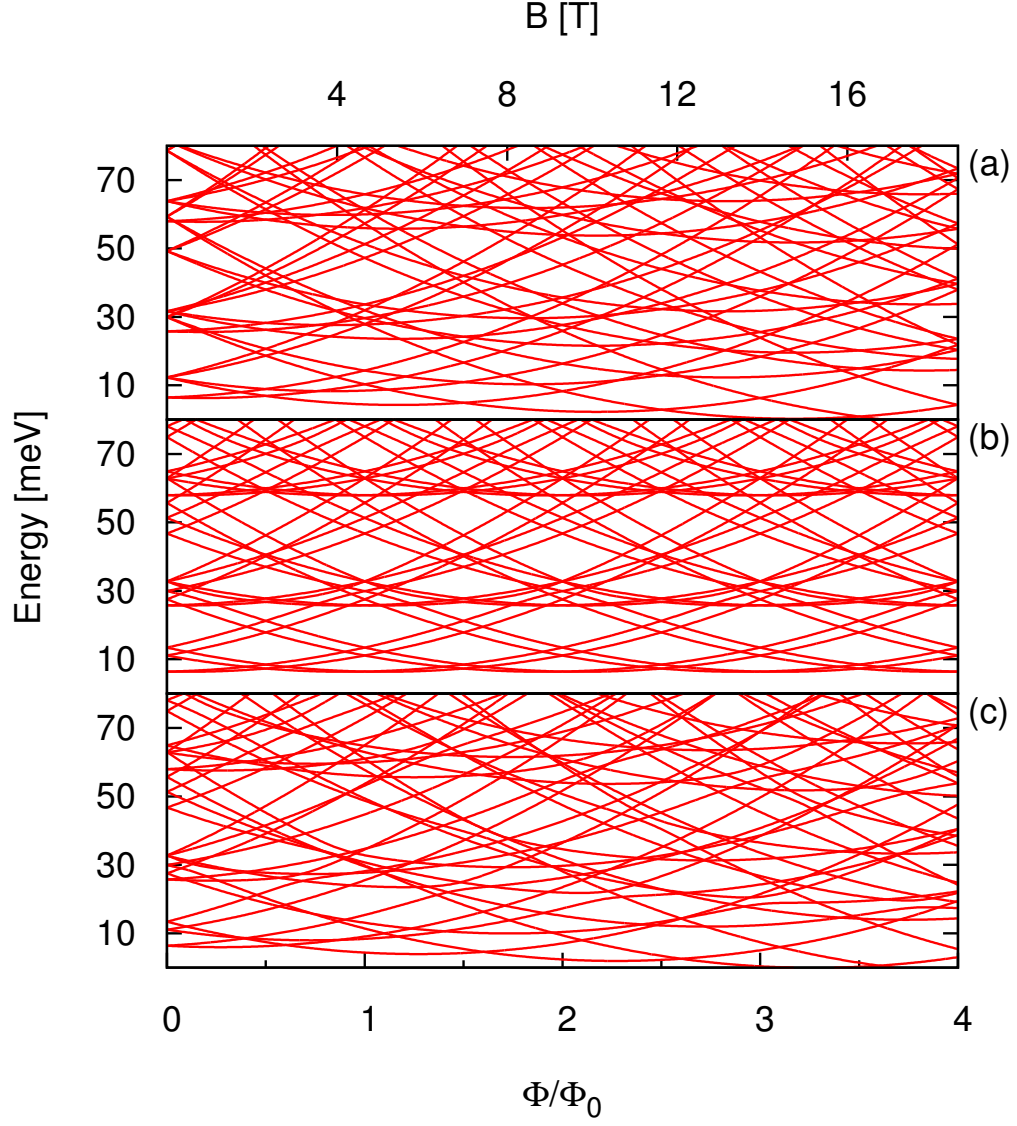


Figure 3.5: Flux-dependence of the spectrum of a cylinder with  $r_0 = 16.8$  nm and aspect ratio  $\eta = 3$  with: (a)  $g_e = -14.9$ ,  $\alpha_R = 0$ . (b)  $g_e = 0$ ,  $\alpha_R = 20$  meVnm. (c)  $g_e = -14.9$ ,  $\alpha_R = 20$  meVnm. The Zeeman term breaks the flux-periodicity whereas the Rashba term does not.



(3.15)] differs from known results for quantum rings. The reason is that in cylindrical core-shell geometries the confining electric field is radial [27, 31], whereas in quantum rings it is typically assumed to be perpendicular to the ring, i. e. along the  $z$  direction [37, 39–42]. Lastly, (c) shows the spectrum with both Rashba and Zeeman terms included. Due to the Zeeman term, the periodicity of the spectrum is again broken.

In contrast to a transverse magnetic field, a longitudinal one should intuitively not break the circular symmetry of the system. This turns out to be true, as the Hamiltonian [Eq. (3.13)] commutes with the rotation operator [Eq. (2.34)], which can be shown following the procedure outlined in the beginning of this section. Hence the system is rotationally invariant and, since the spectrum is generally nondegenerate at arbitrary values of  $\Phi$ , densities based on rotationally invariant observables are circularly symmetric, as discussed in Sec. 2.4. This includes  $\rho(\mathbf{r})$  and  $S_z(\mathbf{r})$ , but not  $S_x(\mathbf{r})$  and  $S_y(\mathbf{r})$  since the operators  $\sigma_x$  and  $\sigma_y$  do not commute with  $D_z$ . The velocity operator derived from  $H_s$  [Eq. (3.13)] is given by

$$\mathbf{v} = \left[ \frac{p_\phi}{m_e} + \frac{r_0 \omega_c^z}{2} - \frac{\alpha_R}{\hbar} \sigma_z \right] \hat{a}_\phi + \left[ \frac{p_z}{m_e} + \frac{\alpha_R}{\hbar} \sigma_\phi \right] \hat{a}_z, \quad (3.16)$$

and is indeed rotationally invariant. As a result,  $\mathbf{j}(\mathbf{r})$  is also rotationally invariant. To illustrate these properties,  $\mathbf{j}(\mathbf{r})$  and  $\mathbf{S}(\mathbf{r})$  of  $N_e = 8$  electrons on the cylinder surface are shown in Fig. 3.6. Indeed, the rotationally invariant  $S_z(\mathbf{r})$  and  $\mathbf{j}(\mathbf{r})$  manifest as concentric circles of constant density, while  $S_x(\mathbf{r})$  and  $S_y(\mathbf{r})$  have an angular dependence. Particularly interesting is the fact that  $j_z$  vanishes everywhere in Fig. 3.6 (a), despite the fact that Rashba SOI introduces spin-dependent terms into both  $v_z$  and  $v_\phi$ , as Eq. (3.16) shows. In fact, when  $\alpha_R = 0$  the resulting current density is almost indistinguishable from that in Fig. 3.6 (a): in particular,  $j_z$  also vanishes in this case, which from  $v_z$  suggests that the densities of the observables  $p_z$  and  $\sigma_\phi$  vanish everywhere. Numerically, we find that this is indeed the case. However, this is contrary to what happens on an infinitely long cylinder, where Rashba SOI alone has been shown to produce a nonvanishing tangential spin density  $S_\phi(\mathbf{r}) = \cos(\phi)S_y(\mathbf{r}) - \sin(\phi)S_x(\mathbf{r})$  [31]. In order to understand the difference, we again consider an infinitely long cylinder in a longitudinal magnetic field with Rashba SOI alone, i. e. described by the Hamiltonian in Eq. (3.13) with  $g_e = 0$  and no hard-wall boundary conditions at  $z = 0$  and  $z = L_0$ . Note that inclusion of the Zeeman term is not essential when considering  $\mathbf{j}$ , as it does not enter into  $\mathbf{v}$  [Eq. (3.16)]. The Hamiltonian commutes with both  $p_z$  and  $J_z$  so we look for spinor solutions of the form [30, 31]

$$\psi_{nk}(z, \phi) = \frac{1}{2\pi\sqrt{r_0}} e^{ikz} e^{in\phi} \begin{pmatrix} a \\ b e^{i\phi} \end{pmatrix}, \quad (3.17)$$

where  $n \in \mathbb{Z}$  and  $k \in \mathbb{R}$ . The time-independent Schrödinger equation  $H_S \psi_{nk} = E \psi_{nk}$  yields

$$\begin{bmatrix} \gamma(n + \tilde{\Phi})^2 - \tilde{E} - \frac{\alpha_R}{r_0} \left( n + \tilde{\Phi} \right) & -i\alpha_R k \\ i\alpha_R k & \gamma(n + 1 + \tilde{\Phi})^2 - \tilde{E} + \frac{\alpha_R}{r_0} \left( n + 1 + \tilde{\Phi} \right) \end{bmatrix} \begin{pmatrix} a \\ b \end{pmatrix} = 0, \quad (3.18)$$

### 3. Results for the closed system

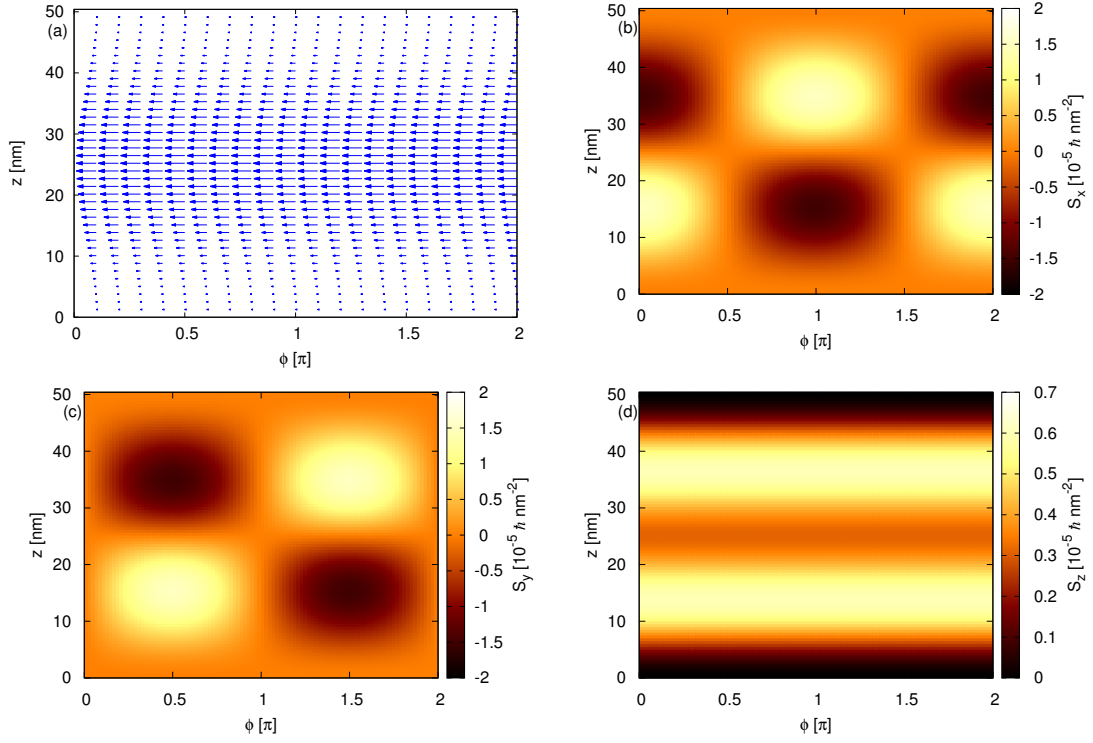


Figure 3.6: Current and spin densities of  $N_e = 8$  electrons on a cylinder with  $r_0 = 16.8$  nm and  $L_0 = 50.4$  nm ( $\eta = 3$ ) in a magnetic field  $B_z = 2$  T ( $\Phi/\Phi_0 \approx 0.4$ ) with Rashba SOI and Zeeman interaction. Both  $\mathbf{j}(\mathbf{r})$  and  $S_z(\mathbf{r})$  are circularly symmetric since  $\mathbf{v}$  and  $\sigma_z$  are rotationally invariant. However,  $S_x(\mathbf{r})$  and  $S_y(\mathbf{r})$  lack this property because  $\sigma_x$  and  $\sigma_y$  do not commute with the rotation operator  $D_z$ .

where we have for simplicity defined  $\gamma = \hbar^2/2m_e r_0^2$ ,  $\tilde{\Phi} = \Phi/\Phi_0$  and  $\tilde{E} = E - \gamma k^2 r_0^2$ . The energies are

$$E_n^\pm(k) = \gamma k^2 r_0^2 + \frac{1}{2} \left( A \pm \sqrt{A^2 - 4(B - \alpha_R^2 k^2)} \right). \quad (3.19)$$

The coefficients  $A(n, \tilde{\Phi})$  and  $B(n, \tilde{\Phi})$  are functions of  $n$  and  $\tilde{\Phi}$ , but independent of  $k$ . Their exact form is not important for our analysis, but it follows that  $E_n^\pm(k) = E_n^\pm(-k)$ . To ensure normalization, the spinor coefficients  $a$  and  $b$  can be chosen as

$$a_n^\pm(k) = \frac{i\alpha_R k}{\gamma(n + \tilde{\Phi})^2 - \frac{\alpha_R}{r_0}(n + \tilde{\Phi}) - \tilde{E}_n^\pm(k)} b_n^\pm(k) \quad (3.20)$$

and

$$b_n^\pm(k) = \sqrt{\left( 1 + \frac{\alpha_R^2 k^2}{\left[ \gamma(n + \tilde{\Phi})^2 - \frac{\alpha_R}{r_0}(n + \tilde{\Phi}) - \tilde{E}_n^\pm(k) \right]^2} \right)^{-1}}, \quad (3.21)$$

which clearly satisfy  $b_n^\pm(-k) = b_n^\pm(k)$ ,  $(b_n^\pm(k))^* = b_n^\pm(k)$ ,  $a_n^\pm(-k) = -a_n^\pm(k)$  and  $(a_n^\pm(k))^* = -a_n^\pm(k)$ . From this, it indeed follows that  $\langle \psi_n^\pm(k) | \sigma_\phi \delta(\mathbf{r} - \mathbf{r}') | \psi_n^\pm(k) \rangle \neq 0$ , i. e. Rashba SOI results in a nonzero tangential spin density in agreement with Ref. [31]. There is however a fundamental difference between eigenstates on the finite and infinite cylinders, namely that  $\langle p_z \rangle$  always vanishes on the former, but not on the latter except if  $k = 0$ . On the finite cylinder with  $\alpha_R \neq 0$ ,  $\langle p_z \rangle = 0$  because the spectrum of  $H_S$  is nondegenerate at arbitrary values of  $\Phi$  and  $[H_S, P] = 0$ , such that the eigenstates  $|\alpha\rangle$  have definite parity relative to the cylinder center, as discussed in Sec. 2.4. But since  $p_z = -i\hbar\partial_z$  can only couple states of opposite parity, it follows that  $\langle \alpha | p_z | \alpha \rangle = 0$  always. This difference alone implies nonzero  $j_z$  on the infinite cylinder, and thus invalidates a direct comparison between the infinite- and finite-length systems. But since  $E_n^\pm(k) = E_n^\pm(-k)$ , one can easily construct infinite-cylinder eigenstates that satisfy  $\langle p_z \rangle = 0$  and are thus physically the “closest” ones to finite-cylinder eigenstates. The most general form satisfying  $\langle p_z \rangle = 0$  is

$$\chi_n^\pm(k) = \frac{1}{\sqrt{2}} (\psi_n^\pm(k) + e^{i\theta} \psi_n^\pm(-k)), \quad (3.22)$$

where  $\theta \in \mathbb{R}$ . Analogous to the finite cylinder, one then obtains vanishing tangential spin density  $\langle \chi_n^\pm(k) | \sigma_\phi \delta(\mathbf{r} - \mathbf{r}') | \chi_n^\pm(k) \rangle = 0$ , which reconciles the two cases.

To conclude this section, let us briefly consider the effects of including the Dresselhaus term in a longitudinal magnetic field, such that

$$\begin{aligned} H_S = & \frac{\hbar^2}{2m_e} \left[ \frac{1}{r_0^2} \left( \frac{\partial_\phi}{i} + \frac{\Phi}{\Phi_0} \right)^2 + \left( \frac{\partial_z}{i} \right)^2 \right] + \frac{\alpha_R}{\hbar} \left[ \sigma_\phi p_z - \sigma_z \left( p_\phi + \frac{eB_z r_0}{2} \right) \right] \\ & + \frac{\hbar g_e m^*}{4} \omega_c^z \sigma_z + \frac{\beta_D}{\hbar} \left( \frac{1}{2} \left[ \sigma_\phi \left\{ p_\phi + \frac{eB_z r_0}{2} \right\} + \left\{ p_\phi + \frac{eB_z r_0}{2} \right\} \sigma_\phi \right] - \sigma_z p_z \right). \end{aligned} \quad (3.23)$$

### 3. Results for the closed system

As was shown in the beginning of this section,  $[\sigma_\phi, D_z] = 0$ , from which it immediately follows that  $[H_S, D_z] = 0$ . Hence, even in the presence of both Rashba and Dresselhaus SOI, the system maintains the rotational symmetry in a longitudinal magnetic field. This is an interesting result, because it can be shown that interplay between the two SOI terms breaks the rotational symmetry of quantum rings pierced by a longitudinal magnetic flux, resulting e. g. in charge densities with angular dependence [37, 40, 41]. As was the case in a transverse magnetic field, the Dresselhaus term breaks the parity symmetry of the system, because  $P$  anticommutes with  $\sigma_\phi$  [see Eq. (3.12)]. The invariance of the various densities under the transformation  $(z, \phi) \rightarrow (L_0 - z, \phi + \pi)$ , visible in Fig. 3.6, is thus broken when the Dresselhaus term is included. However, using the small value  $\beta_D = 3$  meVnm characteristic for InAs, this effect is weak, as we saw with the transverse magnetic field in Sec. 3.1.

## 4. Modelling transport through the finite system

In Chapter 2 we discussed the equilibrium properties of a closed, cylindrical core-shell nanowire. A common means for examining the physical properties of a nanosystem is transport measurements, which probe how well the system carries current. In order to drive a current through the system, it must be brought out of equilibrium and supplied with carriers from an external source. Accordingly, the system is no longer closed, but open to the environment.

In order to simulate the transport of carriers through the finite system, we connect it to two leads at the edges  $z = 0$  and  $z = L_0$ , forming junctions. The leads are taken as semi-infinite, cylindrical continuations of the finite, central system (S) of the same radius  $r_0$ , extending from the junctions to the left (L) over  $z < 0$  and to the right (R) over  $L_0 < z$ , respectively. Their purpose is to supply electrons to the now open central system from two hypothetical reservoirs (or contacts). The reservoirs are maintained at the chemical potentials  $\mu_L$  and  $\mu_R$ , which can generally differ, for example if an external bias is applied to the system. Assuming that states in the left (right) lead are occupied only by electrons from the left (right) reservoir, it follows that the chemical potential of the left (right) lead is  $\mu_L$  ( $\mu_R$ ). Provided the system is out of equilibrium with  $\mu_L \neq \mu_R$ , carriers will flow between the leads through the central system, where they may be scattered by the many effects discussed in Sec. 2.2. We are primarily interested in examining transport through the central system and how scattering due to the various terms in  $H_S$  [Eq. (2.22)] affects transport properties, while the leads are simply introduced as tools for bringing the system out of equilibrium and supplying it with carriers. Hence, we apply a method based on Green's functions which allows us to extract the conductance of the finite central system coupled to leads [43]. Before proceeding with a description of the method, let us discuss Green's functions briefly.

## 4.1. Green's functions

Consider a linear partial differential equation

$$D(\mathbf{r}, t)\psi(\mathbf{r}, t) = J(\mathbf{r}, t), \quad (4.1)$$

where  $D(\mathbf{r}, t)$  is a partial differential operator in the coordinates  $\mathbf{r}$  and  $t$  of arbitrary degree and  $J$  is a source term. An extremely useful tool for solving problems of this sort is Green's functions. A Green's function  $G(\mathbf{r}, t, \mathbf{r}', t')$  for the operator  $D(\mathbf{r}, t)$  satisfies the equation

$$D(\mathbf{r}, t)G(\mathbf{r}, t, \mathbf{r}', t') = \delta(\mathbf{r} - \mathbf{r}')\delta(t - t'). \quad (4.2)$$

Physically,  $G$  thus describes an excitation due to a point source in space-time. If  $G$  is known, a solution to Eq. (4.1) follows

$$\psi(\mathbf{r}, t) = \int G(\mathbf{r}, t, \mathbf{r}', t')J(\mathbf{r}', t')d\mathbf{r}'dt', \quad (4.3)$$

as is readily verified by

$$\begin{aligned} D(\mathbf{r}, t)\psi(\mathbf{r}, t) &= D(\mathbf{r}, t) \int G(\mathbf{r}, t, \mathbf{r}', t')J(\mathbf{r}', t')d\mathbf{r}'dt' \\ &= \int \delta(\mathbf{r} - \mathbf{r}')\delta(t - t')J(\mathbf{r}', t')d\mathbf{r}'dt' = J(\mathbf{r}, t), \end{aligned} \quad (4.4)$$

assuming that  $D$  can be moved under the integration [43, 44]. Provided a solution to the homogeneous version of Eq. (4.1) is known, the general solution to Eq. (4.1) can be written as

$$\psi(\mathbf{r}, t) = \psi_0(\mathbf{r}, t) + \int G(\mathbf{r}, t, \mathbf{r}', t')J(\mathbf{r}', t')d\mathbf{r}'dt', \quad (4.5)$$

where  $D(\mathbf{r}, t)\psi_0(\mathbf{r}, t) = 0$ .

For a Schrödinger equation with Hamiltonian  $H_S$ , a Green's function satisfies

$$\left(i\hbar\frac{\partial}{\partial t} - H_S\right)G(\mathbf{r}, t, \mathbf{r}', t') = \delta(\mathbf{r} - \mathbf{r}')\delta(t - t'). \quad (4.6)$$

As in Sec. 2.2, let us assume that  $H_S$  is time-independent. Then, the Schrödinger equation is separable in time and space and the time-evolution of state kets is governed by the time-evolution operator

$$U(t, t_0) = \exp\left(-i\frac{H_S}{\hbar}(t - t_0)\right). \quad (4.7)$$

Therefore, the propagation of solutions to the Schrödinger equation between two time points depends only on the time difference. In particular, this holds for Green's functions, which are solutions provided  $\mathbf{r} \neq \mathbf{r}'$  and  $t \neq t'$ . Hence, we set  $G(\mathbf{r}, t, \mathbf{r}', t') = G(\mathbf{r}, \mathbf{r}', t - t') \equiv G(\mathbf{r}, \mathbf{r}', t)$ , which satisfies

$$\left(i\hbar\frac{\partial}{\partial t} - H_S\right) G(\mathbf{r}, \mathbf{r}', t) = \delta(\mathbf{r} - \mathbf{r}')\delta(t) \quad (4.8)$$

for the time difference  $t$ . Of particular interest in physics is the Green's function that describes the “response” to the source term  $\delta(\mathbf{r} - \mathbf{r}')\delta(t)$ , i. e. the solution to Eq. (4.8) that exists only for  $t > 0$ , and hence propagates forward in time. This solution is called the retarded Green's function, which will from now on be referred to simply as the Green's function [44]. In order to proceed, let us Fourier transform Eq. (4.8) in time. Integration by parts yields

$$\int_0^\infty e^{it(\omega+i\eta)} \frac{\partial}{\partial t} G(\mathbf{r}, \mathbf{r}', t) dt = -i(\omega+i\eta) \int_0^\infty e^{-\eta t} e^{i\omega t} G(\mathbf{r}, \mathbf{r}', t) dt = -i(\omega+i\eta) G(\mathbf{r}, \mathbf{r}', \omega), \quad (4.9)$$

where we have set the frequency  $\omega \rightarrow \omega + i\eta$  with  $\eta \rightarrow 0^+$  to ensure that the integral converges in the limit  $t \rightarrow \infty$ . Hence, Eq. (4.8) yields

$$(\hbar\omega + i\eta - H_S) G(\mathbf{r}, \mathbf{r}', \omega) = \delta(\mathbf{r} - \mathbf{r}'), \quad (4.10)$$

where we redefine  $\hbar\eta \equiv \eta$ , keeping the sign intact. By analogy with the time-independent Schrödinger equation  $(H_S - \epsilon_\alpha^S)|\alpha\rangle = 0$ , we identify  $\hbar\omega \equiv E$  as the energy of the particle and obtain

$$(E - H_S + i\eta) G(\mathbf{r}, \mathbf{r}', E) = \delta(\mathbf{r} - \mathbf{r}'), \quad (4.11)$$

or equivalently, in the inverse operator sense

$$G(\mathbf{r}, \mathbf{r}', E) = \frac{\delta(\mathbf{r} - \mathbf{r}')}{E - H_S + i\eta}. \quad (4.12)$$

Noting that  $\langle \mathbf{r} | \mathbf{r}' \rangle = \delta(\mathbf{r} - \mathbf{r}')$  we define the retarded Green's operator  $G$

$$G(E) = \frac{1}{E - H_S + i\eta}, \quad (4.13)$$

the matrix element of which in coordinate representation yields the Green's function

$$\langle \mathbf{r} | G(E) | \mathbf{r}' \rangle = \frac{\delta(\mathbf{r} - \mathbf{r}')}{E - H_S + i\eta} = G(\mathbf{r}, \mathbf{r}', E). \quad (4.14)$$

Equation (4.13) is the fundamental result of this section and is an essential component in the transport formalism, which will be discussed next.

## 4.2. Obtaining conductance with Green's functions

Consider a system composed of the finite cylinder discussed in Sec. 2.2 and the two leads discussed in the introduction to this chapter. If the two leads are uncoupled both to each other and to the central system, the entire system is described by three uncoupled Schrödinger equations. In the case of electron transport, when electrons pass between the leads through the central system, interactions between the systems take place at the junctions and the three parts are indeed coupled, which must be accounted for in a quantum mechanical description of the system.

To this end, we introduce coupling terms into the Schrödinger equation for the entire system to account for interactions between the leads and the central system at the junctions. The left (right) lead is coupled to the central system by assuming a coupling term  $H_{LS}$  ( $H_{SR}$ ). Direct coupling between the left and right leads is omitted and they are taken to couple only indirectly through the central system. We assume that the time-independent Schrödinger equation of the entire, coupled system is expressible in the following matrix form [45–49]

$$\begin{bmatrix} H_L & H_{LS} & 0 \\ H_{LS}^\dagger & H_S & H_{SR} \\ 0 & H_{SR}^\dagger & H_R \end{bmatrix} \begin{bmatrix} |\psi_L\rangle \\ |\psi_S\rangle \\ |\psi_R\rangle \end{bmatrix} = E \begin{bmatrix} |\psi_L\rangle \\ |\psi_S\rangle \\ |\psi_R\rangle \end{bmatrix}. \quad (4.15)$$

Here,  $H_L$  ( $H_R$ ) is the Hamiltonian of the isolated left (right) lead and  $|\psi_i\rangle$  is the projected state ket onto subsystem  $i = L, S, R$ . The exact form of the coupling terms  $H_{LS}$  and  $H_{SR}$  is not important at this stage and will be discussed later. Generally however, they are not hermitian [43] and are localized at their respective junctions. To understand the implications of this assumption, we rewrite the first and third equations in Eq. (4.15) as

$$\begin{aligned} H_L|\psi_L\rangle + H_{LS}|\psi_S\rangle &= E|\psi_L\rangle \Leftrightarrow (H_L - E)|\psi_L\rangle = H_{LS}|\psi_S\rangle, \\ H_R|\psi_R\rangle + H_{SR}^\dagger|\psi_S\rangle &= E|\psi_R\rangle \Leftrightarrow (H_R - E)|\psi_R\rangle = H_{SR}^\dagger|\psi_S\rangle. \end{aligned} \quad (4.16)$$

Using Eq. (4.13), we define the Green's operators for the isolated left (L) and right (R) leads

$$g_L(E) = \frac{1}{E - H_L + i\eta} \quad \text{and} \quad g_R(E) = \frac{1}{E - H_R + i\eta}. \quad (4.17)$$

Applying Eq. (4.17) in Eq. (4.16) yields

$$|\psi_L\rangle = g_L H_{LS} |\psi_S\rangle \quad \text{and} \quad |\psi_R\rangle = g_R H_{SR}^\dagger |\psi_S\rangle. \quad (4.18)$$

The second equation in Eq. (4.15) now yields

$$\begin{aligned} H_{LS}^\dagger |\psi_L\rangle + H_S |\psi_S\rangle + H_{SR} |\psi_R\rangle &= E |\psi_S\rangle \\ \Leftrightarrow H_{LS}^\dagger g_L H_{LS} |\psi_S\rangle + H_S |\psi_S\rangle + H_{SR} g_R H_{SR}^\dagger |\psi_S\rangle &= E |\psi_S\rangle \\ \Leftrightarrow (E - H_S - H_{LS}^\dagger g_L H_{LS} - H_{SR} g_R H_{SR}^\dagger) |\psi_S\rangle &= 0. \end{aligned} \quad (4.19)$$



Defining the self-energy operators

$$\Sigma_L(E) = H_{LS}^\dagger g_L H_{LS} \text{ and } \Sigma_R(E) = H_{SR} g_R H_{SR}^\dagger, \quad (4.20)$$

we arrive at

$$(E - H_S - \Sigma_L - \Sigma_R)|\psi_S\rangle = 0 \quad (4.21)$$

and define the Green's operator for the central system coupled to leads [48–51]

$$G_S(E) = \frac{1}{E - H_S - \Sigma_L - \Sigma_R}. \quad (4.22)$$

Equations (4.19)-(4.22) show that  $G_S$ ,  $\Sigma_L$  and  $\Sigma_R$  act on the central system subspace and not the entire, coupled system. In principle, the leads thus enter into the central system Green's operator as self-energy operators, and their appearance motivates the consideration of an effective central system Hamiltonian  $H'_S = H_S + \Sigma_L + \Sigma_R$ , with leads included. However, like the coupling terms [Eq. (4.15)], the self-energies [Eq. (4.20)] are not hermitian, which complicates a physical interpretation beyond standard quantum mechanics: the spectrum of  $H'_S$  is generally complex and the eigenstates can no longer be interpreted easily. As a result, inclusion of leads in central-system calculations is not simply a matter of using the Hamiltonian  $H'_S$  instead of  $H_S$  and the notion of an effective central system Hamiltonian  $H'_S$  is restricted to  $G_S$  [Eq. (4.22)] and observables derived from  $G_S$ , which indeed motivates a further analysis of the properties of  $H'_S$ . Provided the self-energies can be considered as “small” terms compared to  $H_S$ , the spectrum of  $H'_S$  will approximately correspond to that of  $H_S$ , but slightly shifted and with added imaginary parts due to the leads. The imaginary parts result in level-broadening in the central-system density of states, which is given by [43]

$$D(E) = \frac{i}{2\pi} \text{Tr} [G_S(E) - G_S^\dagger(E)]. \quad (4.23)$$

This means that each  $\delta$ -peak in the density of states of the uncoupled central system, described by  $H_S$  alone, becomes a slightly-shifted and broadened peak in the density of states of the coupled central system [43, 47].

Using the Hamiltonian postulated in Eq. (4.15), we now derive an expression for the total current  $I$  through the central system [43, 48, 49]. For an arbitrary electron state  $|\psi\rangle$  of the entire coupled system, the projection  $|\psi_i\rangle$  onto system component  $i$  is obtained by applying the projection operator  $P_i$  onto said component,  $i = L, S, R$ . Since  $|\psi\rangle$  is normalized over the entire system, the probability of finding the electron in the central system is given by  $\langle\psi_S|\psi_S\rangle$ , and so the total charge there is

$$Q_S = -e\langle\psi_S|\psi_S\rangle = -e\langle\psi|P_S^2|\psi\rangle = -e\langle\psi|P_S|\psi\rangle, \quad (4.24)$$

where we used the property  $P_S^2 = P_S$  of the projection operator [19]. The total current through the central system is obtained from  $Q_S$  using the continuity equation.

#### 4. Modelling transport through the finite system

For the central system charge and current densities  $\rho$  and  $\mathbf{j}$ , it reads

$$\frac{\partial \rho}{\partial t} + \nabla \cdot \mathbf{j} = 0, \quad (4.25)$$

or by integrating over the central system and applying the divergence theorem

$$I = \frac{\partial Q_S}{\partial t}. \quad (4.26)$$

Using Eq. (4.24), one finds

$$\begin{aligned} I &= -e \frac{\partial}{\partial t} \langle \psi | P_S | \psi \rangle = -e \left[ \left( \frac{\partial}{\partial t} \langle \psi | \right) P_S | \psi \rangle + \langle \psi | P_S \left( \frac{\partial}{\partial t} | \psi \rangle \right) \right] \\ &= -e \left[ \left( \frac{\partial}{\partial t} \langle \psi | \right) | \psi_S \rangle + \langle \psi_S | \left( \frac{\partial}{\partial t} | \psi \rangle \right) \right] = i \frac{e}{\hbar} [\langle \psi_S | H | \psi \rangle - \langle \psi | H | \psi_S \rangle] \\ &= i \frac{e}{\hbar} \left[ \langle \psi_S | H_{LS}^\dagger + H_S + H_{SR} | \psi \rangle - \langle \psi | H_{LS} + H_S + H_{SR}^\dagger | \psi_S \rangle \right], \end{aligned} \quad (4.27)$$

where we have picked out the terms in the Hamiltonian Eq. (4.15) which couple to  $|\psi_S\rangle$  and  $\langle\psi_S|$ . Picking out the nonzero matrix elements, for example  $\langle\psi_S|H_S|\psi\rangle = \langle\psi_S|H_S|\psi_S\rangle$ , gives

$$\begin{aligned} I &= i \frac{e}{\hbar} \left[ \langle \psi_S | H_{LS}^\dagger | \psi_L \rangle + \langle \psi_S | H_{SR} | \psi_R \rangle - \langle \psi_L | H_{LS} | \psi_S \rangle - \langle \psi_R | H_{SR}^\dagger | \psi_S \rangle \right] \\ &= i \frac{e}{\hbar} \left( \left[ \langle \psi_S | H_{LS}^\dagger | \psi_L \rangle - \langle \psi_L | H_{LS} | \psi_S \rangle \right] + \left[ \langle \psi_S | H_{SR} | \psi_R \rangle - \langle \psi_R | H_{SR}^\dagger | \psi_S \rangle \right] \right) \\ &\equiv I_L + I_R, \end{aligned} \quad (4.28)$$

where we have identified the currents  $I_L$  and  $I_R$  through the left and right junctions into the central system based on the states and coupling terms involved

$$\begin{aligned} I_L &= i \frac{e}{\hbar} \left[ \langle \psi_S | H_{LS}^\dagger | \psi_L \rangle - \langle \psi_L | H_{LS} | \psi_S \rangle \right], \\ I_R &= i \frac{e}{\hbar} \left[ \langle \psi_S | H_{SR} | \psi_R \rangle - \langle \psi_R | H_{SR}^\dagger | \psi_S \rangle \right], \end{aligned} \quad (4.29)$$

which are general expressions for the current through both junctions. In a steady state,  $I = \partial_t Q_S = 0$  and hence  $I_L = -I_R$ , i. e. the current through one junction is cancelled by an equal but opposite current through the other.

As discussed in the beginning of this section, the leads are connected to the central system to supply electrons for transport. We denote the eigenstates of the uncoupled left and right lead by  $|q_L\rangle$  and  $|q_R\rangle$ , respectively. Consider an electron occupying an eigenstate  $|q_L\rangle$  of energy  $E$ . If the left lead were uncoupled to the central system, the electron would propagate indefinitely in this left-lead eigenmode. In the coupled system however, it is affected by a local perturbation close to the junction due to interaction with the central system, resulting in reflection back into

the left lead and/or transmission into the central system. The transmitted part propagates through the central system to the junction with the right lead, where it in turn may be transmitted or reflected. As a result, a net current flows from the right lead to the left lead through the central system. The incident eigenstate thus generates excitations in the entire system and, using Eq. (4.29), we shall calculate the resulting current. Physically, these excitations are the response of the system to the incident eigenstate, and hence a subject of the Green's function discussed in Sec. 4.1. To calculate the system response to  $|q_L\rangle$ , we assume that the state vector of the entire coupled system is expressible in scattering form, namely as a sum of the incident eigenstate and the response [20]. Note that the Hamiltonian Eq. (4.15) is time-independent and hence only elastic (energy-conserving) scattering is considered. We denote the generated excitations in the various system components by  $|\psi_i\rangle$ ,  $i = L, S, R$ . Following Ref. [49], the Schrödinger equation for the coupled system becomes, in analogy with Eq. (4.15),

$$\begin{bmatrix} H_L & H_{LS} & 0 \\ H_{LS}^\dagger & H_S & H_{SR} \\ 0 & H_{SR}^\dagger & H_R \end{bmatrix} \begin{bmatrix} |q_L\rangle + |\psi_L\rangle \\ |\psi_S\rangle \\ |\psi_R\rangle \end{bmatrix} = E \begin{bmatrix} |q_L\rangle + |\psi_L\rangle \\ |\psi_S\rangle \\ |\psi_R\rangle \end{bmatrix} \quad (4.30)$$

or equivalently

$$\begin{aligned} H_L|\psi_L\rangle + H_{LS}|\psi_S\rangle &= E|\psi_L\rangle \\ H_{LS}^\dagger(|q_L\rangle + |\psi_L\rangle) + H_S|\psi_S\rangle + H_{SR}|\psi_R\rangle &= E|\psi_S\rangle \\ H_{SR}^\dagger|\psi_S\rangle + H_R|\psi_R\rangle &= E|\psi_R\rangle. \end{aligned} \quad (4.31)$$

The first and third equations yield

$$|\psi_L\rangle = g_L H_{LS}|\psi_S\rangle \quad \text{and} \quad |\psi_R\rangle = g_R H_{SR}^\dagger|\psi_S\rangle, \quad (4.32)$$

from which the second equation gives

$$\begin{aligned} H_{LS}^\dagger|q_L\rangle + H_{LS}^\dagger|\psi_L\rangle + H_S|\psi_S\rangle + H_{SR}|\psi_R\rangle &= E|\psi_S\rangle \\ \Leftrightarrow (E - H_S - H_{LS}^\dagger g_L H_{LS} - H_{SR} g_R H_{SR}^\dagger)|\psi_S\rangle &= H_{LS}^\dagger|q_L\rangle \\ \Leftrightarrow (E - H_S - \Sigma_L - \Sigma_R)|\psi_S\rangle &= H_{LS}^\dagger|q_L\rangle \\ \Leftrightarrow |\psi_S\rangle &= G_S H_{LS}^\dagger|q_L\rangle, \end{aligned} \quad (4.33)$$

where we used the Green's operators of the isolated leads [Eq. (4.17)], the self-energies [Eq. (4.20)] and the Green's operator for the coupled central system [Eq. (4.22)]. This gives  $|\psi_S\rangle$ , the response of the central system, in terms of the incident eigenmode  $|q_L\rangle$ . Using Eq. (4.33) in Eq. (4.32) gives the response of the leads in terms of  $|q_L\rangle$ , namely

$$|\psi_L\rangle = g_L H_{LS} G_S H_{LS}^\dagger|q_L\rangle \quad \text{and} \quad |\psi_R\rangle = g_R H_{SR}^\dagger G_S H_{LS}^\dagger|q_L\rangle. \quad (4.34)$$

The transmission of an electron from left to right lead corresponds to a net current flowing from right to left lead via the central system. Assuming no accumulation

#### 4. Modelling transport through the finite system

of charge in the central system, by current conservation it suffices to calculate the current through either junction. Let us calculate the current  $I_R^{qL}$ , from the right lead into the central system due to a single incident left-lead eigenmode  $|q_L\rangle$ . Using Eq. (4.29) and the excitations in Eqs. (4.33) and (4.34), one finds

$$\begin{aligned}
I_R^{qL} &= i\frac{e}{\hbar} \left[ \langle \psi_S | H_{SR} | \psi_R \rangle - \langle \psi_R | H_{SR}^\dagger | \psi_S \rangle \right] \\
&= i\frac{e}{\hbar} \left[ \langle q_L | H_{LS} G_S^\dagger H_{SR} g_R H_{SR}^\dagger G_S H_{LS}^\dagger | q_L \rangle - \langle q_L | H_{LS} G_S^\dagger H_{SR} g_R^\dagger H_{SR}^\dagger G_S H_{LS}^\dagger | q_L \rangle \right] \\
&= i\frac{e}{\hbar} \langle q_L | H_{LS} G_S^\dagger H_{SR} \left( g_R - g_R^\dagger \right) H_{SR}^\dagger G_S H_{LS}^\dagger | q_L \rangle \\
&= i\frac{e}{\hbar} \langle q_L | H_{LS} G_S^\dagger \left( H_{SR} g_R H_{SR}^\dagger - H_{SR} g_R^\dagger H_{SR}^\dagger \right) G_S H_{LS}^\dagger | q_L \rangle \\
&= i\frac{e}{\hbar} \langle q_L | H_{LS} G_S^\dagger \left( \Sigma_R - \Sigma_R^\dagger \right) G_S H_{LS}^\dagger | q_L \rangle \\
&\equiv \frac{e}{\hbar} \langle q_L | H_{LS} G_S^\dagger \Gamma_R G_S H_{LS}^\dagger | q_L \rangle,
\end{aligned} \tag{4.35}$$

where we used Eq. (4.20) and define the operator

$$\Gamma_R = i(\Sigma_R - \Sigma_R^\dagger). \tag{4.36}$$

To get the total current  $I_R$  from the right lead into the central system due to incident left-lead eigenstates, we sum over all incident left-lead eigenmodes. Let

$$H_L |q_L\rangle = \epsilon_{q_L}^L |q_L\rangle \text{ and } H_R |q_R\rangle = \epsilon_{q_R}^R |q_R\rangle. \tag{4.37}$$

The occupation of left-lead states is determined by the chemical potential  $\mu_L$ . Hence

$$\begin{aligned}
I_R &= \int dE \sum_{q_L} \delta(E - \epsilon_{q_L}^L) f(E, \mu_L, T) I_R^{qL} \\
&= \frac{e}{\hbar} \int dE \sum_{q_L} \delta(E - \epsilon_{q_L}^L) f(E, \mu_L, T) \langle q_L | H_{LS} G_S^\dagger \Gamma_R G_S H_{LS}^\dagger | q_L \rangle.
\end{aligned} \tag{4.38}$$

Inserting a closure relation for the central system subspace yields

$$\begin{aligned}
I_R &= \frac{e}{\hbar} \int dE \sum_{q_L} \delta(E - \epsilon_{q_L}^L) f(E, \mu_L, T) \langle q_L | H_{LS} \sum_{\alpha} |\alpha\rangle \langle \alpha| G_S^\dagger \Gamma_R G_S H_{LS}^\dagger | q_L \rangle \\
&= \frac{e}{\hbar} \int dE f(E, \mu_L, T) \sum_{\alpha} \langle \alpha | G_S^\dagger \Gamma_R G_S H_{LS}^\dagger \left( \sum_{q_L} \delta(E - \epsilon_{q_L}^L) |q_L\rangle \langle q_L| \right) H_{LS} |\alpha\rangle.
\end{aligned} \tag{4.39}$$

Since

$$\frac{1}{E - \epsilon_{q_L}^L \pm i\eta} = \frac{\mathcal{P}}{E - \epsilon_{q_L}^L} \mp i\pi\delta(E - \epsilon_{q_L}^L), \tag{4.40}$$

where  $\mathcal{P}$  denotes the principal value, one has

$$\delta(E - \epsilon_{q_L}^L) = \frac{i}{2\pi} \left( \frac{1}{E - \epsilon_{q_L}^L + i\eta} - \frac{1}{E - \epsilon_{q_L}^L - i\eta} \right) \quad (4.41)$$

and therefore, using Eqs. (4.17) and (4.37),

$$\begin{aligned} \sum_{q_L} \delta(E - \epsilon_{q_L}^L) |q_L\rangle \langle q_L| &= \frac{i}{2\pi} \sum_{q_L} \left( \frac{1}{E - \epsilon_{q_L}^L + i\eta} - \frac{1}{E - \epsilon_{q_L}^L - i\eta} \right) |q_L\rangle \langle q_L| \\ &= \frac{i}{2\pi} \sum_{q_L} \left( \frac{1}{E - H_L + i\eta} - \frac{1}{E - H_L - i\eta} \right) |q_L\rangle \langle q_L| \quad (4.42) \\ &= \frac{i}{2\pi} (g_L - g_L^\dagger) \sum_{q_L} |q_L\rangle \langle q_L| = \frac{i}{2\pi} (g_L - g_L^\dagger) \end{aligned}$$

by closure  $\sum_{q_L} |q_L\rangle \langle q_L| = 1$  for the isolated left lead. Using Eq. (4.42) in Eq. (4.39) yields

$$\begin{aligned} I_R &= \frac{e}{\hbar} \int dE f(E, \mu_L, T) \sum_{\alpha} \langle \alpha | G_S^\dagger \Gamma_R G_S H_{LS}^\dagger \left( \sum_{q_L} \delta(E - \epsilon_{q_L}^L) |q_L\rangle \langle q_L| \right) H_{LS} | \alpha \rangle \\ &= \frac{e}{\hbar} \int dE f(E, \mu_L, T) \sum_{\alpha} \langle \alpha | G_S^\dagger \Gamma_R G_S H_{LS}^\dagger \frac{i}{2\pi} (g_L - g_L^\dagger) H_{LS} | \alpha \rangle \\ &= \frac{e}{\hbar} \int dE f(E, \mu_L, T) \sum_{\alpha} \langle \alpha | G_S^\dagger \Gamma_R G_S i (\Sigma_L - \Sigma_L^\dagger) | \alpha \rangle \\ &= \frac{e}{\hbar} \int dE f(E, \mu_L, T) \sum_{\alpha} \langle \alpha | G_S^\dagger \Gamma_R G_S \Gamma_L | \alpha \rangle \\ &= \frac{e}{\hbar} \int dE f(E, \mu_L, T) \text{Tr} [G_S^\dagger \Gamma_R G_S \Gamma_L], \end{aligned} \quad (4.43)$$

where we define the operator  $\Gamma_L$  in analogy with Eq. (4.36), but with  $R \rightarrow L$ . Equation (4.43) gives the current through the right lead into the central system due to incident eigenmodes from the left lead. By current continuity and since we assume no charge accumulation in the central system, it gives the current through the central system due to incident eigenmodes from the left lead. To obtain the total current through the central system, we must also consider incident eigenmodes from the right lead, the occupation of which is determined by the chemical potential of the right lead,  $\mu_R$ . The transmission of an electron from right lead to left lead via the central system corresponds to a current from left to right. The resulting current through the right lead must be subtracted from Eq. (4.43), yielding the total central system current from right to left

$$I = \frac{e}{\hbar} \int dE (f(E, \mu_L, T) - f(E, \mu_R, T)) \text{Tr} [G_S^\dagger \Gamma_R G_S \Gamma_L]. \quad (4.44)$$

#### 4. Modelling transport through the finite system

In equilibrium, when  $\mu_L = \mu_R$ , the current vanishes.

Consider a small deviation from equilibrium with  $\mu_L = \mu + \delta\mu$  and  $\mu_R = \mu$ , where  $\delta\mu \rightarrow 0^+$ , resulting in a net flow of electrons from left to right. We assume that this corresponds to the application of a bias  $-V = -\delta\mu/e \rightarrow 0^-$ , lowering the left lead in electric potential relative to the right lead. As Eq. (2.30) shows, the Fermi functions depend on the difference in chemical potential and energy, i. e.  $f(E, \mu) = f(E - \mu)$  for a fixed temperature  $T$ . Taylor expanding the left lead Fermi function  $f(E - \mu_L) = f(E - \mu - \delta\mu)$  in the variable  $E - \mu - \delta\mu$  around the point  $E - \mu$  yields

$$\begin{aligned} f(E, \mu_L) &\approx f(E - \mu) + (E - \mu - \delta\mu - E + \mu) \frac{\partial f(E - \mu - \delta\mu)}{\partial(E - \mu - \delta\mu)} \Big|_{E - \mu - \delta\mu = E - \mu} \\ &= f(E - \mu) - \delta\mu \frac{\partial f(E - \mu)}{\partial(E - \mu)}, \end{aligned} \quad (4.45)$$

such that the Eq. (4.44) becomes (we use  $\delta\mu = eV$ )

$$I = -V \frac{e^2}{h} \int dE \frac{\partial f(E - \mu)}{\partial(E - \mu)} \text{Tr} \left[ G_S^\dagger \Gamma_R G_S \Gamma_L \right]. \quad (4.46)$$

Assuming furthermore vanishing temperature  $T \rightarrow 0$ , states with  $E < \mu$  are fully occupied and states with  $E > \mu$  empty. Hence, the Fermi function becomes a step function

$$f(E - \mu) = \Theta(\mu - E) \Leftrightarrow \frac{\partial f(E - \mu)}{\partial(E - \mu)} = -\delta(\mu - E), \quad (4.47)$$

yielding the current

$$I = V \frac{e^2}{h} \int dE \delta(\mu - E) \text{Tr} \left[ G_S^\dagger \Gamma_R G_S \Gamma_L \right] = V \frac{e^2}{h} \text{Tr} \left[ G_S^\dagger \Gamma_R G_S \Gamma_L \right] \Big|_{E=\mu}, \quad (4.48)$$

which is linear in the bias  $V$ . Hence, the conductance  $G = I/V$  of the coupled central system in this zero-temperature, linear-response limit is given by [17, 43]

$$G = \frac{e^2}{h} \text{Tr} \left[ G_S^\dagger \Gamma_R G_S \Gamma_L \right] \Big|_{E=\mu}, \quad (4.49)$$

which will be used to evaluate the transport properties of cylindrical core-shell systems in this work. We see that  $G$  is obtained from the Green's operator  $G_S$  of the coupled central system [Eq. (4.22)] and the operators  $\Gamma_i$ ,  $i = L, R$  [see e. g. Eq. (4.36)]. Thus, it is a property of the central system, where the self-energies  $\Sigma_i$  describe the effects of the leads, resulting in level-broadening in the central system. The form of the self-energies and the method for evaluating  $G$  will be discussed next.

### 4.3. Evaluating the conductance - Leads and coupling kernels

The operators over which the trace is taken in Eq. (4.49) all act on the central system subspace and not the entire coupled system [see discussion following Eq. (4.19)]. In order to evaluate  $G$ , we construct the necessary operators in the basis of eigenstates  $\{|\alpha\rangle\}$  of the closed central system Hamiltonian  $H_S$  [Eq. (2.22)]. Specifically, we construct the matrix of  $G_S^{-1}$  with the matrix elements [see Eq. (4.22)]

$$\langle\alpha|G_S^{-1}|\beta\rangle = (E - \epsilon_\alpha^S) \delta_{\alpha\beta} - \langle\alpha|\Sigma_L|\beta\rangle - \langle\alpha|\Sigma_R|\beta\rangle \quad (4.50)$$

and invert it numerically to find the matrix  $G_S$ . As Eq. (4.36) shows, the matrix elements  $\langle\alpha|\Sigma_i|\beta\rangle$  also give the matrix representations of the operators  $\Gamma_i$ ,  $i = L, R$ . Hence, evaluating them is sufficient to calculate  $G$  with Eq. (4.49). The self-energy matrix elements  $\langle\alpha|\Sigma_i|\beta\rangle$  are evaluated by inserting closure relations for the isolated lead  $i$  and defining a coupling kernel between the lead and the central system [52]. Before delving into this, let us consider the leads in more detail.

As discussed in the beginning of this section, the leads are taken as semi-infinite cylindrical continuations of the central system extending from the junctions over  $z < 0$  (lead L) and  $L_0 < z$  (lead R). The longitudinal part of the external magnetic field is included in the leads and we let it couple to electron spin through the Zeeman term. From Eqs. (2.12) and (2.16), it follows that the Hamiltonians  $H_i$  of the isolated leads  $i = L, R$  are given by

$$H_i = \frac{\hbar^2}{2m_e} \left[ \frac{1}{r_0^2} \left( \frac{\partial_\phi}{i} + \frac{\Phi}{\Phi_0} \right)^2 + \left( \frac{\partial_z}{i} \right)^2 \right] + \frac{\hbar\omega_c^z g_e m^*}{4} \sigma_z. \quad (4.51)$$

As with the central system, we impose hard-wall boundary conditions at the junctions. For the left lead, this yields the eigenstates [see Eq. (4.37)]

$$\begin{aligned} \langle\mathbf{r}|q_L\rangle &= \Psi_{n_L s_L k_L}^L(\mathbf{r}) = \frac{1}{\pi\sqrt{r_0}} \sin(k_L z) e^{in_L \phi} \chi_{s_L}, \\ \epsilon_{q_L}^L &= \epsilon_{n_L s_L k_L}^L = \frac{\hbar^2}{2m_e r_0^2} \left[ (r_0 k_L)^2 + \left( n_L + \frac{\Phi}{\Phi_0} \right)^2 \right] + \frac{\hbar\omega_c^z g_e m^*}{4} s_L, \end{aligned} \quad (4.52)$$

where  $n_L \in \mathbb{Z}$ ,  $k_L \in \mathbb{R}_+$ ,  $s_L \in \{\pm 1\}$  and  $\chi_{s_L}$  is an eigenspinor of  $\sigma_z$ . Right lead states  $\Psi_{n_R s_R k_R}^R(\mathbf{r})$  are obtained by switching the index  $L \rightarrow R$  and setting  $z \rightarrow z - L_0$  such that they vanish at  $z = L_0$ . Choosing  $k_i \in \mathbb{R}_+$  ensures that the eigenstates  $|q_i\rangle$  are orthonormalized over the isolated lead  $i$ , such that they satisfy a closure relation there, namely

$$\sum_{q_i} |q_i\rangle \langle q_i| = \sum_{n_i, s_i} \int_0^\infty dk_i |n_i s_i k_i\rangle \langle n_i s_i k_i| = 1. \quad (4.53)$$

#### 4. Modelling transport through the finite system

Each lead eigenstate is characterized by three quantum numbers, which we will for brevity continue to group together, such that  $|q_i\rangle$  is an orthonormal eigenket of the isolated lead  $i$ . The longitudinal part of a lead eigenstate is a standing wave, which corresponds to the superposition of plane waves with the wave numbers  $\pm k_i$ , propagating in opposite directions along the cylinder axis. Physically, they may be thought of as superpositions of scattering states incident to and reflected from the junctions due to the hard-wall boundary conditions. Aside from this backscattering, all scattering is taken to occur in the central system, by the various terms discussed in Sec. 2.2.

To illustrate the method for calculating self-energy matrix elements, let us consider the left lead in detail. The normalized eigenstates of the isolated left lead,  $|q_L\rangle$  [Eq. (4.52)], constitute an orthonormal basis for the state space of the isolated left lead and thus satisfy a closure relation there. In this basis,  $g_L$  [Eq. (4.17)] is diagonal. The matrix element  $\langle\alpha|\Sigma_L|\beta\rangle$  can be written as

$$\langle\alpha|\Sigma_L|\beta\rangle = \langle\alpha|H_{LS}^\dagger g_L H_{LS}|\beta\rangle = \sum_{q_L} \frac{\langle\alpha|H_{LS}^\dagger|q_L\rangle\langle q_L|H_{LS}|\beta\rangle}{E - \epsilon_{q_L}^L + i\eta}. \quad (4.54)$$

The coupling Hamiltonian  $H_{LS}$  thus enters as an overlap matrix element between the left lead and the central system. Using a coordinate closure relation for the entire coupled system, the overlap matrix element becomes

$$\langle\alpha|H_{LS}^\dagger|q_L\rangle = \int_{L,S,R} d\mathbf{r}d\mathbf{r}' \langle\alpha|\mathbf{r}\rangle\langle\mathbf{r}|H_{LS}^\dagger|\mathbf{r}'\rangle\langle\mathbf{r}'|q_L\rangle, \quad (4.55)$$

where the integrals extend over the central system (S) and both leads (L,R). The functions  $\langle\mathbf{r}|\alpha\rangle = \Psi_\alpha^S(\mathbf{r})$  and  $\langle\mathbf{r}'|q_L\rangle = \Psi_{q_L}^L(\mathbf{r}')$  are localized in the central system and left lead respectively and vanish everywhere else, so the two space integrals reduce to integrals over the left lead ( $\mathbf{r}'$ ) and central system ( $\mathbf{r}$ ). They couple through

$$\langle\mathbf{r}|H_{LS}^\dagger|\mathbf{r}'\rangle \equiv K_L(\mathbf{r}, \mathbf{r}'), \quad (4.56)$$

which we define as the coupling kernel  $K_L$  between the left lead and the central system. The overlap matrix element thus becomes

$$\langle\alpha|H_{LS}^\dagger|q_L\rangle = \int_S d\mathbf{r} \int_L d\mathbf{r}' (\Psi_\alpha^S(\mathbf{r}))^\dagger K_L(\mathbf{r}, \mathbf{r}') \Psi_{q_L}^L(\mathbf{r}'), \quad (4.57)$$

which can be evaluated with a suitable choice of  $K_L(\mathbf{r}, \mathbf{r}')$ . For lead  $i$ , we use

$$K_i(\mathbf{r}, \mathbf{r}') = g_0^i e^{-\delta_z^i |z' - z|} \frac{\delta(\phi - \phi')}{r_0}, \quad (4.58)$$

where  $(z, \phi)$  and  $(z', \phi')$  are central system and lead coordinates, respectively. The kernel is real and conserves the angular coordinate between lead and central system



because of the  $\delta$ -function, resulting in a circularly symmetric coupling. Here,  $g_0^i$  is a parameter with the dimension energy/length which governs the overall strength of the coupling and can be used to scale the level-broadening in the central system. The parameter  $\delta_z^i$  determines how rapidly the coupling decreases along the cylinder axis and, to be consistent with the assumption of only indirect coupling between the leads via the central system [Eq. (4.15)], it is chosen such that the exponential coupling of a given lead is vanishing at  $z$ -coordinates close to the other lead. From the overlap integral Eq. (4.55), the left lead self-energy matrix elements Eq. (4.54) readily follow. The right lead is treated analogously. Generally, the self-energy matrix elements of lead  $i = L, R$  are expressible as

$$\langle \alpha | \Sigma_i | \beta \rangle = \sum_{q_i} \frac{\int_S d\mathbf{r} \int_i d\mathbf{r}' (\Psi_\alpha^S(\mathbf{r}))^\dagger K_i(\mathbf{r}, \mathbf{r}') \Psi_{q_i}^i(\mathbf{r}') \times \int_i d\mathbf{r}'' \int_S d\mathbf{r}''' (\Psi_{q_i}^i(\mathbf{r}''))^\dagger K_i(\mathbf{r}''', \mathbf{r}'') \Psi_\beta^S(\mathbf{r}''')}{E - \epsilon_{q_i}^i + i\eta}, \quad (4.59)$$

which can be evaluated using Eqs. (4.52), (4.58) and the eigenstates of  $H_S$  [Eqs. (2.22) and (2.23)]. A detailed calculation of Eq. (4.59) is given in Appendix A. The overlap integrals between lead and central system eigenstates in Eq. (4.59) demonstrate the dependence of this coupling scheme on the central-system geometry and properties, resulting in state-dependent level-broadening.



## 5. Results of transport calculations

This section presents the results of transport calculations for cylindrical core-shell nanowires weakly coupled to leads. The length scale  $\delta_z^i$  and the coupling strength parameter  $g_0^i$  of the kernel Eq. (4.58) are assumed identical for both leads. We set  $\delta_z^i = 10/L_0$ , while  $g_0^i$  is chosen such that the self-energy matrix elements Eq. (4.59) are of the order 1 meV, and so the choice of  $g_0^i$  generally depends on system size. The resulting shift and broadening of the central system spectrum are thus both of the order 1 meV, which minimizes the effects of the leads on central system conductance, the behaviour of which should be governed by the physical properties of the central system, i. e. by  $H_S$ . We will focus on the transport properties of cylinders in longitudinal magnetic fields, as discussed for a closed system in Sec. 3.2. The Dresselhaus SOI term Eq. (2.20) is furthermore completely neglected. The central system and leads are taken as InAs shells with material parameters given in the beginning of Chapter 3, unless noted differently. The relevant central system Hamiltonian is given in Eq. (3.13).

### 5.1. Flux-periodic conductance oscillations and spin effects

Let  $r_0 = 16.8$  nm and  $L_0 = 50.4$  nm. Growth of nanowires of comparable radius has been reported in e. g. Refs. [1, 9, 53]. With  $g_0^i = 5.5$  meV/nm, one obtains self-energy matrix elements of the order 1 meV. The aspect ratio is  $\eta = 3$ , which ensures that angular and axial quantization levels result in approximately equal level spacing in the central system, as Figs. 3.4 (b) and 3.5 show. Figure 5.1 shows the conductance  $G$ , calculated using Eq. (4.49), as a function of the longitudinal magnetic flux  $\Phi$  and the chemical potential  $\mu$ . Different subfigures demonstrate the effects of the various spin-dependent terms on  $G$ . For reference, the closed-system spectrum in each case is shown in Fig. 5.2 as a function of  $\Phi$  over the corresponding energy range. Roughly, a comparison between the figures reveals that conductance peaks occur when  $\mu$  intersects with an energy level, so  $G(\Phi)$  manifests as the broadened

## 5. Results of transport calculations

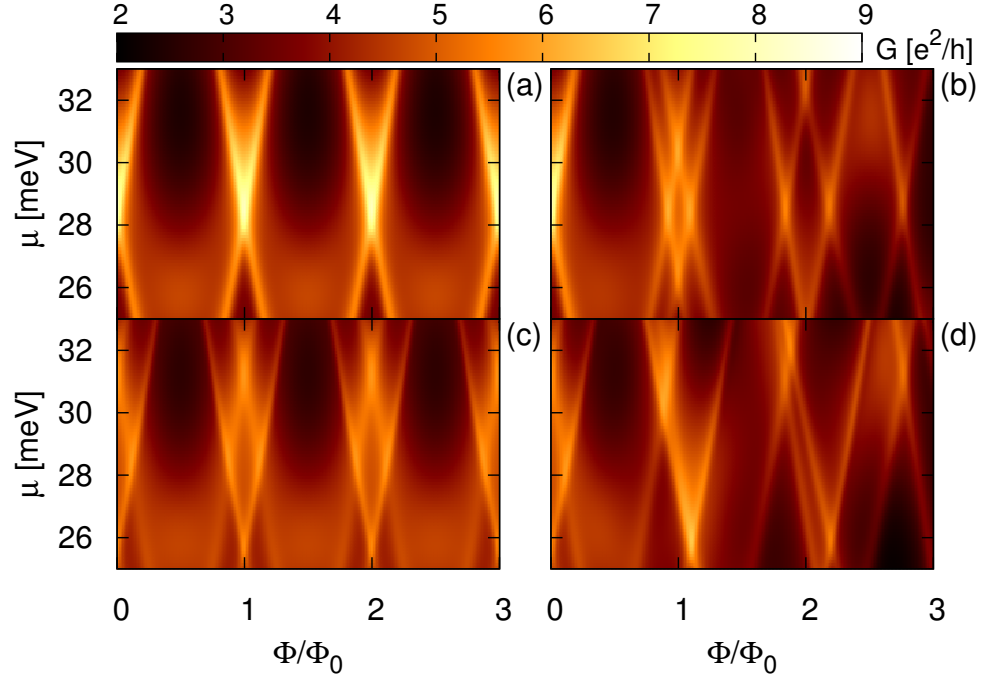


Figure 5.1: Conductance of a cylinder with aspect ratio  $\eta = 3$  for varying values of the chemical potential and magnetic flux, with: (a)  $\alpha_R = g_e = 0$ . (b)  $\alpha_R = 0$ ,  $g_e = -14.9$ . (c)  $\alpha_R = 20 \text{ meVnm}$ ,  $g_e = 0$ . (d)  $\alpha_R = 20 \text{ meVnm}$ ,  $g_e = -14.9$ . Conductance peaks correspond to broadened chemical potential intersections with the closed-system spectrum, resulting in periodic conductance oscillations provided  $g_e = 0$  (compare with Fig. 5.2). The shape and phase of the oscillations are dependent on the value of  $\mu$  considered, due to the varied structure of the spectrum.

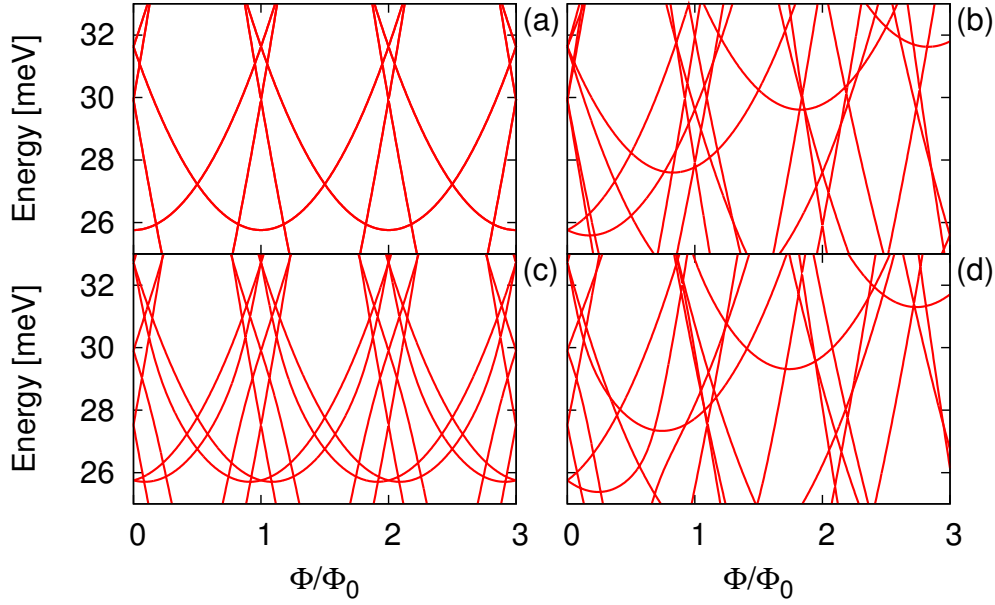


Figure 5.2: Spectrum of a cylinder with aspect ratio  $\eta = 3$  as a function of magnetic flux with: (a)  $\alpha_R = g_e = 0$ . (b)  $\alpha_R = 0$ ,  $g_e = -14.9$ . (c)  $\alpha_R = 20 \text{ meVnm}$ ,  $g_e = 0$ . (d)  $\alpha_R = 20 \text{ meVnm}$ ,  $g_e = -14.9$ . Provided  $g_e = 0$ , the spectrum is periodic in the longitudinal magnetic flux even in the presence of Rashba SOI.

and slightly shifted spectrum  $\epsilon_\alpha^S(\Phi)$  of  $H_S$ . As we have mentioned, this due to the weak coupling to leads through the self-energy operators in  $G_S$  [Eq. (4.22)]. With spin suppressed, i. e.  $g_e = \alpha_R = 0$ , the conductance [Fig. 5.1 (a)] retains the flux-periodicity of the spectrum [Fig. 5.2 (a)]. While  $G$  is flux-periodic for all values of  $\mu$ , the shape and phase of the oscillations are sensitive to the value of  $\mu$  considered. This is due to the varied structure of the spectrum. Including the Zeeman term lifts spin-degeneracy at  $\Phi \neq 0$  and spoils the periodicity of the spectrum. This is indeed reflected in  $G$ , as a comparison between Figs. 5.1 (b) and 5.2 (b) shows. On the other hand, Rashba SOI alone is insufficient to break the flux-periodicity of the spectrum, again reflected in the conductance [27], as Figs. 5.1 (c) and 5.2 (c) show. Compared with the case when  $g_e = \alpha_R = 0$  in Fig. 5.1 (a), Rashba SOI generally causes a shift and split of conductance curves, analogous to the lifting of degeneracies in the spectrum, resulting in the formation of more peaks of smaller amplitude at a fixed  $\mu$ . Lastly, when both the Zeeman and Rashba terms are included, the periodicity is again destroyed [Figs. 5.1 (d) and 5.2 (d)]. In summary, the flux-dependence of  $G$  at a fixed  $\mu$  reflects the flux-dependence of the closed system spectrum  $\epsilon_\alpha^S$  at the corresponding energy. This extends to the spin-dependent Rashba and Zeeman terms, the effects of which on the spectrum were discussed in Sec. 3.2.

## 5. Results of transport calculations

Spin-splitting of states due to the Zeeman term breaks the flux-periodicity of conductance oscillations. As may be seen from Fig. 5.1 (b), the aperiodicity can produce magnetoconductance curves which gradually increase or decrease on average at a fixed chemical potential. This is an interesting characteristic, especially in light of recent published experimental results, which show flux-periodic conductance oscillations superimposed on background fluctuations [11]. Let us consider a cylinder with  $r_0 = 55$  nm and  $L_0 = 100$  nm, realistic parameters given the systems reported in Ref. [11]. For transport calculations, we couple it weakly to leads with  $g_0^i = 0.95$  meV/nm. Figure 5.3 (a) shows the flux-dependence of the closed-system spectrum with  $g_e = -14.9$  and  $\alpha_R = 0$ , as given in Eq. (3.14). Each axial mode  $p$  is composed of states occupying different angular quantization levels  $n$ , which couple to  $\Phi$  producing sequences of parabolas in the spectrum. As a result, the minimum of each axial sublevel is characterized by the bottom part of a parabola. At  $\Phi \neq 0$ , the parabolas are furthermore split into spin up and down states due to the Zeeman term. For a given axial mode, this spin-splitting of the energy minimum produces sloped “traces” of the corresponding parabolic bottoms, marked with dots in Fig. 5.3. A linear equation for the traces follows from the parabola minima of Eq. (3.14) with  $n = -\Phi/\Phi_0$ , namely

$$\epsilon_{ps}^{\text{trace}}(\Phi) = \frac{\hbar^2}{2m_e r_0^2} \left[ \frac{r_0^2}{L_0^2} \pi^2 p^2 + g_e m^* \frac{\Phi}{\Phi_0} s \right]. \quad (5.1)$$

Due to the traces, the density of states (DOS) varies slowly with  $\Phi$ , yielding a large-scale “background” modulation. Intuitively, at a given energy, the DOS should increase gradually as two such traces approach each other, but decrease as they move apart. The dashed lines in Fig. 5.3 (a) mark the energies 15 and 21 meV, which are located between two such traces, distancing from the former and approaching the latter. This results in a gradually decreasing and increasing DOS, respectively, as Fig. 5.4 shows. The same trend is also visible in the conductance evaluated at the corresponding chemical potentials  $\mu = 15$  and 21 meV, as Figure 5.5 (a) shows. Hence, the background conductance oscillations observed in experiment may in part be due to an interplay between Zeeman splitting and the finite system length.

As Eq. (5.1) shows, the slopes of the traces can be tuned by varying the  $g$ -factor. For illustrative purposes, Fig. 5.3 (b) shows the spectrum with a doubled  $g$ -factor,  $g_e = -29.8$ , and  $\alpha_R = 0$  still. This doubles the slopes of traces and reveals crossings between them. Figure 5.5 (b) shows the conductance evaluated at the same chemical potential values as before,  $\mu = 15$  and 21 meV. The latter comes close to a crossing between traces around  $\Phi/\Phi_0 \approx 15$ , as can be seen in Fig. 5.3 (b), and reveals that the crossings indeed manifest as peaks in background conductance oscillations. We can apply the correspondence between crossings of traces and peaks in background conductance oscillations to calculate the electron  $g$ -factor. A crossing between two traces, characterized by the quantum numbers  $p_1, s_1$  and  $p_2, s_2$ , occurs

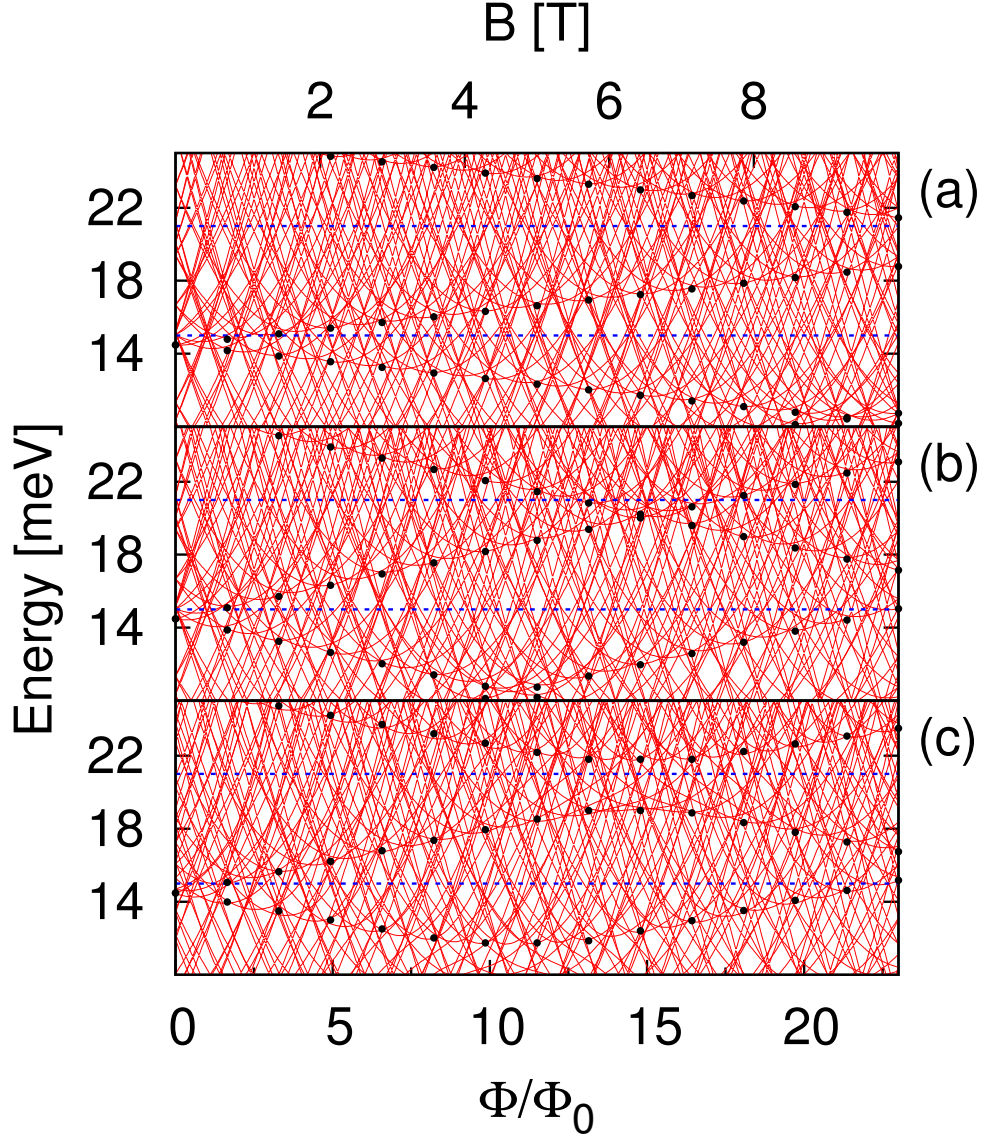


Figure 5.3: Spectrum of a cylinder with  $r_0 = 55$  nm and  $L_0 = 100$  nm with: (a)  $g_e = -14.9$ ,  $\alpha_R = 0$ . (b)  $g_e = -29.8$ ,  $\alpha_R = 0$ . (c)  $g_e = -29.8$ ,  $\alpha_R = 20$  meVnm. Due to Zeeman splitting, axial-sublevel minima produce sloped linear “traces” of parabola minima marked with dots. The traces can cross, resulting in large-scale DOS oscillations at a fixed energy. Doubling  $g_e$  moves the crossings to smaller values of  $\Phi$ . With Rashba SOI included the crossings become avoided. The values of  $\mu$  used to calculate  $G(\Phi)$  in Fig. 5.5 are marked marked with dashed lines.

## 5. Results of transport calculations

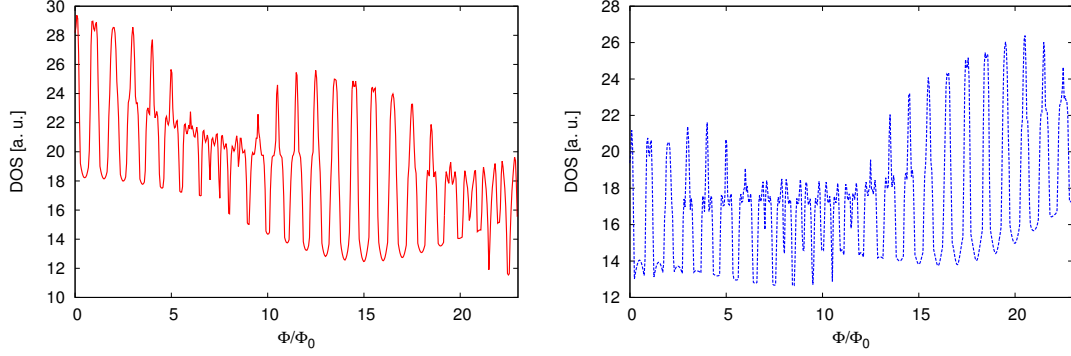


Figure 5.4: Density of states of a cylinder coupled to leads, using the parameters  $r_0 = 55$  nm,  $L_0 = 100$  nm,  $g_e = -14.9$  and  $\alpha_R = 0$  meVnm, evaluated at the energies 15 (left) and 21 (right) meV, marked with dashed lines in Fig. 5.3 (a). The sloped “traces” result in a slowly varying DOS with  $\Phi$ .

at the particular value of  $\Phi$  where the corresponding lines intersect [Eq. (5.1)]

$$\frac{r_0^2}{L_0^2}\pi^2 p_1^2 + g_e m^* \frac{\Phi}{\Phi_0} s_1 = \frac{r_0^2}{L_0^2}\pi^2 p_2^2 + g_e m^* \frac{\Phi}{\Phi_0} s_2. \quad (5.2)$$

Solving for  $g_e$  yields

$$g_e = \frac{\pi^2 r_0^2}{m^* L_0^2} \left( \frac{\Phi}{\Phi_0} \right)_c^{-1} \frac{p_2^2 - p_1^2}{s_1 - s_2}, \quad (5.3)$$

where  $(\Phi/\Phi_0)_c$  is the magnetic flux at which the lines intersect. Here,  $s_1 - s_2 = \pm 2$  because only traces of opposite spin may intersect. If  $p_2 > p_1$  and the  $g$ -factor is known to be positive (negative), then  $s_1 - s_2 = +(-)2$ . The value of  $(\Phi/\Phi_0)_c$  may be estimated from Fig. 5.5 as the flux at which the background conductance oscillations are maximum. Let us apply this to  $G(\Phi)$  evaluated at  $\mu = 21$  meV in Fig. 5.5 (b), where the background oscillations peak around  $(\Phi/\Phi_0)_c \approx 15$ . To proceed, we must know which axial levels form the relevant traces. If  $\mu$  is known, this follows from the condition

$$p_1^2 < \frac{2m_e L_0^2 \mu}{\hbar^2 \pi^2} < p_2^2, \quad (5.4)$$

which must hold at  $\Phi = 0$  [Eq. (3.14)]. On the other hand, if  $\mu$  is not known a guess of the relevant axial modes is necessary. In the present case,  $\mu = 21$  meV and one finds  $p_1 = 3$  and  $p_2 = 4$ , which yields  $g_e \approx -30$  compared to the input value  $g_e = -29.8$ . In Figs. 5.5 (a) and (b), we also note a beating pattern in the magnetoconductance. In the present model, the beating pattern arises due to Zeeman splitting, and setting  $g_e = 0$  again yields perfectly flux-periodic oscillations (see Fig. 5.1). Note that doubling  $g_e$  results in a smaller beating period, as for example a comparison between the curves at  $\mu = 15$  meV illustrates. The beating pattern arises because, at a given energy, the Zeeman term causes a flux-dependent misalignment of the parabolas in Eq. (3.14). In other words, at a fixed energy, the



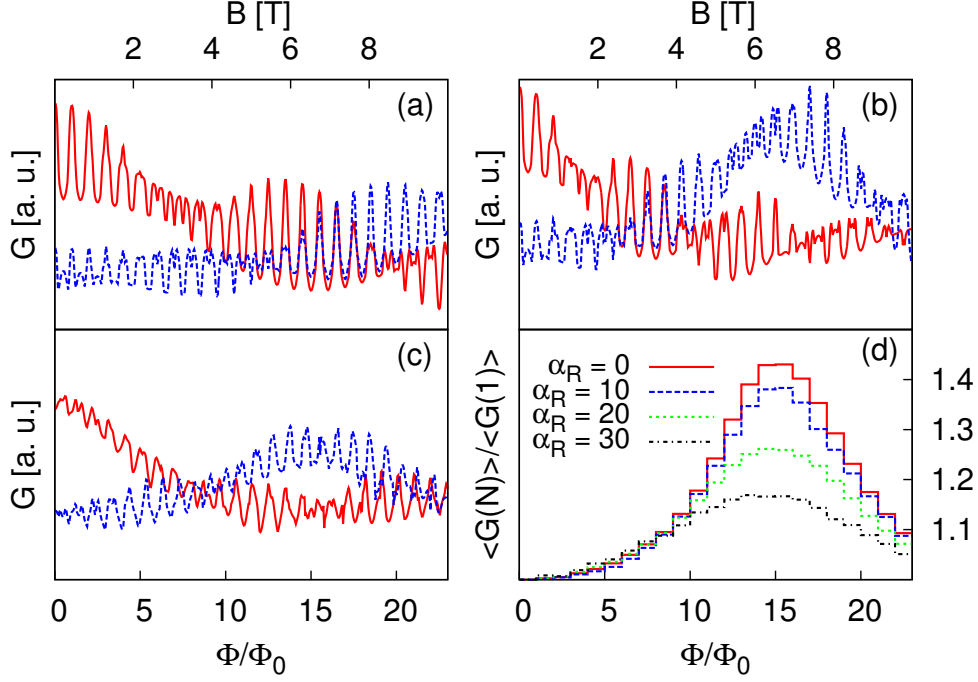


Figure 5.5: A cylinder with  $r_0 = 55$  nm and  $L_0 = 100$  nm. (a), (b) and (c):  $G(\Phi)$  evaluated at  $\mu = 15$  meV (solid) and  $\mu = 21$  meV (dashed) with (a)  $g_e = -14.9$ ,  $\alpha_R = 0$ , (b)  $g_e = -29.8$ ,  $\alpha_R = 0$  and (c)  $g_e = -29.8$ ,  $\alpha_R = 20$  meVnm. Due to Zeeman splitting, conductance oscillations are superimposed on background fluctuations, the form of which depends on  $\mu$  as is reflected in the spectrum [compare with Figs. 5.3 (a), (b) and (c)]. (d) Flux-averaged conductance  $\langle G(N) \rangle$  relative to  $\langle G(N = 1) \rangle$  at  $\mu = 21$  meV, plotted against flux number  $N$  with  $g_e = -29.8$  for different values of  $\alpha_R$ , given in units of meVnm in the key. As  $\alpha_R$  increases, the amplitude of the peak around  $\Phi/\Phi_0 = N = 15$  is reduced, reflected in the Rashba-induced avoided crossings of “traces” in Fig. 5.3 (c).

## 5. Results of transport calculations

flux-spacing between energy levels oscillates as one moves along the  $\Phi$ -axis, such that they go from being densely packed into a narrow flux-interval to being evenly spread out [see Figs. 5.3 (a) and (b)]. The DOS oscillates analogously and hence the conductance as well.

Finally, Fig. 5.3 (c) shows the spectrum with  $g_e = -29.8$  still and  $\alpha_R = 20$  meVnm. Interestingly, due to Rashba SOI, the crossings of the traces become avoided, such that their energy separation increases with  $\alpha_R$ . Figure 5.5 (c) shows the corresponding  $G(\Phi)$  evaluated at  $\mu = 15$  and 21 meV, as before. As discussed before, Rashba SOI dampens the conductance peaks observed. Furthermore, the SOI-induced “gap” between traces in the spectrum dampens the background-oscillation peak in conductance, as a comparison of the peaks around  $\Phi/\Phi_0 \approx 15$  in Figs. 5.5 (b) and (c) illustrates. For a better understanding of how the amplitude of the background conductance oscillations varies with  $\alpha_R$ , Fig. 5.5 (d) shows how the conductance  $\langle G(N) \rangle$  averaged over the  $N$ -th flux  $N - 1 \leq \Phi/\Phi_0 \leq N$ ,  $N \in \mathbb{Z}_+$ , varies with  $N$  relative to  $\langle G(N = 1) \rangle$  for different values of  $\alpha_R$ . Formally, we define the flux-averaged conductance at a fixed  $\mu$  as (let  $\Phi/\Phi_0 \equiv \tilde{\Phi}$ )

$$\langle G(N) \rangle = \int_{\tilde{\Phi}=N-1}^{\tilde{\Phi}=N} G(\tilde{\Phi}) d\tilde{\Phi}. \quad (5.5)$$

Such averaging excludes the flux-periodic part of the oscillations and allows us to focus on the background conductance oscillations. Normalizing each curve with  $\langle G(N = 1) \rangle$  makes possible a comparison between curves with different  $\alpha_R$ , as it gives the relative amplitude of the background oscillations. Analogous to Figs. 5.5 (b) and (c),  $\langle G(N) \rangle$  in Fig. 5.5 (d) peaks around  $N = 15$ , but as  $\alpha_R$  increases the peak is reduced in amplitude. This is sensible, as increasing  $\alpha_R$  increases the “gaps” between traces [Fig. 5.3 (c)], which intuitively decreases the DOS there and hence the conductance. It has been shown that  $\alpha_R$  is tunable by applying a gate voltage [33, 34, 36], and therefore measurements on peaks in background magnetoconductance oscillations in core-shell nanowires may allude to the existence of Rashba SOI in such systems. Importantly, a nonzero  $\alpha_R$  flattens, but does not shift peaks in background conductance oscillations much compared to  $\alpha_R = 0$ , and so Eq. (5.3) may still be applied to estimate the  $g$ -factor.

## 5.2. Transverse electric field

Next, we consider the effects of a static, transverse electric field  $\mathbf{E}_T = E_x \hat{a}_x$  on the flux-periodic oscillations. Again, we set  $r_0 = 16.8$  nm,  $L_0 = 50.4$  nm and  $g_0^i = 5.5$  meV/nm. For simplicity, we will ignore spin in this section, as spin effects on the

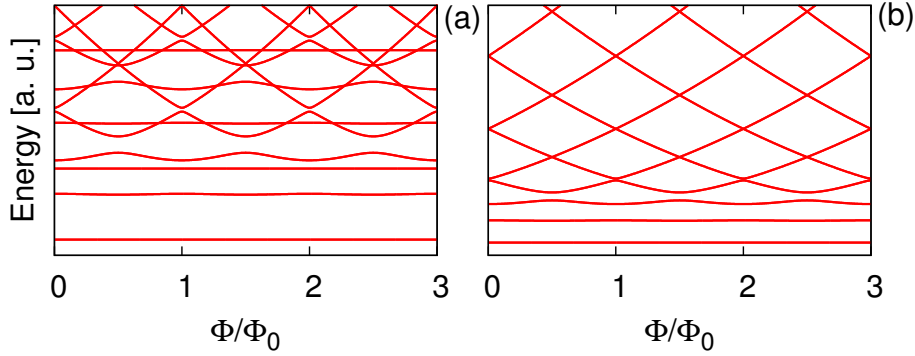


Figure 5.6: Energy spectrum as a function of magnetic flux with a transverse electric field  $E_x = 1$  meV/nm for a finite cylinder of: (a) aspect ratio  $\eta = 3$ , (b) aspect ratio  $\eta = 0.25$  (ring limit). The spectrum remains periodic in  $\Phi$ , although oscillations are reduced in amplitude for states with low angular momentum  $L_z$ . Note that the figures are not to scale.

flux-periodic oscillations were analyzed in the previous section. The central system Hamiltonian is given by [see Eqs. (2.12) and (2.21)]

$$H_S = \frac{\hbar^2}{2m_e} \left[ \frac{1}{r_0^2} \left( \frac{\partial_\phi}{i} + \frac{\Phi}{\Phi_0} \right)^2 + \left( \frac{\partial_z}{i} \right)^2 \right] + eE_x r_0 \cos(\phi). \quad (5.6)$$

The rotational symmetry of the system is broken since  $H_S$  and  $L_z$  no longer commute [see Eq. (2.34)]. Hence, the electric field mixes states with different orbital angular momenta.

Figure 5.6 (a) shows the flux-dependence of the energy spectrum of the closed cylinder with a transverse electric field applied. Some crossings have become avoided since  $L_z$  is no longer a constant of the motion and some states are flattened in energy as functions of  $\Phi$ . In the absence of a transverse electric field, each level associated with axial confinement contains states of successively higher angular momentum  $L_z = \hbar n$  [see Fig. 3.4]. In the presence of a transverse electric field, the lowest angular momentum states are flattened, as is demonstrated in Fig. 5.6 (b), which shows the spectrum of a cylinder with the same radius, but of aspect ratio  $\eta = 0.25$ , i. e. in the ring-limit, such that the energetically-lowest states at  $E_x = 0$  are states of successively higher  $L_z$  occupying the lowest axial mode [Fig. 3.4 (a)]. The flux-periodic oscillations of states with low  $L_z$  are flattened as functions of  $\Phi$  when  $E_x \neq 0$  and for sufficiently large  $E_x$ , their amplitudes become vanishing. However, states with large  $L_z$  still clearly oscillate periodically with  $\Phi$ . Thus, a transverse electric field does not strictly speaking break the flux-periodicity of the

## 5. Results of transport calculations

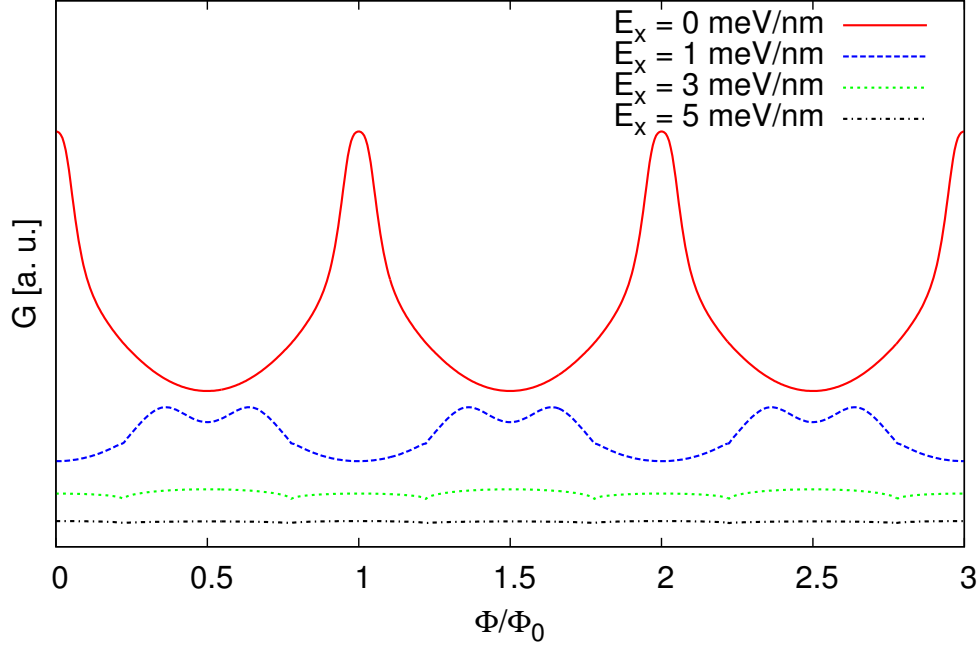


Figure 5.7: Magnetoconductance of a finite cylinder with aspect ratio  $\eta = 3$  in transverse electric fields of varying strength. The chemical potential is fixed at  $\mu = 29$  meV. Conductance oscillations remain flux-periodic, but as  $E_x$  increases their amplitude decreases and they are gradually washed out, such that  $G$  at fixed  $\mu$  is effectively constant as a function of  $\Phi$  in large transverse fields. The curves are to scale, but have been shifted along the  $y$ -axis for clarity.

spectrum. This follows from  $H_S$  in Eq. (5.6), which does not couple  $\Phi$  and  $E_x$ . As a result, the properties of the cylinder remain flux-periodic when a transverse electric field is included [23, 54]. Generally, the amplitude of flattened states decreases as  $E_x$  increases, and increasing  $E_x$  will flatten states with larger  $L_z$ .

Due to the electric potential  $V_T = -E_x r_0 \cos(\phi)$ , electrons have the electrostatic energy term  $U(\phi) = er_0 E_x \cos(\phi)$ , which is maximum and minimum  $\pm er_0 E_x$  at  $\phi = 0$  and  $\phi = \pi$ , respectively. States that have small  $L_z$  when  $E_x = 0$  have low rotational energy around the cylinder circumference, and so their circular motion is strongly disturbed by this potential. For reference, in the present example, states with  $L_z = \pm \hbar$  have rotational energy 6 meV, compared to the  $U(\phi)$  extrema  $\pm 17$  meV if  $E_x = 1$  mV/nm. Therefore,  $U(\phi)$  leads to the localization of states with low  $L_z$  around  $\phi = \pi$  and simultaneously a depletion from  $\phi = 0$ . This effect increases with  $E_x$ , in a sense depleting one half of the cylinder by “trapping” states with larger  $L_z$ . Similarly, states with small  $L_z$  become increasingly localized and thus no longer enclose a magnetic flux, a necessary prerequisite for the flux-periodic oscillations [12], which in turn explains their flattening in both spectrum and conductance.

In Fig. 5.7, we show the calculated magnetoconductance of a cylinder at  $\mu = 29$  meV in transverse electric fields of varying strength. Since  $E_x$  generally shifts the spectrum of the central system down in energy relative to the leads, we have added a model gate voltage to the Hamiltonian in Eq. (5.6)

$$H_S \rightarrow H_S + eV_G, \quad (5.7)$$

to shift the spectrum back, by aligning the ground states at  $\Phi = 0$  for the various values of  $E_x$  considered, in order to make possible a comparison between them at the same chemical potential. Conductance oscillations remain flux-periodic even when  $E_x \neq 0$ , but their shape and phase within a single period varies and with increasing  $E_x$ , their amplitude is reduced, mirroring the central system spectrum as we have seen before [Figs. 5.1 and 5.2].

### 5.3. Broken circular symmetry of the contacts

From an experimental point of view, the assumption of a circularly symmetric coupling kernel [Eq. (4.58)] may be unrealistic, as contacts typically only connect to restricted parts of the wire, but not the entire circumference [9–11]. In this section, we will check the dependence of the flux-periodic conductance oscillations on this circular contact symmetry. To do this, we break it explicitly by restricting the coupling regions to finite angles, which corresponds to the experimentally-relevant situation of the contacts no longer having uniform angular coverage of the cylindrical surface. We again consider a cylinder with  $r_0 = 16.8$  nm,  $L_0 = 50.4$  nm and  $g_0^i = 5.5$  meV/nm, and furthermore neglect spin, such that the Hamiltonian is given by Eq. (2.12). Assuming vanishing coupling at junction  $i = L, R$ , except in the angular interval  $\varphi_{min}^i \leq \varphi \leq \varphi_{max}^i$ , we introduce Heaviside step functions  $\Theta(x)$  into the coupling kernel in Eq. (4.58)

$$K^i(\mathbf{r}, \mathbf{r}') \rightarrow K^i(\mathbf{r}, \mathbf{r}') [\Theta(\phi - \phi_{min}^i) - \Theta(\phi - \phi_{max}^i)]. \quad (5.8)$$

Figure 5.8 compares the magnetoconductance of the cylinder with restricted and unrestricted coupling. In (a), the left and right junctions extend over equally long, but different angular intervals, and in (b) they extend over angular intervals of different length. Regardless, we see that the oscillations indeed remain flux-periodic. However, compared to the case with unrestricted coupling, the overall conductance is reduced and the shape of the oscillations within a given period may change depending on the intervals considered.

## 5. Results of transport calculations

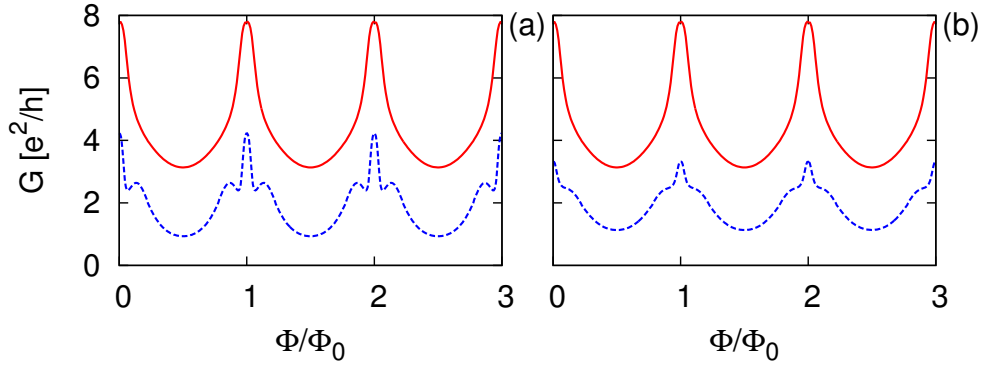


Figure 5.8: Magnetoconductance evaluated at  $\mu = 29 \text{ meV}$  of the cylinder with spin neglected and unrestricted coupling (solid lines), compared to the case with coupling restricted to (dashed lines): (a)  $(\varphi_{min}^L, \varphi_{max}^L) = (0, \pi)$  and  $(\varphi_{min}^R, \varphi_{max}^R) = (\pi, 2\pi)$ . (b)  $(\varphi_{min}^L, \varphi_{max}^L) = (\pi/2, 3\pi/2)$  and  $(\varphi_{min}^R, \varphi_{max}^R) = (\pi/2, 2\pi)$ . Restricting the coupling alters the shape of the conductance oscillations, but they remain flux-periodic.

## 6. Inclusion of core impurities

As discussed in Chapter 1, the number of shell conduction electrons may be increased in realistic core-shell nanowires by modulation doping the core with donors, which produces ionized Coulomb impurities in the core, i. e. attractive potentials to shell conduction electrons. In this section we outline how such impurities are included in our formalism and discuss their effects.

### 6.1. Formalism

Static, donor-like impurities in the core introduce a Coulomb potential  $V_I$  with which shell conduction electrons interact. The potential  $V_I$  is a sum of individual electron-impurity interaction potentials

$$V_I(\mathbf{r}) = \sum_i \nu_i(\mathbf{r}), \quad (6.1)$$

where  $\nu_i(\mathbf{r})$  is the potential due to impurity  $i$  located at  $\mathbf{r}_i = (r_i, \phi_i, z_i)$ , which is given by

$$\nu_i(\mathbf{r}) = -\frac{e^2}{4\pi\epsilon} \frac{1}{|\mathbf{r} - \mathbf{r}_i|}. \quad (6.2)$$

Here,  $\epsilon = \epsilon_r \epsilon_0$  is the material dielectric constant. The impurities can thus be included at the single-electron level by incorporating  $V_I$  into the central-system Hamiltonian Eq. (2.22), namely

$$H_S \rightarrow H_S + V_I, \quad (6.3)$$

which is then diagonalized in the same basis as before [see discussion following Eq. (2.22)]. One thereby obtains the effects of the impurities on any observable derived from  $H_S$ , including the densities Eqs. (2.28) and conductance Eq. (4.49).

An alternative method for including impurities is to solve a Dyson equation, which yields the Green's operator  $G_S^I$  of the coupled, central system with impurities included, from the Green's operator  $G_S$  given in Eq. (4.22) without impurities. To derive the Dyson equation, we use Eq. (4.22) to obtain

$$(E - H_S - \Sigma_L - \Sigma_R)G_S = 1. \quad (6.4)$$

## 6. Inclusion of core impurities

The corresponding equation for  $G_S^I$ , derived from the Hamiltonian  $H_S + V_I$ , is

$$\begin{aligned}
& (E - H_S - V_I - \Sigma_L - \Sigma_R)G_S^I = 1 \\
& \Leftrightarrow (E - H_S - \Sigma_L - \Sigma_R)G_S^I = 1 + V_I G_S^I \\
& \Leftrightarrow (E - H_S - \Sigma_L - \Sigma_R)G_S^I = (E - H_S - \Sigma_L - \Sigma_R)G_S + V_I G_S^I \\
& \Leftrightarrow G_S^I = G_S + G_S V_I G_S^I,
\end{aligned} \tag{6.5}$$

where we used Eq. (4.22). The final result in Eq. (6.5) is the Dyson equation [55]. An alternative form is

$$\begin{aligned}
G_S^I &= G_S + G_S V_I G_S^I = G_S + G_S V_I G_S + G_S V_I G_S V_I G_S + G_S V_I G_S V_I G_S V_I G_S + \dots \\
&= G_S + (G_S + G_S V_I G_S + G_S V_I G_S V_I G_S + \dots) V_I G_S = G_S + G_S^I V_I G_S.
\end{aligned} \tag{6.6}$$

Solving the Dyson equation yields the operator  $G_S^I$  from  $V_I$  and  $G_S$ , both of which are known for a given impurity configuration. Note that all three operators act on the central system subspace. As before, we thus construct them in the basis of closed central system eigenstates [see Eq. (2.22)]. Determining  $G_S^I$  thus becomes a matter of solving the matrix equation Eq. (6.5) and, once it is obtained,  $G$  can be calculated as before with Eq. (4.49) using  $G_S^I$  instead of  $G_S$ . One might be tempted to solve Eq. (6.5) by iteration. This approach however would require the iteration matrix  $G_S V_I$  to have a spectral radius  $\rho_T < 1$ , where the spectral radius of a matrix is defined as the largest of the absolute values of its eigenvalues [56]. We find that this condition is generally not met in our calculations. Instead, we rewrite Eq. (6.5) as

$$(1 - G_S V_I) G_S^I = G_S, \tag{6.7}$$

which can be solved numerically for the unknown matrix  $G_S^I$  as a system of matrix equations. Furthermore, since  $G_S G_S^{-1} = 1$  one finds

$$G_S (G_S^{-1} - V_I) G_S^I = G_S \tag{6.8}$$

or

$$(G_S^{-1} - V_I) G_S^I = 1, \tag{6.9}$$

which is a more convenient form in our calculations as it depends directly on the matrix  $G_S^{-1}$ , which we construct explicitly [see Eq. (4.50)], and hence saves a matrix inversion.

Both of the aforementioned methods are equivalent and therefore, one is free to choose whichever one pleases. Comparing both methods, we obtain the same numerical results. The Dyson approach offers another test since  $G_S^I$  must satisfy Eqs. (6.5) and (6.6), which it indeed does in our calculations. Both approaches necessitate the evaluation of matrix elements of the operator  $V_I$  [Eq. (6.1)], which are a bit tricky to compute. If the impurities are included directly into  $H_S$ , which is



diagonalized in the basis  $\{|nps\rangle\}$  [see discussion following Eq. (2.22)], the matrix elements  $\langle nps|V_I|n'p's'\rangle$  must be evaluated. Similarly, if the Dyson equation is used, the matrix elements  $\langle\alpha|V_I|\beta\rangle$  are required. In both cases, the following expansion of the three-dimensional Coulomb kernel in cylindrical geometries is useful [57]

$$\frac{1}{|\mathbf{r} - \mathbf{r}'|} = \sum_{m=-\infty}^{\infty} e^{im(\phi-\phi')} \frac{1}{\pi\sqrt{rr'}} Q_{m-1/2} \left( \frac{r^2 + r'^2 + (z - z')^2}{2rr'} \right), \quad (6.10)$$

where  $Q_{m-1/2}$  are associated Legendre functions of the second kind of zeroth order and half-integer degree. A detailed discussion on how the matrix elements are evaluated is given in Appendix B.

## 6.2. Results with core impurities included

We consider a cylinder with  $r_0 = 16.8$  nm,  $L_0 = 50.4$  nm and  $g_0^i = 5.5$  meV/nm. Our intent is to analyze impurity effects on the flux-periodic oscillations. With Rashba SOI and Zeeman splitting included, the Hamiltonian is thus given in Eq. (3.13), but with impurity potentials added [Eq. (6.1)]. Impurity potentials of the form Eq. (6.2) generally do not commute with the rotation operator  $D_z$  and hence break the circular symmetry of the system, except in the special case when the impurities lie on the cylinder axis  $r_i = 0$  [28]. This follows immediately from Eq. (6.2), which for impurities on the  $z$ -axis goes like

$$\frac{1}{|\mathbf{r} - \mathbf{r}_i|} = \frac{1}{\sqrt{(z - z_i)^2 + r_0^2(\cos^2(\phi) + \sin^2(\phi))}} = \frac{1}{\sqrt{(z - z_i)^2 + r_0^2}}, \quad (6.11)$$

and is thus independent of the angle  $\phi$ . Hence, it clearly commutes with  $L_z = -i\hbar\partial_\phi$  and so with  $D_z$  [Eq. (2.34)]. Small deviations in impurity location from the cylinder axis break the rotational symmetry and introduce into the spectrum avoided crossings for states with low  $L_z$ , similar to a transverse electric field as discussed in Sec. 5.2. The gaps are small if the impurities are few and close to the cylinder axis. Indeed, the resulting weakly broken rotational symmetry is barely visible in the otherwise rotationally-invariant densities  $\mathbf{j}$ ,  $\boldsymbol{\rho}$  and  $S_z$  [Eq. (2.31)], which still manifest as more or less concentric circles of constant density for a given  $z$ -coordinate [see e. g. Figs. 3.6 (a) and (d)]. The primary difference between explicit symmetry breaking due to a transverse electric field and impurities is that, unlike the electric field, impurities couple to both angular and longitudinal electron motion. Hence, their location on the  $z$ -axis can strongly affect the densities, as the impurity potentials generally ruin the longitudinal parity symmetry of the system. For example, if the impurities are concentrated close to the top end ( $z = L_0$ ) of the cylinder, the longitudinal parity symmetry is strongly violated, resulting in an upward shift of the densities, i. e.  $\mathbf{S}$ ,  $\mathbf{j}$  and  $\boldsymbol{\rho}$  increase in the upper half but decrease in the lower half.

## 6. Inclusion of core impurities

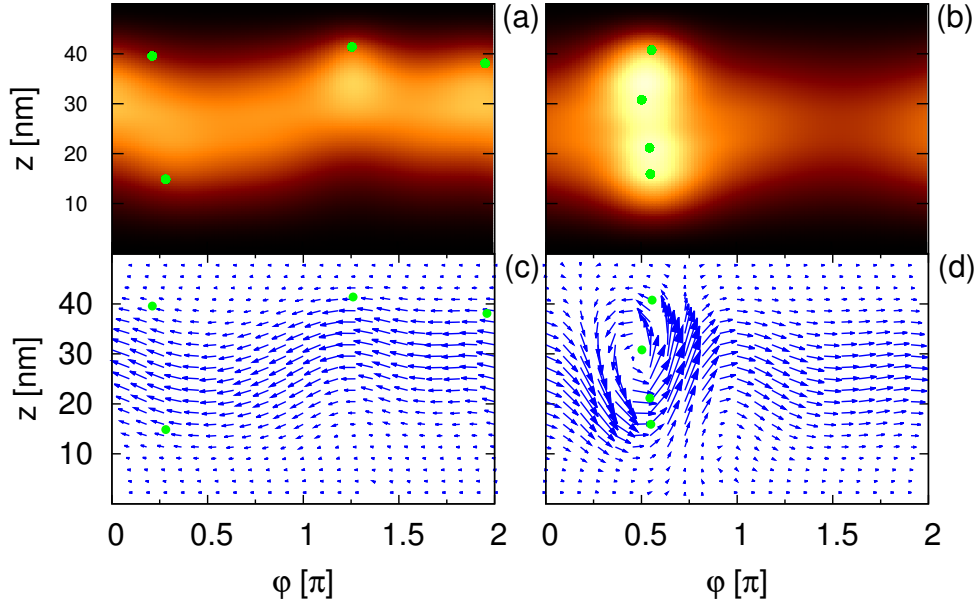


Figure 6.1: Electron (top) and current (bottom) densities of  $N_e = 8$  electrons on a cylinder with aspect ratio  $\eta = 3$  pierced by a longitudinal flux  $\Phi/\Phi_0 \approx 0.4$  with two distinct impurity configurations, 1 (left) and 2 (right), marked with filled dots. Due to the impurities, the rotational and parity symmetries are broken [compare with Figs. 3.6 (a) and (d)]. Bright and dark regions correspond to regions of high and low charge density, respectively.

However, placing impurities close to the cylinder center ( $r_i = 0$ ,  $z_i = L_0/2$ ) results in densities that are virtually indistinguishable from the case without impurities, as such a configuration “almost” conserves the parity and rotational symmetries.

Impurities are generally not located solely around the center of the cylinder axis in realistic core-shell nanowires and greatly varying densities may manifest in the closed system due to more generalized impurity distributions. In Fig. 6.1 we show the densities  $\rho$  and  $\mathbf{j}$  of  $N_e = 8$  electrons on the cylinder for two distinct distributions, where the impurity coordinates  $(\phi_i, z_i)$  are marked with filled dots. The closed-system spectra for the two distributions are shown in Fig. 6.2. In order to simplify analysis and maintain an analogy with the application of a transverse electric field [Sec. 5.2], spin is neglected in the figure. The impurities in Figs. 6.1 (a) and (c) (configuration 1) are uniformly distributed along the radial direction with coordinates in the range  $0.15 \leq r_i/r_0 \leq 0.82$ , more concentrated in the upper half of the cylinder. In Figs. 6.1 (b) and (d) (configuration 2) the impurities are condensed into a narrow angular interval around  $\phi \approx \pi/2$  close to the cylinder surface,  $0.55 \leq r_i/r_0 \leq 0.76$ . Both configurations strongly break both the rotational

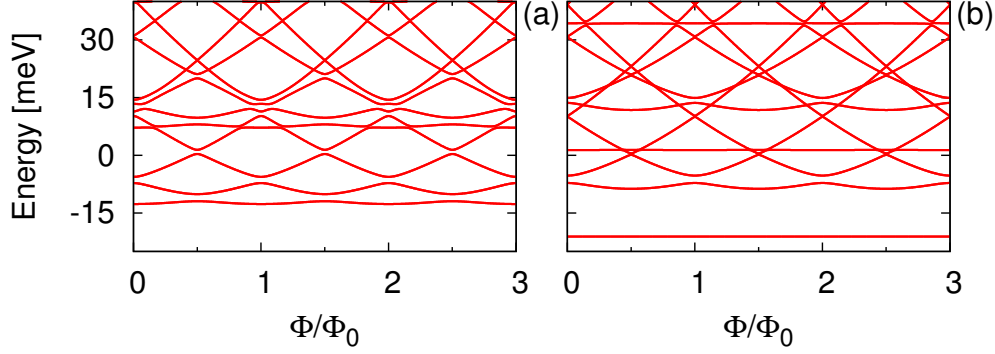


Figure 6.2: Spectra of the cylinders with the same impurity configurations as in Fig. 6.1: (a) Configuration 1. (b) Configuration 2. The impurities break the parity and rotational symmetries, resulting in avoided crossings, flattening and deformation of energy levels as functions of  $\Phi$ .

and parity symmetries of the closed system as the densities show. Configuration 2 is composed of impurities that are evenly distributed along the cylinder length at comparable distances from the surface in a narrow angular interval. As a result, they form a potential well around  $\phi \approx \pi/2$  which traps states of low orbital angular momentum  $L_z$  similar to a transverse electric field. Therefore, the electrons mostly occupy the region around  $\phi \approx \pi/2$  as  $\rho$  shows [Fig. 6.1 (c)], almost destroying their enclosure of the magnetic flux piercing the cylinder, which is a necessary prerequisite for flux-periodic oscillations [12]. Hence, the spectrum [Fig. 6.2 (b)] exhibits “flattening” of states with low  $L_z$  similar to Fig. 5.6. This is reflected in  $j$  [Fig. 6.1 (d)] which shows the formation of a vortex circulating the impurity cluster, greatly deforming the circular motion observed in Fig. 3.6 (a). On the other hand, configuration 1 affects  $\rho$  and  $j$  more modestly, by for example introducing nonvanishing  $j_z$  [Fig. 6.1 (c)]. But  $\rho$  still clearly encloses a magnetic flux [Fig. 6.1 (a)] and as a result, states with low  $L_z$  are not flattened completely [Fig. 6.2 (a)], although the amplitudes of their flux-periodic oscillations are diminished.

Donor-like impurity potentials are attractive to electrons and will thus shift the spectrum of the central system down in energy in addition to deforming the flux-dependence, as may be seen by comparing Figs. 6.2 (a), (b) and 3.4 (b). Both factors depend on the number and location of impurities. As conductance is evaluated at a fixed  $\mu$  set by the leads and primarily determined by the spectrum of  $H_S$ , adding impurities can significantly alter  $G(\Phi)$  at a fixed  $\mu$  solely due to the induced shift of the spectrum. As with the transverse electric field, we remedy this by using the model gate voltage Eq. (5.7) to shift the central system spectrum back, making possible a comparison between different impurity configurations at a fixed chemical potential. To demonstrate the effects of impurities on magnetoconductance, let us consider

## 6. Inclusion of core impurities

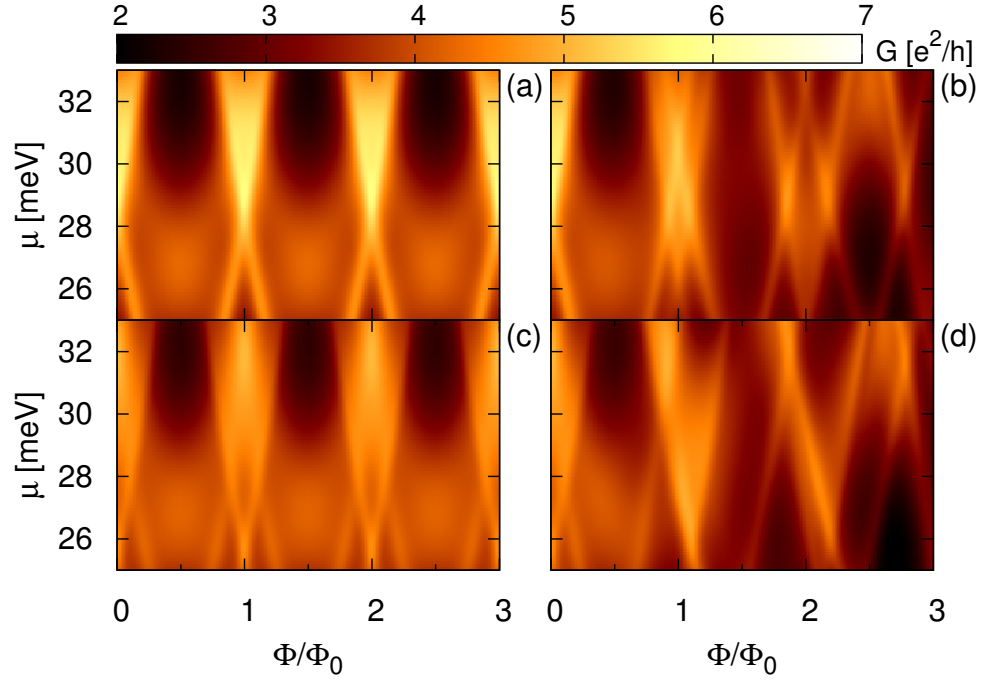


Figure 6.3: Magnetoconductance of a cylinder of aspect ratio  $\eta = 3$  with impurity configuration 1 [Figs. 6.1 (a) and (c)] and: (a)  $\alpha_R = g_e = 0$ . (b)  $\alpha_R = 0$ ,  $g_e = -14.9$ . (c)  $\alpha_R = 20 \text{ meVnm}$ ,  $g_e = 0$ . (d)  $\alpha_R = 20 \text{ meVnm}$ ,  $g_e = -14.9$ . The figures are qualitatively similar to the case without impurities given in Fig. 5.1, but with damped oscillations. Impurities alone are insufficient to break the periodicity of the oscillations.

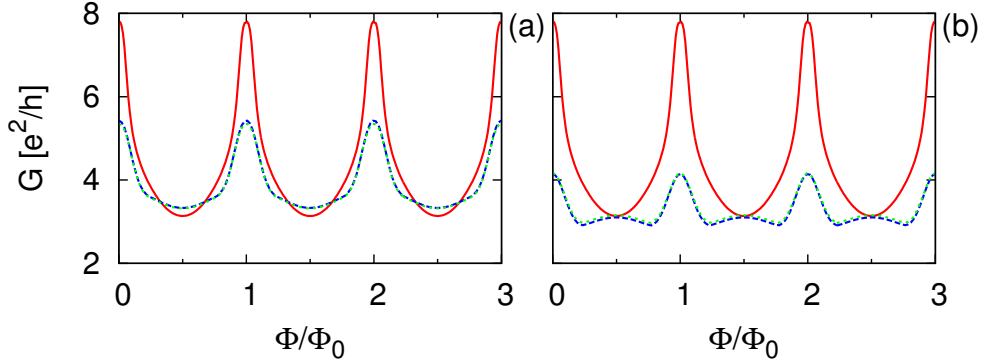


Figure 6.4: Magnetoconductance evaluated at  $\mu = 29$  meV of a cylinder coupled to leads averaged over  $N_c = 250$  (dashed) and  $N_c = 750$  (dotted) random impurity configurations containing (a)  $N = 4$  and (b)  $N = 8$  impurities each. The curves almost overlap and further averaging does not affect results significantly. The solid lines show  $G(\Phi)$  without impurities. Impurity averaging reduces conductance oscillations in amplitude, but even with a highly doped core ( $N = 8$ ) they are still clearly visible.

impurity configuration 1 used e. g. in Figs. 6.1 (a) and (c). Realigning the spectrum requires a gate voltage  $V_G = 19.1$  mV. Figure 6.3 shows the resulting conductance of the finite cylinder coupled to leads, and demonstrates the effects of the various spin-dependent terms. Provided the oscillations were periodic prior to the inclusion of impurities, i. e. if  $g_e = 0$ , they remain so when impurities are included. As with the transverse electric field, this is because the impurity potentials [Eq. (6.2)] do not couple to  $\Phi$ . The conductance curves with and without impurities [see Fig. 5.1] are qualitatively similar, but the impurities dampen oscillation amplitudes by reducing maxima and increasing minima.

The impurity-induced dampening raises the question of whether the flux-periodic conductance oscillations generally survive when donor impurities are present in the core. We have considered the conductance using a particular impurity configuration, but in reality different samples have varying, unknown configurations. To answer this question we evaluate the average magnetoconductance  $\langle G(\Phi) \rangle_c$  at a fixed  $\mu$  over multiple random impurity configurations. This gives insight into the general behaviour of an assembly of core-shell nanowires. We calculate  $\langle G(\Phi) \rangle_c$  over  $N_c$  random configurations of  $N$  impurities each, where  $N$  is constant for a given assembly. The assumption of a constant number of impurities per configuration is justified using reported average donor densities in the core. For reference, a core donor density of  $10^{17}$  cm $^{-3}$ , which is large assuming a GaAs core, corresponds to

## 6. Inclusion of core impurities

4 or 5 impurities in the central system under consideration [10, 11]. Figure 6.4 (a) compares  $G(\Phi)$  at  $\mu = 29$  meV without impurities and averaged over  $N_c = 250$  and  $N_c = 750$  configurations of  $N = 4$  impurities, a realistic value assuming a core donor density of the order of magnitude mentioned above. The two averages are practically indistinguishable and further averaging does not affect the results significantly. Here, our aim is to probe impurity effects on the amplitudes of the flux-periodic conductance oscillations and therefore spin is neglected. The applied gate voltage  $V_G$  is obtained by averaging the shift of the ground state over multiple, random  $N$ -impurity configurations. The oscillations are indeed damped, but still clearly visible after extensive averaging. Increasing the number of impurities to  $N = 8$  [Fig. 6.4 (b)] further reduces oscillation amplitudes, but they remain clearly visible. Actually, for  $N = 8$  impurities, even averaging over  $N_c = 10$  configurations already yields the same qualitative  $\langle G(\Phi) \rangle_c$  as observed in Fig. 6.4 (b) after extensive averaging, which implies that at such high core donor concentrations the exact impurity configuration is not paramount. The damping suggests that conductance oscillations may be reduced in amplitude beyond achievable experimental resolution in extremely disordered samples. However, our simulations indicate that even in the presence of a large but realistic core donor density, the oscillations are clearly resolvable. Finally, we mention that our model donor impurities do not account for screening of the impurity potentials [Eq. (6.2)]. Screening of donor impurities in the core would reduce their effects on conduction electrons and hence on both closed and open system properties [16]. Similarly, electron-electron interaction would oppose impurity-induced localizations in the system, as in e. g. Fig. 6.1 (b) and (d), and hence weaken impurity effects [28]. By ignoring screening effects in the core and electron-electron interaction, our simulations thus describe “a worst-case scenario” of the electron-impurity interactions.

## 7. Conclusions and summary

We have analyzed electron states on a cylindrical surface of finite length, to model a semiconductor core-shell nanowire. In the presence of a transverse magnetic field, we observe snaking and cyclotron states where the radial field projection is vanishing and maximum, respectively. Since the energies of cyclotron states, which are actually Landau levels, increase with magnetic field strength, depletion of electrons from the cyclotron regions sets in at sufficiently large magnetic field strengths. The system is parity invariant, excluding the Dresselhaus SOI term, which breaks a few symmetries that otherwise manifest in the charge, current and spin densities. This occurs in cylinders of finite length due to edge currents, which connect the snaking states propagating along the cylinder, and contribute strongly to Dresselhaus SOI.

In a longitudinal magnetic field, the cylinder spectrum is flux-periodic and we find that interplay between Rashba and Dresselhaus SOI is insufficient to break the rotational symmetry of the system, in contrast with known results for quantum rings. From our transport calculations, we also see flux-periodic magnetoconductance oscillations except if Zeeman splitting is included. In this case, oscillations with magnetic flux are still apparent, but they are no longer flux-periodic. On the other hand, a rich structure of background oscillations and beating patterns becomes discernible. By analyzing these oscillations, it is possible to estimate the  $g$ -factor of the electrons in the shell and detect the presence of Rashba SOI, provided the SOI strength can be varied. Our results are in qualitative agreement with recent measurements performed on GaAs/InAs core-shell nanowires. Furthermore, the flux-periodic oscillations may be flattened by applying a transverse electric field or considering particular impurity configurations, both of which strongly break the rotational symmetry of the system. This is because a necessary prerequisite to observe flux-periodic oscillations is that wave functions enclose a magnetic flux. Conductance oscillations are robust to the experimentally-relevant effects of nonuniform coupling to leads, which corresponds to the nonuniform application of contacts to the sample in experiment. Generally, impurities dampen the conductance oscillations, but they nevertheless remain clearly resolvable after extensive averaging over multiple, random impurity configurations, provided a realistic core donor density is assumed.

Several possible extensions of these calculations are possible. For example, the transport formalism could be applied to study the snaking states in more detail, but their contribution to conductance has been left untouched. It might be possible to

## 7. *Conclusions and summary*

combine transverse electric and magnetic fields to deplete one half of the cylinder, but retain snaking propagation of electrons between the cylinder edges on the other. Secondly, some form of Coulomb interaction between the electrons might be included in the central system and the resulting charging effects on transport studied, e. g. the Coulomb blockade. Coulomb repulsion would also tend to oppose localizations of electrons, for example due to impurities, a transverse electric field or in snaking regions, and might thus have nontrivial effects. Other extensions are also possible, such as considering the more realistic hexagonal core-shell geometry or a nonzero shell thickness, but would require considerable modification of the single-electron Hamiltonian.



# A. Evaluation of self-energy matrix elements

To demonstrate the evaluation of self-energy matrix elements Eq. (4.59), let us consider the left lead, namely

$$\begin{aligned}
\langle \alpha | \Sigma_L | \beta \rangle &= \sum_{q_L} \frac{\int_S d\mathbf{r} \int_L d\mathbf{r}' (\Psi_\alpha^S(\mathbf{r}))^\dagger K_L(\mathbf{r}, \mathbf{r}') \Psi_{q_L}^L(\mathbf{r}') \times \int_S d\mathbf{r}''' \int_L d\mathbf{r}'' (\Psi_{q_L}^L(\mathbf{r}''))^\dagger K_L(\mathbf{r}''', \mathbf{r}'') \Psi_\beta^S(\mathbf{r}''')}{E - \epsilon_{q_L}^L + i\eta} \\
&= \int_S d\mathbf{r} d\mathbf{r}''' \int_L d\mathbf{r}' d\mathbf{r}'' (\Psi_\alpha^S(\mathbf{r}))^\dagger K_L(\mathbf{r}, \mathbf{r}') \overbrace{\left[ \sum_{q_L} \frac{\Psi_{q_L}^L(\mathbf{r}') (\Psi_{q_L}^L(\mathbf{r}''))^\dagger}{E - \epsilon_{q_L}^L + i\eta} \right]}^{\equiv A} K_L(\mathbf{r}''', \mathbf{r}'') \Psi_\beta^S(\mathbf{r}''').
\end{aligned} \tag{A.1}$$

Using Eq. (4.52) and defining

$$\kappa_{n_L s_L}^2(E) = \frac{2m_e}{\hbar^2} \left( E - \epsilon_{n_L s_L}^L + \frac{\hbar^2 k_L^2}{2m_e} \right) = \frac{2m_e E}{\hbar^2} - \frac{1}{r_0^2} (n_L + \Phi/\Phi_0)^2 - \frac{g_e m^*}{2(l_B^z)^2} s_L, \tag{A.2}$$

one obtains (redefine  $\eta$  also)

$$\begin{aligned}
A &= \frac{2m_e}{\pi^2 r_0 \hbar^2} \sum_{n_L, s_L} e^{in_L(\phi' - \phi'')} \chi_{s_L} \chi_{s_L}^\dagger \int_0^\infty dk_L \frac{\sin(k_L z') \sin(k_L z'')}{\kappa_{n_L s_L}^2 - k_L^2 + i\eta} \\
&= \frac{-m_e}{4\pi^2 r_0 \hbar^2} \sum_{n_L, s_L} e^{in_L(\phi' - \phi'')} \chi_{s_L} \chi_{s_L}^\dagger \int_{-\infty}^\infty dk_L \frac{e^{ik_L(z'' + z')} - e^{ik_L(z'' - z')} - e^{ik_L(z' - z'')} + e^{-ik_L(z'' + z')}}{\kappa_{n_L s_L}^2 - k_L^2 + i\eta},
\end{aligned} \tag{A.3}$$

where we used the fact that the integrand is even in  $k_L$ . The four  $k_L$ -integrals are evaluated by extension into the complex plane. Poles are located at

$$k_L = \pm \kappa_{n_L s_L} \sqrt{1 + i \frac{\eta}{\kappa_{n_L s_L}^2}} \approx \pm \kappa_{n_L s_L} \left( 1 + i \frac{\eta}{2\kappa_{n_L s_L}^2} \right) \equiv \pm (\kappa_{n_L s_L} + i\eta), \tag{A.4}$$

### A. Evaluation of self-energy matrix elements

where we redefine  $\eta$  keeping the sign intact. Hence there is one pole in the upper complex half plane and one in the lower. As an example, let us do the second integral. Note that  $z', z'' \in \mathbb{R}_-$  (left lead). If  $z'' - z' < 0$  the contour must be closed in the lower half plane to ensure convergence, i. e. that  $\text{Re}\{ik_L(z'' - z')\} < 0$ , but if  $z'' - z' > 0$  the contour must be closed in the upper half plane. Applying the residue theorem and letting  $\eta \rightarrow 0^+$ , one finds

$$\frac{m_e}{4\pi^2 r_0 \hbar^2} \int_{-\infty}^{\infty} dk_L \frac{e^{ik_L(z'' - z')}}{\kappa_{n_L s_L}^2 - k_L^2 + i\eta} = \frac{im_e}{4\pi r_0 \hbar^2 \kappa_{n_L s_L}} e^{i\kappa_{n_L s_L}|z'' - z'|}. \quad (\text{A.5})$$

Since the  $k_L$ -integral extends from  $-\infty$  to  $\infty$ , closing the contour in the lower half plane necessitates a clockwise-parametrized line curve. The residue theorem applies to counterclockwise parametrized curves and hence closing in the lower half plane incurs an extra factor of  $-1$ . Treating the other integrals analogously, Eq. (A.3) yields

$$A = \frac{im_e}{2\pi r_0 \hbar^2} \sum_{n_L, s_L} \frac{e^{in_L(\phi' - \phi'')} \chi_{s_L} \chi_{s_L}^\dagger}{\kappa_{n_L s_L}} \left[ e^{-i\kappa_{n_L s_L}(z' + z'')} - e^{i\kappa_{n_L s_L}|z' - z''|} \right], \quad (\text{A.6})$$

so Eq. (A.1) becomes

$$\begin{aligned} \langle \alpha | \Sigma_L | \beta \rangle &= \frac{im_e}{2\pi r_0 \hbar^2} \sum_{n_L, s_L} \int_S d\mathbf{r} d\mathbf{r}''' \int_L d\mathbf{r}' d\mathbf{r}'' \left[ e^{-i\kappa_{n_L s_L}(z' + z'')} - e^{i\kappa_{n_L s_L}|z' - z''|} \right] \times \\ &\quad (\Psi_\alpha^S(\mathbf{r}))^\dagger K_L(\mathbf{r}, \mathbf{r}') \frac{e^{in_L(\phi' - \phi'')} \chi_{s_L} \chi_{s_L}^\dagger}{\kappa_{n_L s_L}} K_L(\mathbf{r}''', \mathbf{r}'') \Psi_\beta^S(\mathbf{r}'''). \end{aligned} \quad (\text{A.7})$$

Using Eq. (4.58), writing

$$K_L(\mathbf{r}, \mathbf{r}') \equiv K_L(z, z') \frac{1}{r_0} \delta(\phi - \phi'), \quad (\text{A.8})$$

and integrating out the  $\delta$ -functions, one finds

$$\begin{aligned} \langle \alpha | \Sigma_L | \beta \rangle &= \frac{ir_0 m_e}{2\pi \hbar^2} \sum_{n_L, s_L} \int_0^{2\pi} d\phi d\phi''' \int_0^{L_0} dz dz''' \int_{-\infty}^0 dz' dz'' \left[ e^{-i\kappa_{n_L s_L}(z' + z'')} - e^{i\kappa_{n_L s_L}|z' - z''|} \right] \times \\ &\quad (\Psi_\alpha^S(z, \phi))^\dagger K_L(z, z') \frac{e^{in_L(\phi - \phi''')} \chi_{s_L} \chi_{s_L}^\dagger}{\kappa_{n_L s_L}} K_L(z''', z'') \Psi_\beta^S(z''', \phi'''). \end{aligned} \quad (\text{A.9})$$

Since

$$\begin{aligned} e^{-i\kappa_{n_L s_L}(z' + z'')} - e^{i\kappa_{n_L s_L}|z' - z''|} &= \\ \frac{2}{i} \left[ \Theta(z' - z'') e^{-i\kappa_{n_L s_L} z''} \sin(\kappa_{n_L s_L} z') + \Theta(z'' - z') e^{-i\kappa_{n_L s_L} z'} \sin(\kappa_{n_L s_L} z'') \right], \end{aligned} \quad (\text{A.10})$$

Eq. (A.9) yields

$$\begin{aligned} \langle \alpha | \Sigma_L | \beta \rangle = & \frac{r_0 m_e}{\pi \hbar^2} \sum_{n_L, s_L} \int_0^{2\pi} d\phi d\phi''' \int_0^{L_0} dz dz''' \int_{-\infty}^0 dz' (\Psi_\alpha^S(z, \phi))^\dagger K_L(z, z') \frac{e^{in_L(\phi - \phi''')} \chi_{s_L} \chi_{s_L}^\dagger}{\kappa_{n_L s_L}} \Psi_\beta^S(z''', \phi''') \times \\ & \left[ \sin(\kappa_{n_L s_L} z') \int_{-\infty}^{z'} dz'' K_L(z''', z'') e^{-i\kappa_{n_L s_L} z''} + e^{-i\kappa_{n_L s_L} z'} \int_{z'}^0 dz'' K_L(z''', z'') \sin(\kappa_{n_L s_L} z'') \right]. \end{aligned} \quad (\text{A.11})$$

We now expand the eigenstates of  $H_S$  in terms of the orbital basis in Eq. (2.8) and eigenspinors of  $\sigma_z$

$$\Psi_\alpha^S(z, \phi) = \sum_{nps} C_{nps}^\alpha \langle \mathbf{r} | nps \rangle = \sum_{nps} \frac{C_{nps}^\alpha}{\sqrt{\pi r_0 L_0}} e^{in\phi} \sin\left(\frac{p\pi z}{L_0}\right) \chi_s \quad (\text{A.12})$$

and use the same expansion for  $\Psi_\beta^S(z''', \phi''')$  but with primed indices. Inserting into Eq. (A.11) and doing the angular part

$$\int_0^{2\pi} d\phi d\phi''' e^{i\phi(n_L - n)} e^{i\phi'''(n' - n_L)} = 4\pi^2 \delta_{n_L, n} \delta_{n_L, n'}, \quad (\text{A.13})$$

and the spin part

$$\sum_{s_L s s'} \chi_s^\dagger \chi_{s_L} \chi_{s_L}^\dagger \chi_{s'} = \sum_{s_L s s'} \delta_{s_L, s} \delta_{s_L, s'}, \quad (\text{A.14})$$

yields

$$\begin{aligned} \langle \alpha | \Sigma_L | \beta \rangle = & \frac{4m_e}{\hbar^2 L_0} \sum_{nsp p'} (C_{nps}^\alpha)^* C_{np' s}^\beta \int_0^{L_0} dz dz''' \int_{-\infty}^0 dz' \sin\left(\frac{p\pi z}{L_0}\right) K_L(z, z') \sin\left(\frac{p'\pi z'''}{L_0}\right) \times \\ & \left[ \frac{\sin(\kappa_{ns} z')}{\kappa_{ns}} \int_{-\infty}^{z'} dz'' K_L(z''', z'') e^{-i\kappa_{ns} z''} + e^{-i\kappa_{ns} z'} \int_{z'}^0 dz'' K_L(z''', z'') \frac{\sin(\kappa_{ns} z'')}{\kappa_{ns}} \right], \end{aligned} \quad (\text{A.15})$$

or equivalently, using  $K_L(z, z') = g_0^L e^{\delta_z^L(z' - z)}$

$$\begin{aligned} \langle \alpha | \Sigma_L | \beta \rangle = & \frac{4m_e (g_0^L)^2}{\hbar^2 L_0} \sum_{nsp p'} (C_{nps}^\alpha)^* C_{np' s}^\beta \int_0^{L_0} dz dz''' \int_{-\infty}^0 dz' \sin\left(\frac{p\pi z}{L_0}\right) e^{\delta_z^L(z' - z)} \sin\left(\frac{p'\pi z'''}{L_0}\right) \times \\ & \left[ \frac{\sin(\kappa_{ns} z')}{\kappa_{ns}} \int_{-\infty}^{z'} dz'' e^{\delta_z^L(z'' - z''')} e^{-i\kappa_{ns} z''} + e^{-i\kappa_{ns} z'} \int_{z'}^0 dz'' e^{\delta_z^L(z'' - z''')} \frac{\sin(\kappa_{ns} z'')}{\kappa_{ns}} \right]. \end{aligned} \quad (\text{A.16})$$

### A. Evaluation of self-energy matrix elements

Since  $\sin(x) = (e^{ix} - e^{-ix})/2i$ , all that remains are straightforward exponential integrals, all of which converge. After a tedious derivation, Eq. (A.16) yields

$$\begin{aligned} \langle \alpha | \Sigma_L | \beta \rangle &= \frac{-2m_e (g_0^L)^2 \pi^2 L_0^3}{\delta_z^L \hbar^2} \times \\ &\sum_{nspp'} (C_{nps}^\alpha)^* C_{np's}^\beta pp' \frac{1 - e^{-\delta_z^L L_0} [(-1)^{p'} + (-1)^p] + (-1)^{p+p'} e^{-2\delta_z^L L_0}}{[p^2 \pi^2 + (\delta_z^L L_0)^2] [p'^2 \pi^2 + (\delta_z^L L_0)^2] [\delta_z^L L_0 - i\kappa_{ns} L_0]^2}, \end{aligned} \quad (\text{A.17})$$

where the energy-dependent  $\kappa_{ns}(E)$  is given in Eq. (A.2). An analogous derivation for the right lead results in

$$\begin{aligned} \langle \alpha | \Sigma_R | \beta \rangle &= \frac{-2m_e (g_0^R)^2 \pi^2 L_0^3}{\delta_z^R \hbar^2} \times \\ &\sum_{nspp'} (C_{nps}^\alpha)^* C_{np's}^\beta pp' \frac{e^{-2\delta_z^R L_0} - e^{-\delta_z^R L_0} [(-1)^{p'} + (-1)^p] + (-1)^{p+p'}}{[p^2 \pi^2 + (\delta_z^R L_0)^2] [p'^2 \pi^2 + (\delta_z^R L_0)^2] [\delta_z^R L_0 - i\kappa_{ns} L_0]^2}. \end{aligned} \quad (\text{A.18})$$

The matrix elements indeed have the dimension energy, as the prefactor to the sums shows.

If coupling parameters are identical for both leads, i. e.  $g_0^L = g_0^R = g_0$  and  $\delta_z^L = \delta_z^R = \delta_z$ , an interesting symmetry exists between the self-energy matrix elements of the two leads. Let us rewrite Eqs. (A.17) and (A.18) as

$$\langle \alpha | \Sigma_L | \beta \rangle = \sum_{nspp'} \sigma_L(n, s, p, p') \quad \text{and} \quad \langle \alpha | \Sigma_R | \beta \rangle = \sum_{nspp'} \sigma_R(n, s, p, p'). \quad (\text{A.19})$$

Inspection of the numerators in Eqs. (A.17) and (A.18) shows that

$$\sigma_R(n, s, p, p') = (-1)^{p+p'} \sigma_L(n, s, p, p'). \quad (\text{A.20})$$

The difference stems from the parity of the longitudinal basis elements  $\langle z | p \rangle \sim \sin(p\pi z/L_0)$ , which are even (odd) when  $p$  is even (odd) relative to the cylinder center, as discussed in Sec. 2.4. An overlap integral between a given lead and the central system will thus differ by a factor of  $(-1)^p$  from the corresponding overlap integral with the other lead, and since the self-energy matrix elements include two such overlap integrals [see Eq. (4.54)], this factor enters twice, resulting in the factor  $(-1)^{p+p'}$  in Eq. (A.20).

## B. Evaluation of impurity-potential matrix elements

In order to obtain the matrix  $G_S^I$  from the Dyson equation (6.5), one needs the matrix  $V_I$  with matrix elements [see Eqs. (6.1) and (6.2)]

$$\langle \alpha | V_I | \beta \rangle = \sum_i \langle \alpha | \nu_i | \beta \rangle, \quad (\text{B.1})$$

where the states  $\{|\alpha\rangle\}$  are eigenkets of  $H_S$  [see Eq. (2.23)]. For illustrative purposes, let us evaluate the matrix element of a single impurity potential  $\langle \alpha | \nu_i | \beta \rangle$  due to an impurity located at  $\mathbf{r}_i = (r_i, \phi_i, z_i)$ . Using the Coulomb kernel expansion given in Eq. (6.10), the impurity potential Eq. (6.2) becomes

$$\nu_i(\mathbf{r}) = \frac{-e^2}{4\pi^2\epsilon} \frac{1}{\sqrt{r_0 r_i}} \sum_{m=-\infty}^{\infty} e^{im(\phi-\phi_i)} Q_{m-1/2}(\xi), \quad (\text{B.2})$$

where

$$\xi = \frac{r_0^2 + r_i^2 + (z - z_i)^2}{2r_0 r_i}. \quad (\text{B.3})$$

Expanding the states  $|\alpha\rangle$  in terms of the usual basis  $\{|nps\rangle\}$  [see discussion following Eq. (2.23)] yields in coordinate representation

$$\Psi_\alpha^S(z, \phi) = \sum_{nps} C_{nps}^\alpha \langle \mathbf{r} | nps \rangle = \sum_{nps} \frac{C_{nps}^\alpha}{\sqrt{\pi r_0 L_0}} e^{in\phi} \sin\left(\frac{p\pi z}{L_0}\right) \chi_s, \quad (\text{B.4})$$

and one obtains the matrix element

$$\begin{aligned} \langle \alpha | \nu_i | \beta \rangle &= \int_0^{2\pi} r_0 d\phi \int_0^{L_0} dz \left( \Psi_\alpha^S(z, \phi) \right)^\dagger \nu_i(z, \phi) \Psi_\beta^S(z, \phi) \\ &= \sum_{\substack{nps \\ n'p'}} \frac{-e^2 (C_{nps}^\alpha)^* C_{n'p's}^\beta}{2\pi^2\epsilon L_0 \sqrt{r_0 r_i}} e^{-i\phi_i(n-n')} \int_0^{L_0} dz \sin\left(\frac{p\pi z}{L_0}\right) \sin\left(\frac{p'\pi z}{L_0}\right) Q_{n-n'-1/2}(\xi) \end{aligned} \quad (\text{B.5})$$

### B. Evaluation of impurity-potential matrix elements

by evaluating the angular and spin parts. By comparing Eqs. (B.4) and (B.5), the matrix elements  $\langle nps|\nu_i|n'p's'\rangle$  necessary to include  $V_I$  directly in  $H_S$  are given by

$$\langle nps|\nu_i|n'p's'\rangle = \frac{-e^2 e^{-i\phi_i(n-n')}}{2\pi^2 \epsilon L_0 \sqrt{r_0 r_i}} \delta_{ss'} \int_0^{L_0} dz \sin\left(\frac{p\pi z}{L_0}\right) \sin\left(\frac{p'\pi z}{L_0}\right) Q_{n-n'-1/2}(\xi). \quad (\text{B.6})$$

Both matrix elements Eqs. (B.5) and (B.6) require evaluation of the integral

$$\int_0^{L_0} dz \sin\left(\frac{p\pi z}{L_0}\right) \sin\left(\frac{p'\pi z}{L_0}\right) Q_{n-n'-1/2}\left(\frac{r_0^2 + r_i^2 + (z - z_i)^2}{2r_0 r_i}\right), \quad (\text{B.7})$$

which to our knowledge can not be done analytically. To evaluate it, we employ an  $n$ -point Gaussian quadrature, which generally reads [58]

$$\int_a^b f(y)dy \approx \frac{b-a}{2} \sum_{i=1}^n w_i f\left(\left[\frac{b-a}{2}\right]x_i + \left[\frac{b+a}{2}\right]\right) \quad (\text{B.8})$$

where the abscissas  $x_i$  and weights  $w_i$  are known, tabulated constants independent of  $a$ ,  $b$  and  $f(y)$ . Accuracy can be further increased by partitioning  $[a, b]$  into  $N-1$  subintervals  $[\alpha_j, \alpha_{j+1}]$  of length  $h_\alpha = \frac{b-a}{N-1}$  each, such that  $a = \alpha_1 < \alpha_2 < \dots < \alpha_N = b$  where  $\alpha_j = a + (j-1)h_\alpha$ , and applying the Gaussian quadrature to each subinterval. One then finds

$$\begin{aligned} \int_{\alpha_j}^{\alpha_{j+1}} f(y)dy &\approx \frac{\alpha_{j+1} - \alpha_j}{2} \sum_{i=1}^n w_i f\left(\left[\frac{\alpha_{j+1} - \alpha_j}{2}\right]x_i + \left[\frac{\alpha_{j+1} + \alpha_j}{2}\right]\right) \\ &= \frac{h_\alpha}{2} \sum_{i=1}^n w_i f\left(\frac{h_\alpha}{2}x_i + \left[\frac{\alpha_{j+1} + \alpha_j}{2}\right]\right) \end{aligned} \quad (\text{B.9})$$

and therefore

$$\int_a^b f(y)dy = \sum_{j=1}^{N-1} \int_{\alpha_j}^{\alpha_{j+1}} f(y)dy \approx \frac{h_\alpha}{2} \sum_{j=1}^{N-1} \sum_{i=1}^n w_i f\left(\frac{h_\alpha}{2}x_i + \left[\frac{\alpha_{j+1} + \alpha_j}{2}\right]\right), \quad (\text{B.10})$$

which we use to evaluate the integral Eq. (B.7). We find that  $N = 5$  and  $n = 4$  approximate the integral accurately enough. The functions  $Q_{n-1/2}$  are evaluated numerically using the code provided in Ref. [59].

# Bibliography

- [1] Erik P. A. M. Bakkers and Marcel A. Verheijen. Synthesis of inp nanotubes. *Journal of the American Chemical Society*, 125(12):3440–3441, 2003.
- [2] Yat Li, Fang Qian, Jie Xiang, and Charles M. Lieber. Nanowire electronics and optoelectronic devices. *Materials Today*, 9:18, 2006.
- [3] C. Thelander, P. Agarwal, S. Brongersma, J. Eymery, L.F. Feiner, A. Forchel, M. Scheffler, W. Riess, B.J. Ohlsson, U. Gösele, and L. Samuelson. Nanowire-based one-dimensional electronics. *Materials Today*, 9:28–35, 2006.
- [4] Peidong Yang, Ruoxue Yan, and Melissa Fardy. Semiconductor nanowire: What’s next? *Nano Letters*, 10(5):1529–1536, 2010.
- [5] Fang Qian, Yat Li, Silvija Gradecak, Hong-Gyu Park, Yajie Dong, Yong Ding, Zhong Lin Wing, and Charles M. Lieber. Rashba spin–orbit coupling effect on a diluted magnetic semiconductor cylinder surface and ballistic transport . *Nature Materials*, 7(9):701–706, 2008.
- [6] Torsten Rieger, Martina Luysberg, Thomas Schäpers, Detlev Grützmacher, and Mihail Ion Lepsa. Molecular beam epitaxy growth of gaas/inas core–shell nanowires and fabrication of inas nanotubes. *Nano Letters*, 12(11):5559–5564, 2012.
- [7] J. W. W. van Tilburg, R. E. Algra, W. G. G. Immink, M. Verheijen, E. P. A. M. Bakkers, and L. P. Kouwenhoven. *Semiconductor Science and Technology*, 25(2):024011, 2010.
- [8] Ronit Popovitz-Biro, Andrey Kretinin, Palle Von Huth, and Hadas Shtrikman. Inas/gaas core–shell nanowires. *Crystal Growth & Design*, 11(9):3858–3865, 2011.
- [9] Minkyung Jung, Joon Sung Lee, Woon Song, Young Heon Kim, Sang Don Lee, Nam Kim, Jeunghee Park, Mahn-Soo Choi, Shingo Katsumoto, Hyoyoung Lee, and Jinhee Kim. Quantum interference in radial heterostructure nanowires. *Nano Letters*, 8(10):3189–3193, 2008.
- [10] C Blömers, T Rieger, P Zellekens, F Haas, M I Lepsa, H Hardtdegen, Ö Gül, N Demarina, D Grützmacher, H Lüth, and Th Schäpers. Realization

- of nanoscaled tubular conductors by means of gaas/inas core/shell nanowires. *Nanotechnology*, 24(3):035203, 2013.
- [11] Ö. Gül, N. Demarina, C. Blömers, T. Rieger, H. Lüth, M. I. Lepsa, D. Grütz-macher, and Th. Schäpers. Flux periodic magnetoconductance oscillations in gaas/inas core/shell nanowires. *Phys. Rev. B*, 89:045417, Jan 2014.
  - [12] N. Byers and C. N. Yang. Theoretical considerations concerning quantized magnetic flux in superconducting cylinders. *Phys. Rev. Lett.*, 7:46–49, Jul 1961.
  - [13] R. Winkler. *Spin orbit coupling effects in two-dimensional electron and hole systems*. Springer-Verlag, 2003.
  - [14] Giulio Ferrari, Andrea Bertoni, Guido Goldoni, and Elisa Molinari. *Phys. Rev. B*, 78:115326, Sep 2008.
  - [15] Andrei Manolescu, Tomas Orn Rosdahl, Sigurdur I. Erlingsson, Llorens Serra, and Vidar Gudmundsson. Snaking states on a cylindrical surface in a perpen-dicular magnetic field. *The European Physical Journal B*, 86(10):1–12, 2013.
  - [16] Harald Ibach and Hans Lüth. *Solid State Physics. An Introduction to Principles of Materials Science*. Springer-Verlag, 2009.
  - [17] John H. Davies. *The Physics of Low-Dimensional Semiconductors. An Intro-duction*. Cambridge University Press, 2006.
  - [18] Douglas R. Hofstadter. Energy levels and wave functions of bloch electrons in rational and irrational magnetic fields. *Phys. Rev. B*, 14:2239–2249, Sep 1976.
  - [19] Claude Cohen-Tannoudji, Bernard Diu, and Franck Laloë. *Quantum Mechan-ics*. John Wiley & Sons, 2005.
  - [20] J. J. Sakurai and Jim Napolitano. *Modern Quantum Mechanics*. Pearson, 2011.
  - [21] S. Bellucci and P. Onorato. Landau levels and edge states in a cylindrical two-dimensional electron gas: A semiclassical approach. *Phys. Rev. B*, 82:205305, Nov 2010.
  - [22] Axel Lorke, R. Johannes Luyken, Alexander O. Govorov, Jörg P. Kotthaus, J. M. Garcia, and P. M. Petroff. Spectroscopy of Nanoscopic Semiconductor Rings. *Phys. Rev. Lett.*, 84:2223–2226, Mar 2000.
  - [23] A. M. Alexeev and M. E. Portnoi. Electric dipole moment oscillations in aharonov-bohm quantum rings. *Phys. Rev. B*, 85:245419, Jun 2012.
  - [24] Y. Aharonov and D. Bohm. Significance of electromagnetic potentials in the quantum theory. *Phys. Rev.*, 115:485–491, Aug 1959.



- [25] R. A. Webb, S. Washburn, C. P. Umbach, and R. B. Laibowitz. Observation of  $h/e$  Aharonov-Bohm Oscillations in Normal-Metal Rings.
- [26] L. P. Lévy, G. Dolan, J. Dunsmuir, and H. Bouchiat. *Phys. Rev. Lett.*, 64:2074–2077, Apr 1990.
- [27] Yaroslav Tserkovnyak and Bertrand I. Halperin. Magnetoconductance oscillations in quasiballistic multimode nanowires. *Phys. Rev. B*, 74:245327, Dec 2006.
- [28] V. N. Gladilin, J. Tempere, J. T. Devreese, and P. M. Koenraad. Aharonov-bohm oscillations in the magnetic moment of multielectron randomly doped semiconductor cylindrical core-shell nanowires. *Phys. Rev. B*, 87:165424, Apr 2013.
- [29] John David Jackson. *Classical Electrodynamics*. John Wiley & Sons, 3rd edition, 1999.
- [30] B.H. Mehdiyev, A.M. Babayev, S. Cakmak, and E. Artunc. Rashba spin-orbit coupling effect on a diluted magnetic semiconductor cylinder surface and ballistic transport. *Superlattices and Microstructures*, 46(4):593–602, 2009.
- [31] A. Bringer and Th. Schäpers. Spin precession and modulation in ballistic cylindrical nanowires due to the rashba effect. *Phys. Rev. B*, 83:115305, Mar 2011.
- [32] C. Fasth, A. Fuhrer, L. Samuelson, Vitaly N. Golovach, and Daniel Loss. Direct Measurement of the Spin-Orbit Interaction in a Two-Electron InAs Nanowire Quantum Dot. *Phys. Rev. Lett.*, 98:266801, Jun 2007.
- [33] G. Engels, J. Lange, Th. Schäpers, and H. Lüth. Experimental and theoretical approach to spin splitting in modulation-doped  $\text{In}_x\text{Ga}_{1-x}\text{As}/\text{InP}$  quantum wells for  $b \rightarrow 0$ . *Phys. Rev. B*, 55:R1958–R1961, Jan 1997.
- [34] Junsaku Nitta, Tatsushi Akazaki, Hideaki Takayanagi, and Takatomo Enoki. Gate Control of Spin-Orbit Interaction in an Inverted  $\text{In}_{0.53}\text{Ga}_{0.47}\text{As}/\text{In}_{0.52}\text{Al}_{0.48}\text{As}$  Heterostructure. *Phys. Rev. Lett.*, 78:1335–1338, Feb 1997.
- [35] Saadi Lamari. Effect of the doping concentration on the zero-field spin splitting and rashba parameter in a p-inas mosfet. *Phys. Rev. B*, 67:165329, Apr 2003.
- [36] Dong Liang and Xuan P.A. Gao. Strong tuning of rashba spin-orbit interaction in single inas nanowires. *Nano Letters*, 12(6):3263–3267, 2012.
- [37] J. S. Sheng and Kai Chang. Spin states and persistent currents in mesoscopic rings: Spin-orbit interactions. *Phys. Rev. B*, 74:235315, Dec 2006.
- [38] Charles Kittel and Herbert Kroemer. *Thermal Physics*. W. H. Freeman, 1980.

## BIBLIOGRAPHY

- [39] Diego Frustaglia and Klaus Richter. *Phys. Rev. B*, 69(23):235310, Jun 2004.
- [40] M. P. Nowak and B. Szafran. Spin-orbit coupling effects in two-dimensional circular quantum rings: Elliptical deformation of confined electron density. *Phys. Rev. B*, 80:195319, Nov 2009.
- [41] Csaba Daday, Andrei Manolescu, D. C. Marinescu, and Vidar Gudmundsson. Electronic charge and spin density distribution in a quantum ring with spin-orbit and coulomb interactions. *Phys. Rev. B*, 84:115311, Sep 2011.
- [42] Fumiya Nagasawa, Jun Takagi, Yoji Kunihashi, Makoto Kohda, and Jun-saku Nitta. Experimental demonstration of spin geometric phase: Radius dependence of time-reversal aharonov-casher oscillations. *Phys. Rev. Lett.*, 108:086801, Feb 2012.
- [43] S. Datta. *Electronic Transport in Mesoscopic Systems*. Cambridge University Press, 1995.
- [44] Thordur Jonsson and Jakob Yngvason. *Waves and Distributions*. World Scientific, 1995.
- [45] Mads Brandbyge, José-Luis Mozos, Pablo Ordejón, Jeremy Taylor, and Kurt Stokbro. Density-functional method for nonequilibrium electron transport. *Phys. Rev. B*, 65:165401, Mar 2002.
- [46] K. S. Thygesen, M. V. Bollinger, and K. W. Jacobsen. Conductance calculations with a wavelet basis set. *Phys. Rev. B*, 67:115404, Mar 2003.
- [47] S. Kurth, G. Stefanucci, C.-O. Almbladh, A. Rubio, and E. K. U. Gross. Time-dependent quantum transport: A practical scheme using density functional theory. *Phys. Rev. B*, 72:035308, Jul 2005.
- [48] Magnus Paulsson and Mads Brandbyge. Transmission eigenchannels from nonequilibrium green’s functions. *Phys. Rev. B*, 76:115117, Sep 2007.
- [49] M. Paulsson. arXiv:cond-mat/0210519v2 [cond-mat.mes-hall], 2008.
- [50] Ferdows Zahid, Magnus Paulsson, and Supriyo Datta. Electrical conduction through molecules. In *Advanced Semiconductors and Organic Nano-Techniques*. Academic Press, 2003.
- [51] Tomofumi Tada, Masakazu Kondo, and Kazunari Yoshizawa. Green’s function formalism coupled with gaussian broadening of discrete states for quantum transport: Application to atomic and molecular wires. *The Journal of Chemical Physics*, 121(16):8050–8057, 2004.

- [52] Vidar Gudmundsson, Cosmin Gainar, Chi-Shung Tang, Valeriu Moldoveanu, and Andrei Manolescu. Time-dependent transport via the generalized master equation through a finite quantum wire with an embedded subsystem. *New Journal of Physics*, 11(11):113007, 2009.
- [53] Thomas Richter, Christian Blömers, Hans Lüth, Raffaella Calarco, Michael Indlekofer, Michel Marso, and Thomas Schäpers. Flux quantization effects in inn nanowires. *Nano Letters*, 8(9):2834–2838, 2008.
- [54] Z. Barticevic, G. Fuster, and M. Pacheco. Effect of an electric field on the bohm-aharonov oscillations in the electronic spectrum of a quantum ring. *Phys. Rev. B*, 65:193307, May 2002.
- [55] H. Bruus and K. Flensberg. *Many-Body Quantum Theory in Condensed Matter Physics: An Introduction*. Oxford University Press, 2004.
- [56] Brian Bradie. *A Friendly Introduction to Numerical Analysis*. Pearson Prentice Hall, 2006.
- [57] Howard S. Cohl and Joel E. Tohline. A compact cylindrical green’s function expansion for the solution of potential problems. *The Astrophysical Journal*, 527:86–101, December 1999.
- [58] Milton Abramowitz and Irene A. Stegun. *Handbook of Mathematical Functions*. Dover Publications Inc., 1970.
- [59] J. Segura and A. Gil. Evaluation of toroidal harmonics. *Computer Physics Communications*, 124(1):104–122, 2000.